



# Localizing a giant flare on a young scallop-shell star

**Cinta Vidante**

Master Thesis
For the acquirement of the scientific degree

Master of Science
*(M.Sc.)*

in the discipline of
Astrophysics

eingereicht am 28. April 2025 am
Institut für Physik und Astronomie
der Universität Potsdam

| | |
|---|---|
| **Erstgutachter** | Prof. Dr. Katja Poppenhäger |
| **Zweigutachter** | Prof. Dr. Dr. Stephan Geier |
| **Betreuer** | Dr. Ekaterina Ilin |

# Abstract

M dwarfs are prime targets for transiting exoplanet surveys. Young M dwarfs, in particular, carry cues about the conditions under which they formed. Scallop-shell stars are rapidly rotating M dwarfs in young open clusters and star-forming regions with unexplained complex and strictly periodic photometric modulation. The cause for the modulation is poorly understood. Some of these stars are reported to have changes in their modulation patterns after a strong flare, which indicates an interaction with the structures that cause the modulation. Measuring the location of strong, modulation-altering flares in scallop-shell stars present a unique way of constraining the location of the structure in question. The latitude of the flares indicate where energetic particles are ejected from these stars. When these particle hit the material and change the modulation, the latitude of the material should be similar to that of the flare.

In this thesis I study TIC 206544316, a scallop-shell star observed with the Transiting Exoplanet Survey Satellite that displayed a long-duration giant flare which was modulated in brightness by the star's fast rotation. The stellar modulation pattern was permanently altered after the flare. I used middle- and high-resolution spectra from Gaia RVS, CARMENES, and MIKE to constrain the inclination of the stellar rotation axis with the cross-correlation method and the Bayesian framework from Masuda and Winn. Combining inclination and the structure of the rotational modulation of the flare using Markov Chain Monte Carlo (MCMC), I find that the flare is a low-latitude flare, supposedly low enough to interact with any structure of material near the equator. In addition, I find that the flare itself does not follow the classical flare model commonly used in literature, with an impulsive phase followed by an exponential gradual decay. Instead, it shows a small additional bump after the impulsive phase, a part of a recently found group of complex flares called peak-bump flares.

Interaction between the flare and the material could be the cause of the observed modulation change, consistent with the favored explanations for the nature of scallop-shell stars that require material near the equator. However, a further analysis of the modulation change, showed a dimming in the lightcurve instead of a brightening, which is counter-intuitive to the simple image that a flare would disperse the occulting material after a direct hit. If the material is dust, the following CME after the flare may cause the modulation change by dislocating material from the cloud of dust around the location of ejection. If the material is plasma, the dimming can be caused by a trapped coronal mass ejection following the flare in the magnetic field line of the star due to its strong magnetic field. The peak-bump profile can be caused by material falling down to the star as a coronal rain. My work therefore demonstrate that flares can be used as powerful and highly localized probes into the surroundings of potentially planet-hosting young M dwarfs.

# Zusammenfassung

M-Zwerge sind bevorzugte Ziele für die Untersuchung von Transit-Exoplaneten. Insbesondere junge M-Zwerge liefern Hinweise auf die Bedingungen, unter denen sie entstanden sind. *Scallop-shell stars* sind schnell rotierende M-Zwerge in jungen offenen Sternhaufen und Sternentstehungsgebieten mit ungeklärter komplexer und streng periodischer photometrischer Modulation. Die Ursache der Modulation ist noch nicht vollständig verstanden. Bei einigen dieser Sterne wird nach einem starken Flare ein verändertes Modulationsmuster beobachtet, was auf eine Wechselwirkung mit den Strukturen hindeutet, die die Modulation verursachen. Die Messung der Position starker, die Modulation verändernder Flares in Jakobsmuschel-Schalen-Sternen bietet eine einzigartige Möglichkeit, die Position der betreffenden Struktur einzugrenzen. Der Breitengrad der Flares zeigt an, wo diese Sterne energiereiche Teilchen ausstoßen. Wenn diese Teilchen auf das Material treffen und die Modulation verändern, sollte der Breitengrad des Materials dem des Flares ähneln.

In dieser Arbeit untersuche ich TIC 206544316, einen *scallop-shell star*, der mit dem Transiting Exoplanet Survey Satellite beobachtet wurde und einen lang anhaltenden, riesigen Flare aufwies, dessen Helligkeit durch die schnelle Rotation des Sterns moduliert wurde. Das Erscheinungsbild der Modulation veränderte sich nach dem Flare dauerhaft. Ich verwendete mittel- und hochauflösende Spektren der Gaia-RVS-, CARMENES- und MIKE-Spektrographen, um die Neigung der Sternrotationsachse mit der Kreuzkorrelationsmethode und dem bayesschen Ansatz von Masuda und Winn zu bestimmen. Durch die Kombination von Neigung und Struktur der Rotationsmodulation des Flares mithilfe des Markov-Chain-Monte-Carlo-Verfahrens (MCMC) stelle ich fest, dass es sich bei dem Flare um einen Flare in niedrigen Breiten handelt, der vermutlich niedrig genug ist, um mit jeder Materialstruktur in Äquatornähe zu interagieren. Darüber hinaus stelle ich fest, dass der Flare selbst nicht dem in der Literatur üblichen Standard-Flare-Modell folgt. Stattdessen zeigt er nach der Impulsphase einen kleinen zusätzlichen Buckel, der zu einer kürzlich entdeckten Gruppe komplexer Flares, den sogenannten Peak-Bump-Flares, gehört.

Die Wechselwirkung zwischen Flare und Material könnte die Ursache für die beobachtete Modulationsänderung sein, was mit den bevorzugten Erklärungen für die Natur von *scallop-shell stars* übereinstimmt, die Material in Äquatornähe benötigen. Eine weitere Analyse der Modulationsänderung zeigte jedoch eine Abschwächung der Lichtkurve anstelle einer Aufhellung, was der einfachen Vorstellung widerspricht, dass ein Flare das ihn verdeckende Material nach einem direkten Treffer zerstreuen würde. Wenn das Material Staub ist, könnte der CME, der dem Flare folgt, die Modulationsänderung verursachen, indem er Material aus der Staubwolke um dem Auswurfort verlagert. Handelt es sich bei dem Material um Plasma, kann die Abschwächung durch einen eingeschlossenen koronalen Massenauswurf nach dem Flare in der Magnetfeldlinie des Sterns aufgrund seines starken Magnetfelds verursacht werden. Das Peak-Bump-Profil kann durch Material verursacht werden, das als koronaler Regen auf den Stern fällt. Meine Arbeit zeigt daher, dass Flares als leistungsstarke und hochlokalisierte Sonden in die Umgebung potenziell planetenbeherbergender junger M-Zwerge eingesetzt werden können.

# Acknowledgments

Woaaaaaaaaaaaaaaaaah. Where to begin, really. The list of people to thank for is going to be long, but I will start with thanking three amazing women. First, I want to thank and dedicate this thesis to Vivien, my mom. Every second I spent in Germany was thanks no one other than you, who, even as the sole breadwinner of the house, managed to send me to study in Germany supporting this dream of mine. Without your hard work, I would not have the privilege of writing and completing this thesis. You are the testament of perseverance. Second, Ekaterina. This thesis, and the fact that I am still mentally sound, is the result of your wonderful feedback, mentoring, support, and empowerment. You pulled me into this crazy world of flares and planet-interaction and I am now fully hooked, lined, and sinkered. You have inspired me to be bold and creative in my research. You have become my role model for a mentor. Third, and surely not the least, Katja. From the day I attended your lecture, I had hoped I would be lucky enough to become one of your students. Thank you so much for allowing me to take on this project and for inviting me to your research group. Our discussions always leave me buzzing with excitement to learn more, to discover more, and to study more. You are an absolute inspiration to an aspiring young female researcher like me, and I count my blessings for this wonderful opportunity.

I want to thank my friends in the group: Julián, who always makes time for my never-ending questions and inspires me to investigate more; Judy, who filled life at the institute with sunshine, always so encouraging and supportive; Nikoleta and Desmond, my time in the office would never have been as fun without you–thank you so much for listening to my rants and for all our impromptu conversations during work; Martiño, Linda, and Zheng, who made these last few months of intense thesis writing full of laughter. To Peter and Andreas: who gave me the means of supporting myself financially throughout this endeavor and teaching me additional instrumental skills while being awesome bosses. To Ruth: thank you for giving me the opportunity to work and study in New York. Without your support and guidance, I would not have been able to have so many exciting discussions with amazing people. To the Branch I people: Rainer, Alex, Jibin, and Mark, who were kind enough to make time to discuss science with me from so many different angles. To my dear Flora: my fellow crazies Laura and Florian. Our monthly meetups were often the highlight of my month. You made my Master's experience so much fun and helped me stay sane amidst all the homework and projects. To Caro: who became the big sister I never had and who taught me to be passionate about the things I love. To my support system back home: Vannysha, Elika, Ming, Ive, and Lenny. I am so grateful to always have people to count on, just one call away, even across the oceans. To dad and Beauty: I know you're supporting me up there from Heaven. I hope I made you both proud.

And finally to Arne, Mr. LOML. Thank you for your patience, love, and encouragement, and for giving me those much-needed moments of solace from all the stress and work. You gave me a home when my real home was so far away. This thesis lived through so many life-changing moments. There were so many times when I could have given up during my mental breakdowns, but you were always there, picking up the shattered pieces (me) and helping me rise from the ashes.

# Contents

# 1 Motivation

Arguably one of the most sought-after questions in science, that is driven by the innate curiosity of humankind, is whether life can exist beyond Earth. There is a universal consensus that the likelihood of life persisting on a distant planet is heavily dependent on its host star. These host stars play an important role in shaping the planetary environment, much like our own Sun does for Earth. The current prime targets for exoplanet detections and characterizations are M dwarfs (Section 2.1). Young M dwarfs carry cues about the conditions under which they formed. They are also considerably more magnetically active compared to their older and more massive counterparts (Section 2.2). Studying young M dwarfs and their surrounding environment is crucial for a comprehensive understanding of exoplanet habitability and the potential impact of stellar activity on young exoplanets.

Scallop-shell stars are rapidly rotating M dwarfs in young open clusters and star-forming regions with unexplained complex and strictly periodic photometric modulation (Section 3.1). The cause for the modulation of scallop-shell stars is still poorly understood with equatorial material as the most favored hypothesis (Section 3.2). Some of these stars are even reported to have changes in their modulation patterns after a strong flare, which indicates an interaction with the structures that cause the modulation. Studying scallop-shell stars could reveal the surrounding environments of young M dwarfs that were previously inaccessible.

Flares are rapid releases of coronal magnetic energy and are one of the directly observable manifestations of stellar magnetic fields (Section 2.3). Flare are also localized explosions. Material and radiation from flares are ejected out vertically from the flare location. Thus, the flare latitude gives information where energetic particles originate and active regions (Section 2.3.2). Based on current knowledge of the stellar dynamo, fast-rotators are expected to exhibit high-latitude active regions, and vice versa. High-latitude spots and flares have indeed been observed on fast-rotators, but low-latitude spots have also been observed. Localizing more flares on stars other than the Sun are needed to give better constraints on stellar dynamo models.

This thesis aims to measure the locations of strong, modulation-altering flares in scallop-shell stars to constrain the structure thought to be responsible for the modulation and gather more data points on localized flares. The favored hypothesis involves low-latitude material. As a result, interaction with this material is most likely to occur from low-latitude flares, which is unexpected based on current dynamo theory. This thesis seeks to show the potential of flares as powerful probes into the surrounding environments of potentially planet-hosting young M dwarfs and provides better constraints on stellar dynamo models for young M dwarfs and fast-rotators.

# 2 Stellar Activity of M dwarfs

## 2.1 M dwarf stars at the focus of the search for life

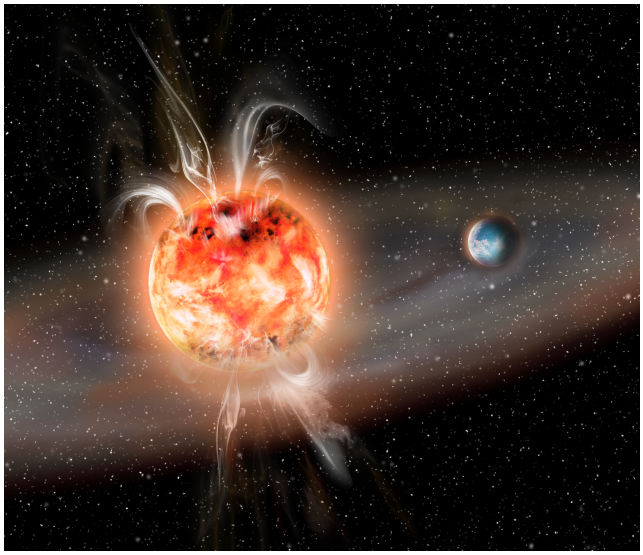

**Figure 2.1:** Illustration of high-latitude flares in an M dwarf with a close-in rocky planet orbiting it. While M dwarfs are important targets for exoplanet detections, flares from M dwarfs actively emit radiation and, if followed by shock-driving CMEs, expel particles that can alter and evaporate the atmospheres of planets that orbit them. However, studies show that M dwarfs tend to occur near the polar regions [e.g., Ili+21b], potentially sparing planets that orbit these stars from dangerous space weather events. Courtesy of AIP/J. Fohlmeister.

M dwarfs are stars that are cooler, smaller, and less massive than our Sun, with masses of $0.08 - 0.55\,M_{\odot}$ and effective temperatures of $2500 - 4000$ K [PM13]. They occupy the bottom part of the main sequence in the Hertzsprung-Russel diagram and are known as the most common stars in our Galaxy, making up approximately 75% of the stellar population [e.g., Boc+10]. Their low surface temperature results in their spectra to be dominated by molecular bands and their radiation peaked in the near-infrared (NIR). The interior structure of M dwarfs undergoes a transition at $\approx 0.35 M_{\odot}$ [CB97], at spectral type M4V, from a partially-convective interior structure to a fully-convective one. This divides M dwarfs into two main groups. Partially-convective M dwarfs have a thick outer convective envelope and radiative core, similar to solar-like stars. On the other hand, fully-convective M dwarfs have both outer convective envelope and core, similar to brown dwarfs and giant planets. This transition raises question how they differ in terms of generating magnetic fields.

M dwarfs are important targets for exoplanet detection for two main reasons.

First, their small, cool nature makes it easier to detect rocky exoplanets in their habitable zones. Their low effective temperature and luminosity makes their habitable zones (HZ), ranges of distance where liquid water may exist on the surface orbiting rocky exoplanets, much closer to the host star [e.g., KWR93]. This means that rocky exoplanets in these regions have short orbital periods and large radial velocity amplitudes, which eases detection through radial velocity measurement. Additionally, M dwarfs' small radii results in a higher planet-to-star ratio for rocky exoplanets in the habitable zones, which, when coupled with their low luminosity, makes the decrease in brightness during a planetary transit more noticeable.

Second, M dwarfs have long evolutionary timescales. The lifetime of core hydrogen burning for stars is proportionally inverse to their initial mass. This is because the reaction rate of hydrogen fusion scales with the temperature of the core: the hotter the core, which scales with stellar mass, the shorter the star's lifetime in the main sequence [e.g., Ibe67; Ibe74]. Therefore, both partially- and fully-convective M dwarfs evolve much slower than their more massive counterparts, such as the Sun. In fact, fully-convective M dwarfs have a main sequence timescale in the order of $\sim 10^{12}$ years [e.g., ABL05] and are thought to never evolve into a red giant phase [e.g., LBA97]. Therefore, M dwarfs offer long timescales for complex life to evolve within their planetary system.

While the close distance of the habitable zone makes them detectable with the commonly-used methods, they come with a high cost for the orbiting exoplanets: they are also closer to host stars that exhibit strong magnetic activity (see Figure 2.1). To understand why this is the case and what it means for the orbiting exoplanets, Section 2.2 discuss the processes that generate magnetic fields in M dwarfs and the role of stellar rotation. This is followed by Section 2.3, that discusses the manifestations of these magnetic fields, with a focus on flares, as one of the few directly observable phenomena in stars other than our Sun, and how flare latitudes can be used to magnetic field topology and stellar dynamo processes. Finally, Section 3 focuses on a class of young M dwarfs with unique geometries that offer an opportunity to probe the environments of potentially planet-hosting M dwarfs using flares.

## 2.2 Stellar magnetic dynamo

Stars generate magnetic fields through a dynamo: the conversion of kinetic energy into magnetic energy. In a simple dynamo on a bike, this would be converting the energy of a spinning wheel into magnetic energy, which then generates electric current that powers the lights. In stars, the magnetic dynamo is powered mainly by stellar rotation. Stars rotate on its axis and this has been known as early as the 1600s, when Galileo Galilei observed sunspots appeared to move. Not only that, the Sun does not rotate as a solid body; it exhibits differential rotation. This means the rotation speed of the surface of the Sun is a function its latitude, where it peaks at the equator [Car63]. The combination of differential rotation and the turbulence from convective motions and stellar rotation rate are thought to be the main driver

of the magnetic dynamo on solar-like stars, known as the $\alpha\Omega$-dynamo.

The $\alpha\Omega$-dynamo has been largely successful in explaining the magnetic activity and cycles of the Sun, although many details remain uncertain [see CS23; Oss03, and references therein]. The main idea is that stars inherit weak fossil magnetic fields at their formation, and the task of a stellar dynamo is to amplify and regenerate any existing magnetic field. In this process, differential rotation converts a poloidal field into a toroidal one at the transition region between the radiative core and the outer convective envelope, known as the $\Omega$-effect. Meanwhile, the Coriolis force from stellar rotation that is acting on rising turbulent fluid from convective motions generates a poloidal field from a toroidal one, known as the $\alpha$-effect. For stars with radiative core, magnetic flux tubes are thought to be generated in the boundary regions between the radiative core and convective envelope, where differential rotation is the strongest [Par55].

The $\alpha\Omega$-dynamo applies to partially convective M dwarfs, but fully convective M dwarfs require a different dynamo mechanism that operates without a radiative core. The $\alpha^2$-dynamo has been suggested as a solution for fully convective stars [e.g., CK06], where the $\alpha$-effect is the dominant process generating stellar magnetic fields. This means that the $\alpha^2$-dynamo depends on the strength of the Coriolis force acting on the turbulent fluid, which is largely dependent on the stellar rotation rate, with minimal to negligible influence from differential rotation. Consequently, it is generally expected that the faster a star rotates, the stronger its large-scale magnetic field becomes.

As stars age, they lose angular momentum and spin down, leading to a gradual decline in their magnetic field strength and activity [e.g., Bar03; Kra67]. However, M dwarfs in particular retain their fast rotation for much longer than their more massive counterparts [e.g., Irw+11; New+16]. As a result, for the same age, M dwarfs are known to exhibit stronger magnetic fields, driven by their fast rotation. This has been observed both through direct measurements of large-scale magnetic fields via Zeeman effects [see Koc21, and references therein] and observations of stronger and more frequent magnetically-driven phenomena.

## 2.3 Stellar activity and flares

Stellar magnetic activity, often referred to as stellar activity, is an umbrella term for all magnetically-driven phenomena observed in stars with outer convective envelopes. These include starspots, flares, coronal mass ejections (CMEs), and emissions from the stellar chromosphere and corona. They are generally powered by small-scale variations in the magnetic fields on the stellar atmosphere. Naturally, higher magnetic activity is caused by stronger magnetic fields. From the dependence of stellar rotation on the stellar dynamo, a relation between rotation and stellar activity is observed and studied [e.g., New+17; RJG12; Wri+11], with the general idea that stars with faster rotation generate higher stellar activity and vice versa.

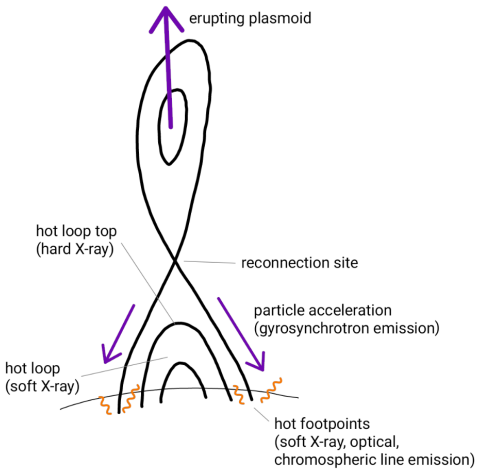


**Figure 2.2:** Simple illustration of processes and features in the standard model of solar and stellar flares. The hot loop top produces emissions in the hard X-ray (HXR), while emissions in the soft X-ray (SXR) are from the hot loop. The plasmoid (hot plasma) ejected after the reconnection becomes a CME. The magenta arrows indicate particles accelerated up- and downwards from the re-connection site. From Ilin [Ili22].

Out of the many observed phenomena from magnetic activity we see in our Sun, flares are one of the few that we can directly observe in other stars. Flares are explosive releases of magnetic energy due to magnetic reconnection in the stellar atmosphere. How a flare and its subsequent events occur is commonly based on the CSHKP model [Car64; Hir74; KP76; Stu66]. The standard picture involves a closed magnetic loop emerging from the stellar interior that extends to the corona and is anchored at footpoints on the stellar surface with opposite magnetic polarities (see Figure 2.2). Over time, convective motions of the stellar surface twist and tangle the magnetic loop, increasing tension on the magnetic field lines and, consequently, the magnetic field strength. At some point, magnetic reconnection occurs, reconfiguring the magnetic field into a lower-energy state and releasing magnetic energy into the environment. Due to this underlying process, flares are quasi-stochastic and occur preferably in magnetically-complex active regions [see Ben17].

Flares are observable almost across the entire electromagnetic radiation spectrum, from radio to gamma rays [see BG10, and Figure 2.3]. The energy release from the reconnection accelerate surrounding particles, both upwards, away from the star, and downwards to the stellar surface. The accelerated particles then emit non-thermal radiation and dissipate energy by heating the surrounding atmospheric layers they pass through which gives thermal radiation. Flare emissions from different wavelength regimes probe these processes in different layers of the stellar atmosphere, from the photosphere to the corona. In favorable cases, a flare is followed by an erupting filament from the reconnection, which would then be the core of a coronal mass ejection (CME) that further accelerates surrounding particles and give rise to stellar energetic particle events (SEPs).

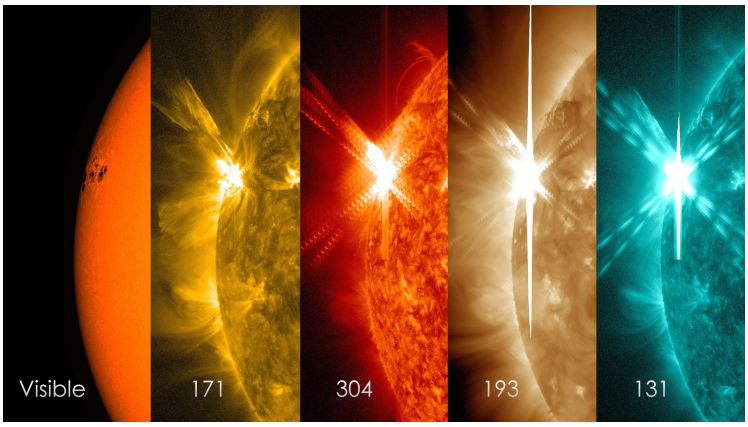


**Figure 2.3:** A solar flare captured in different wavelengths. From left to right, as labeled on each image, the wavelengths are: optical, 171 Å, 304 Å, 193 Å, and 131 Å. Each wavelength has been colorized. While the flare is not visible in the optical, or white light, a spot can be seen at the location where the flare occurs in the other wavelengths. Courtesy of NASA/GSFC/SDO.

Flares on M dwarfs are thought to originate from the same process as solar flares [see Kow24]. However, When comparing solar and stellar flares, flares on M dwarfs are approximately $10^2 - 10^4$ times more powerful than the largest solar flares [e.g., Gün+20]. M dwarfs also flare up to 1000 times more frequently than the Sun for flares of the same energy [Loy+18]. The highly energetic nature of M dwarf flares can result in stronger heating of planetary atmospheres [e.g., AM21] and the stripping of atmospheric layers from energetic particles [Che+20a; Seg+10; Til+19], contributing to atmospheric loss. However, high-energy radiation may be essential for the emergence of life, as ultraviolet (UV) light plays a key role in prebiotic photochemistry, particularly in the origin of RNA [Rim+18; RWS17]. Stellar radiation from M dwarfs alone is thought to produce insufficient UV flux for life [Spi+23; Spi+24]. To date, it is still not clear how these extremely high energies affect the habitability of exoplanets in their orbit.

### 2.3.1 White-light flares

Section 2.1 and 2.3 have established the urgency to study stellar activity, especially the high energetic flares, to get a the full picture of how life may look like in M dwarfs star-planet systems. However, flares occur randomly in time and may require observations over multiple nights to catch a single event. This makes flare observations challenging because not a lot of telescopes can afford to lose valuable time in waiting. Difficult monitoring campaigns may return only a few hundred flare lightcurves [e.g., Hil+10; Mof74] and focused studies revolved around already-known flaring stars [e.g., HP91].

This changed with the launch of space telescopes, particularly Kepler [Bor+10] and the Transiting Exoplanet Survey Satellite [TESS; Ric+14]. Continuous, photometric all-sky monitoring by these telescopes enabled the detection of thousands of flaring stars with hundreds of thousands of individual flare events (Figure 2.4).

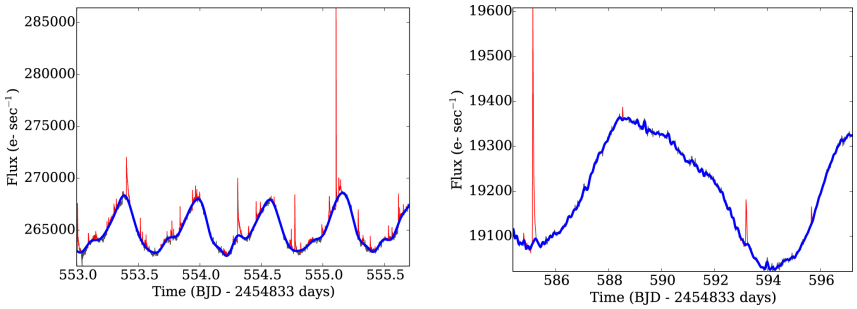


**Figure 2.4:** Example of two flare stars from Kepler observations. Left: Short-cadence data from the well-studied M dwarf KIC 9726699 (GJ 1243). Right: Long-cadence data for KIC 6224062. The blue lines represent the quiescent lightcurve model, or the star's modulation pattern, which in this case is caused by spots. The recovered flares are shown in red. From Davenport [Dav16].

This also allowed the community to study stellar flare parameters with statistically significant number of samples, including flare rates and energy distributions of different spectral types [e.g., Dav16; Gün+20; Pie+22] and ages [e.g., Ili+19; Ili+21a].

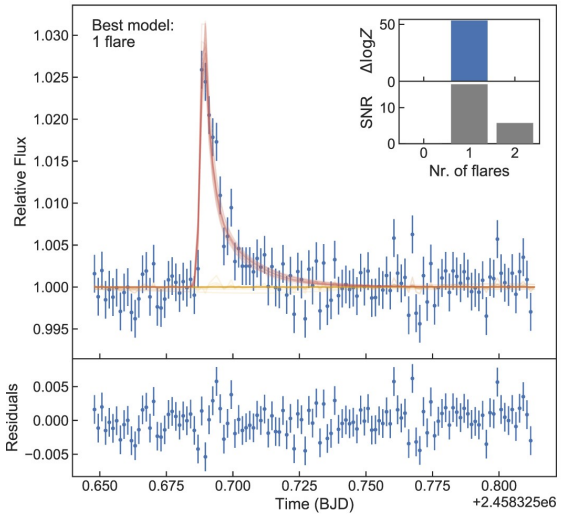


**Figure 2.5:** A classical flare lightcurve from TIC 144217628. The red curves represent the best model for the flare. This image illustrates how a classical flare has a distinct morphology that features a impulsive phase, where its brightness increases rapidly, followed by a gradual exponential decay phase. From Günther et al. [Gün+20].

Flares that were observed using Kepler and TESS are called white-light flares[1]. They are flares with emissions visible in the optical continuum observed using broad passbands, e.g., TESS covers a wavelength range of $6,000 - 10,000$. White-light flares, along with their near-UV (NUV) counterparts, are known for their dramatic impulsive phase followed by a long, gradual decay that can last for many hours. This characteristic description of flare phenomena creates a standard model

1 For clarity purposes, the term "white-light flare" in this essay is used to refer to optical flares. Both terms are used interchangeably.

for flares, explored by Davenport et al. [Dav+14]. This standard model, hereafter referred to as classical flares, is based on morphological studies of flares on the star GJ 1243. An example of how a classical flare looks like in detail can be seen in Figure 2.5. However, observations from TESS reveal that stellar flares exhibit a variety of morphologies [HM22], ranging from quasi-periodic pulsations [Ram+21] to more complex shapes, such as an additional bump during the gradual decay phase, known as a peak-bump flare [Yan+23, Figure 2.6].

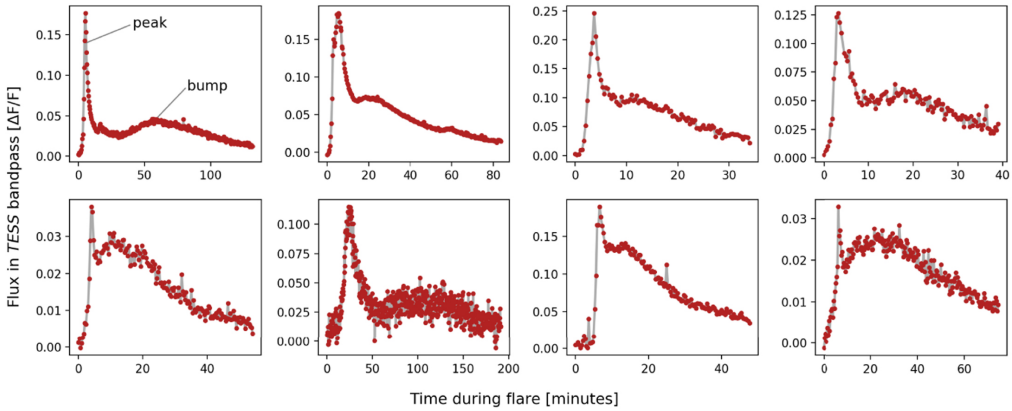


**Figure 2.6:** Examples of "peak-bump" flares and how they differ from the classical flare in Figure 2.5. These flares are characterized by a large, impulsive phase, similar to classical flares, followed by a lower-amplitude, less-impulsive Gaussian peak before decaying. Peak-bump flares are modeled by adding a Gaussian bump on top of a classical flare. Several hypotheses have been proposed to explain the cause of the Gaussian peak or bump, including radiative backwarming of the photosphere and coronal rain. From Howard et al. [How+20].

The photometric lightcurves of white-light flares are powered by continuum and line emission, which may result in different morphologies depending on the specific processes. Nevertheless, generally they are thought to originate from thermal radiation from the flare footpoints and typically modeled with a photospheric blackbody radiation with temperatures around $T \sim 10,000$ K [e.g., HP91; Kow+13], although both higher [How+20] and lower [Maa+22] temperatures have also been observed. However, recent studies have put this paradigm into question. Optically-thin hydrogen-recombination spectrum originating in the chromosphere are proposed as an alternative [Sim+24], but still falls short in describing the observed spectra [Kow+25]. The precise radiation source and processes of white-light stellar flares remain as one of the most enigmatic aspects of stellar flares. More observations to accurately account flare radiation are needed to predict the effect of flaring activity on the habitability of exoplanets.

### 2.3.2 Flaring latitudes as probes of stellar magnetic topology

Another important aspect of flares is their location. On the Sun, flares typically occur in magnetically-complex active regions, such as sunspots [STZ00, see Figure 2.3]. These sunspots follow a well-studied cyclic latitudinal variation throughout the solar cycle, forming a pattern known as the butterfly diagram [Gne77]. This

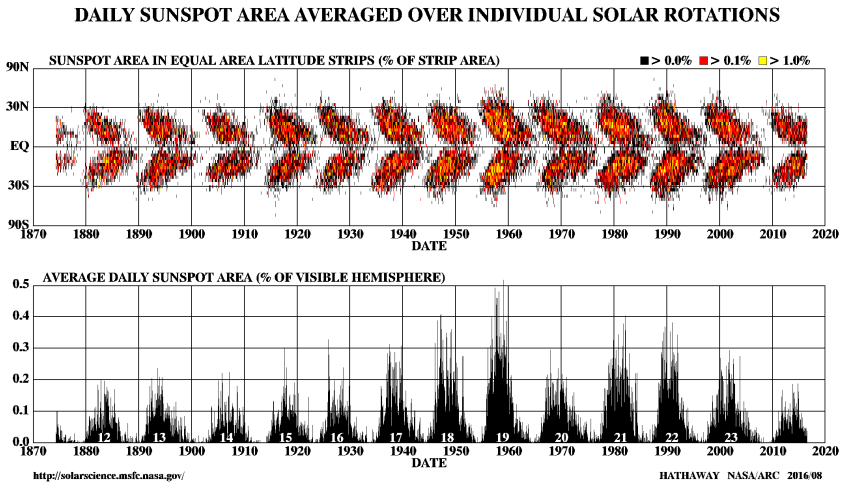


**Figure 2.7:** The sunspot "butterfly diagram." Top: Fractional coverage of sunspots as a function of solar latitude. Bottom: Fractional coverage of sunspots as a function of time, illustrating the 11-year solar cycle. The butterfly diagram reveals a strict band of preferential active latitudes on the Sun, ranging from -30° to 30°. The sunspot coverage map over time also illustrates that high magnetic activity, during solar maximum, is marked by large spots coverage. Courtesy of D. Hathaway, NASA/MSFC.

cycle, seen in Figure 2.7, show the Sun has a strong preferential active latitudes near the equator, and solar flares are found to follow a similar distribution [Zha+07]. Active regions, sunspots, and flares originate from the emergence of magnetic flux tubes from the solar interior. As a result, the butterfly diagram serves as a key observational constraint on solar dynamo theory.

On other stars, studying the location of active regions is not an easy feat. Generally, Zeeman Doppler Imaging [ZDI; see Koc16] is used to map the surface distribution of starspots and magnetic field vectors for stars that lack spatial resolution. If stellar flares occur in active regions similarly to solar flares, localizing flare latitudes can, in turn, provide crucial insights into how stellar dynamos work. They can also act as location tracers for potential CME-driven energetic particle events that may impact the orbiting exoplanets, particularly for stars where ZDI is not feasible.

### Rotation periods and preferential active latitudes

In general, fast-rotating stars are expected to exhibit stronger magnetic fields (Section 2.2). Another particularly intriguing consequence of stellar rotation in the dynamo process is that fast-rotating stars are expected to develop high-latitude active regions [Gas+13; SS92; WB16; Yad+15], seen in Figure 2.8. Multiple ZDI studies of starspots show this trend [see, e.g., Str09]. However, the observational evidence from ZDI could be influenced by a systematic bias, as ZDI may struggle to detect low-latitude active regions. In contrast, low-latitude spots are detected through spot transits [see Sil03], i.e., an exoplanet transiting over a spotted region, even in fast-rotating stars [e.g., Dai+18; NV20; Sil+10]. This raises questions whether

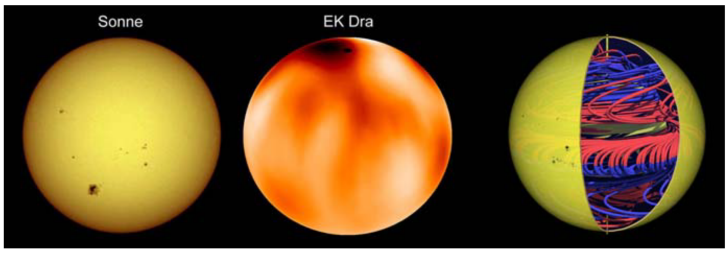


**Figure 2.8:** A comparison of the Sun (left) with EK Dra (middle), a young solar analogue approximately 100 Myr old with a rotation period ten times faster than the present-day Sun. The image of EK Dra is constructed from data by Strassmeier and Rice [SR98]. EK Dra shows significantly larger cool spots, which also appear at higher latitudes compared to its solar counterparts. The single black dot on EK Dra represents the pole of its rotation axis, not a stellar spot. Right: A simulation of the solar dynamo in the stellar interior, producing a dipole-like magnetic field structure. Blue represents inward-pointing fields, while red indicates outward-pointing fields. If individual flux-tube bundles reach the stellar surface, they emerge as spots. From Strassmeier [Str09].

fast-rotators truly exhibit strong preferential active latitudes.

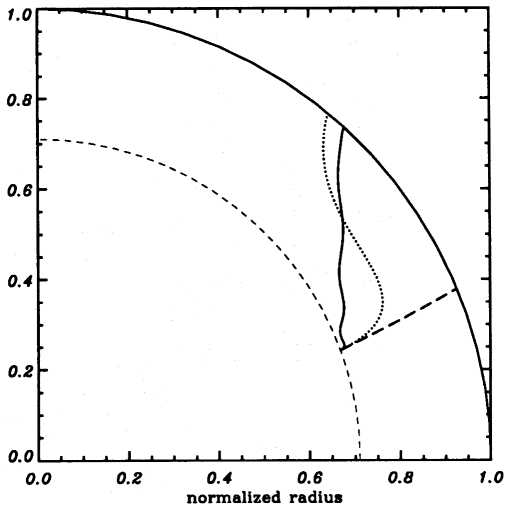


**Figure 2.9:** Motion of a simulated toroidal flux tube with initial strength of $B = 2 \times 10^5$ in the solar interior with different rotational periods. The starting latitude is 20°. The different curves represent different rotation rates: the dashed curve corresponds to the solar rotation period of 26 days, the dotted curve to 9 days, and the solid curve to 3 days. For the solar rotation period, the flux tube rises radially. However, for shorter periods, the Coriolis force becomes important. At a rotation period of 3 days, the flux tube is nearly parallel to the rotation axis. From [SS92].

The reasoning for expecting high-latitude active regions for fast-rotators involves the forces that govern stellar dynamo. The location of active regions are determined by the emerging locations of the magnetic flux tubes. Magnetic flux tubes rise from the stellar interior, driven by buoyancy from convective motions. The balance between buoyancy and the Coriolis force determines their path: if

buoyancy dominates, the flux tubes rise radially to the surface, whereas if the Coriolis force dominates, they follow a path parallel to the stellar rotation axis. In other words, fast-rotating stars, where the Coriolis force is stronger, are expected to have high-latitude active regions because their flux tubes that originate at low latitudes are deflected and then emerging at higher latitudes [CG87]. This is illustrated in Figure 2.9. Consequently, if stellar flares are described by processes similar to those on the Sun, a relationship between stellar rotation rate and flaring latitudes can be expected.

### Flare localization

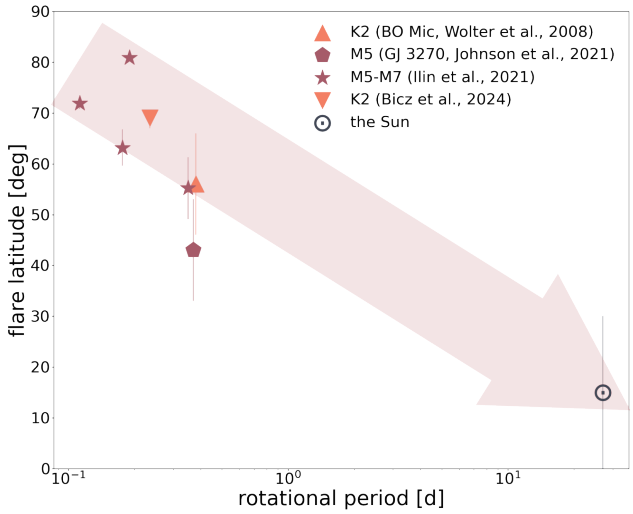


**Figure 2.10:** All localized flares as a function of their rotational period. Most of the localized flares with rotation shorter than the solar period have high-latitude flares. This suggested a possible connection between stellar flare latitudes and rotational period, shown in the pink arrow. However, more data is needed to confirm any relationship between the two parameters.

Most flare localization studies are serendipitous individual events, and these can generally be categorized into two main methods. The first involves direct imaging, either through Doppler shift or radio observations. Wolter et al. [Wol+08] and Johnson et al. [Joh+21] used Doppler imaging to localize flares on a K-dwarf and an M-dwarf, respectively, determining flare latitudes of 56° and 43°. On the other hand, Peterson et al. [Pet+10] used radio imaging to capture a coronal loop, finding that active regions occurred near the poles of the secondary star. The second method uses the relative position of another celestial object, such as a binary companion. Schmitt and Favata [SF99] localized a giant X-ray flare in a binary system consisting of an A-type and F-type star by analyzing lightcurve eclipses, while Martin et al. [Mar+24] used a similar approach in an M-dwarf binary observed by TESS. Both studies identified flares near the poles of the stars, as the flare lightcurves remained visible during eclipses from the stars' companions. There is also evidence of a giant CME following the flare in Schmitt and Favata [SF99], showing that

high-latitude CMEs could in principal happen.

The first systematic search for localizable flares was conducted by Ilin et al. [Ili+21b], using a new method that takes advantages of long-duration flares that are modulated by the star's rotation. The lightcurves of these flares have a distinct shape, characterized by the movement in and out of view of the flaring region. Ilin et al. [Ili+21b] combed through lightcurves of fast-rotating fully-convective M dwarfs from the first two years of TESS and identified rotationally-modulated flares. All of the localized flares occurred at high-latitudes, ranging from 55° to 81°, much higher than typical solar latitudes. Ilin et al. [Ili+23] further expanded the methods for localizing flares by demonstrating that, even without rotationally-modulated flares, flaring latitudes can be estimated through an analysis of spot configurations and the timing between flares.

All reported localized flares occur at latitudes higher than typical solar flares, i.e., well above 30° (Figure 2.10). All of these stars rotate faster than our Sun. These findings, so far, suggest that flares in fast-rotating stars flare closer to the poles than the equator, aligning with the known dynamo theory.

# 3 Scallop-shell Stars

M dwarfs retain their fast rotation much longer than their more massive counterparts [Bar03; Irw+11; New+16]. As a result, young M dwarfs are often observed to rotate rapidly, with rotation periods shorter than 2 days [e.g., Pop+21; Pop+23]. This rapid rotation leads to stronger magnetic field generation and higher magnetic activity (Section 2.2 and 2.3). In turn, stronger magnetic fields contribute to more magnetically-complex active regions, such as higher coverage of starspots (see Figure 2.7).

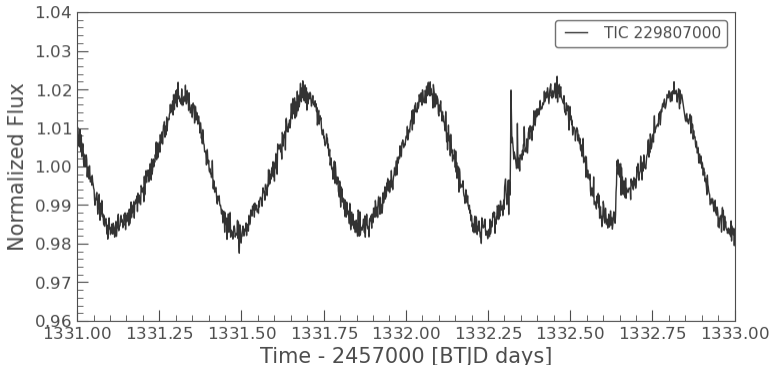


**Figure 3.1:** A lighcurve of TIC 229807000, a spotted M dwarf [Doy+19]. The configuration of spots on the star creates a smooth sinusoidal modulation.

Young M dwarfs often show signs of starspots. In photometric observations (Figure 3.1), spots result in a smooth, semi-sinusoidal rotational modulation. Stars that exhibit more complex rotational modulation can usually be explained by a more complex configuration of spots: with different sizes and locations [e.g., Rap+14; Str+17]. However, with the launches of all-sky surveys, e.g., Kepler and TESS, more and more young M dwarfs are found to have complex rotational modulation that can not be explained by spots alone.

Dipper and burster stars [e.g., CH18; Cod+17; Mor+11] are one of the known stars to deviate from the norm. These stars exhibit fading (dips) and brightening (bursts) events that recur periodically, quasi-periodically, or without any apparent underlying pattern (Figure 3.2). They, and five other morphology classes [Cod+14], were found in clusters and associations of young disk-bearing objects with IR excess. This indicates that the presence of circumstellar material is responsible for their photometric variability, either through accretion or obscuration from the disk.

Despite efforts to classify the lightcurve morphology of young M dwarfs into seven categories, some stars still do not fit within this framework. In particular, Kepler/K2 observations of star-forming regions revealed another distinct group:

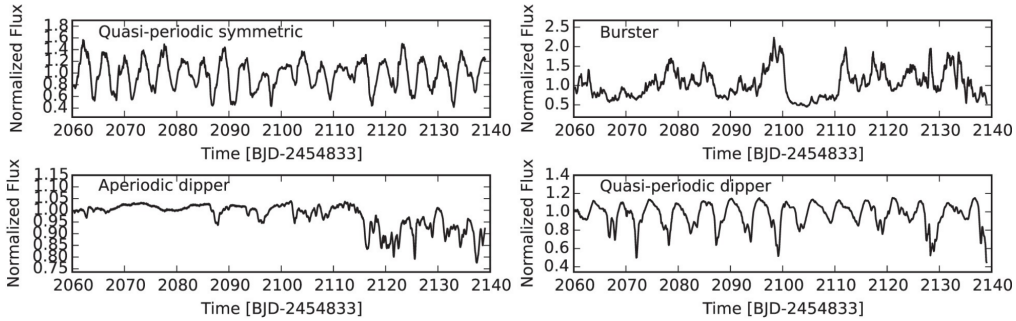


**Figure 3.2:** Examples of different light-curve morphologies observed in disk-bearing stars. The lightcurves show modulation that does not resemble the smooth sinusoidal variation caused by spots, as shown in Figure 3.1. Instead, they have more irregular shapes with sharp peaks and dips. While some display quasi-periodic behavior, others appear stochastic. These variations are attributed to obscuration by the opaque disk and accretion bursts. From Cody and Hillenbrand [CH18].

scallop-shell stars [Sta+17]. Unlike dippers and bursters, their modulation pattern does not fit the with modulation from spots or disks. Instead, they exhibit strictly periodic modulation with complex, scallop-shell-like patterns (Figure 3.3). The cause of their modulation is still unknown. Currently, there are around ~ 100 scallop-shell stars found from more Kepler/K2 [Sta+17; Sta+18b] observations and TESS [Bou+24; Sta+21; Zha+19]. Other than the name scallop-shell stars, they are also known as "complex rotators" and complex periodic variables (CPVs).

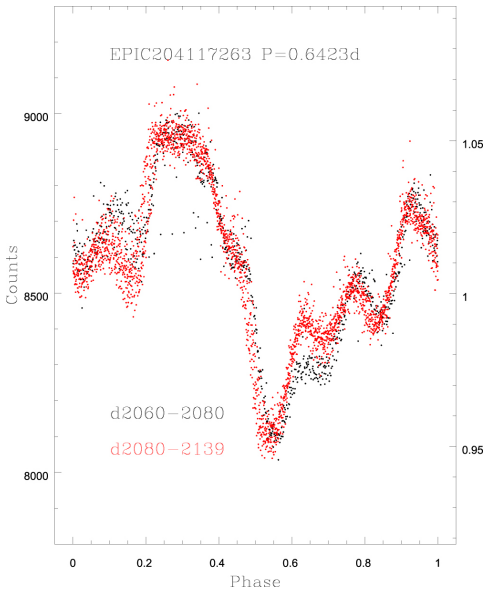


**Figure 3.3:** Phased lightcurve of EPIC 204117263, one of the first scallop-shell stars to be identified. The phased lightcurve, or modulation pattern, exhibits a wave-like shape resembling a scallop shell. Black points represent data from days 2060–2080 of the Kepler mission, while red points correspond to data collected after day 2080. Although there are some small changes in the modulation pattern, it remained generally stable throughout the entire K2 campaign. From Stauffer et al. [Sta+17].

It is now clear that, while they are uncommon, scallop-shell stars are not particularly rare. The favored hypotheses of their unique characteristics (Section 3.1) require material near the equator (Section 3.2). If this hypothesis were true, accounting for their rotation axes suggests that 30% of fast-rotating M dwarfs should have equatorial material [Gün+22]. Therefore, scallop-shell stars offer a unique view of the stellar environment in young, potentially planet-hosting M dwarfs in ways that were previously inaccessible.

## 3.1 Characteristic and observations

Since their discovery, scallop-shell stars are found to have several distinct characteristics and observational features that separate them from other variable stars. There are four main features of scallop-shell stars, each of them has to be accounted to give a unified and sound explanation of the cause of the unexplained modulation.

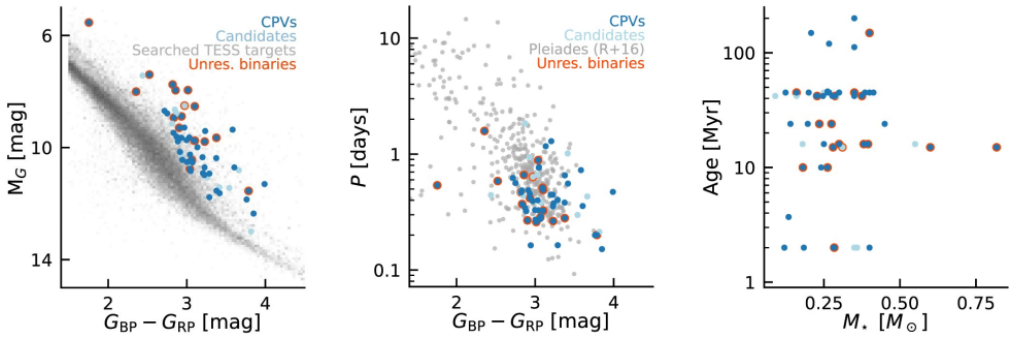


**Figure 3.4:** Properties of scallop-shell stars (CPVs) from Bouma et al. [Bou+24], showing that scallop-shell stars are mostly pre-main-sequence M dwarfs with ages younger than ≈ 150 Myr and periods shorter than ≈ 1 day. Dark blue dots represent confirmed scallop-shell stars, light blue dots indicate ambiguous scallop-shells, and unresolved binaries are shown as ringed objects. Left: Distribution of scallop-shell stars compared to the entire search target. Middle: Comparison of scallop-shell stars with the Pleiades. Right: Distribution of age and mass of scallop-shell stars.

**Scallop-shell stars are young, fast-rotating M dwarfs.** Most of them are found in star-forming regions and identified as pre-main-sequence M dwarfs with ages from ≈ 5 – 200 million years. They are observed to comprise ≈ 1 – 3% of young M dwarfs in that age range [Gün+22; Reb+22]. from the lack of detected scallop-shell stars in the Hyades and Praesepe suggest the phenomena of scallop-shell stars only persist for the first few hundreds million years [Bou+24]. Scallop-shell stars are also fast-rotators, with period range from 0.2 – 2 days (Figure 3.4). However, while early discoveries of scallop-shell stars showed these objects do not have period longer than 2 days [e.g., Sta+17; Zha+19], more recent catalog of scallop-shell stars [Bou+24] used 2 days as a manual cut-off. Whether scallop-shell stars can have longer periods requires studying larger samples.

**The modulation patterns are complex, with sharp peaks and dips.** Scallop-shell stars are found from the distinct complex modulation in optical observations.

They are described to have patterns that look like the rim of a scallop-shell. Similar to dipper and burster stars, scallop-shell stars cannot be explained with starspots alone because they exhibit modulation pattern with "jagged" and/or "notched" features (Figure 3.5) in contrast to the smooth sinusoidal modulation of spots (Figure 3.1). However, they can be approximated with sinusoidal modulation in the first order, indicating that spots may also be involved. The complex modulation patterns are also highly structured and well-defined when the lightcurves are phased. The amplitudes of their dips range from a few percent to around 10% and are generally asymmetric.

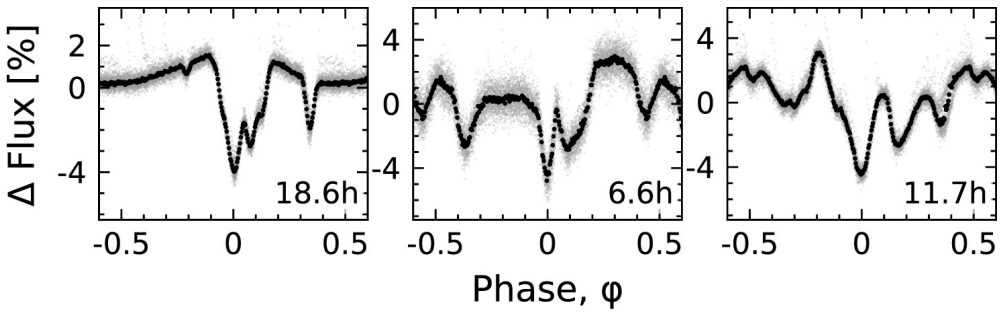


**Figure 3.5:** Phased lightcurves of three scallop-shell stars observed with TESS. The labeled number represent the rotation period of each star in hours. Each panel shows the average of the data accumulated over one month, relative to the stellar brightness. Gray circles are raw two minute cadence data, while black circles are binned to 300 points per cycle. The objects are, from left to right, TIC 402980664, TIC 94088626, and TIC 425933644. From Bouma et al. [Bou+24].

**The modulation patterns are strictly periodic and generally stable.** While scallop-shell stars share the complex pattern of dipper and burster stars, their strict periodicity is what sets them apart. The modulation appear to be stable over timescales of at least one year [Gün+22] but not more than 2 years [Pop+23, see Figure 3.6], while some minor features may appear and disappear over a few weeks. This stability suggests that the occulting structure or material should be stable over the course of months. The timescale also seems to be aligned with the timescale of spot modulation for some young M dwarfs that appear to be constant from hundreds of days to years [DHH15; GCH17]. In contrast to its stability over a long timescale, some of the scallop-shell stars are observed to have changes in their modulation, even permanently, after a flare occurred [Bou+24; Sta+17; Zha+19, see Figure 3.7]. They can also take place without an associated flare. There is no clear correlation between flare characteristics and these switches, as both small and large flares can precede them.

**The modulations are color-dependent and more prominent in the blue.** Shown in Figure 3.8, observing the modulation through multi-passband filters show that scallop-shell stars have $1 - 2\times$ deeper flux variation in the blue bandpasses than red [e.g., Bou+20; Gün+22; Koe22]. This color dependency is consistent with reddening by dust and may be used to constrain the dust grain size. Interestingly, the majority of scallop-shell stars do not show significant IR excess that indicates

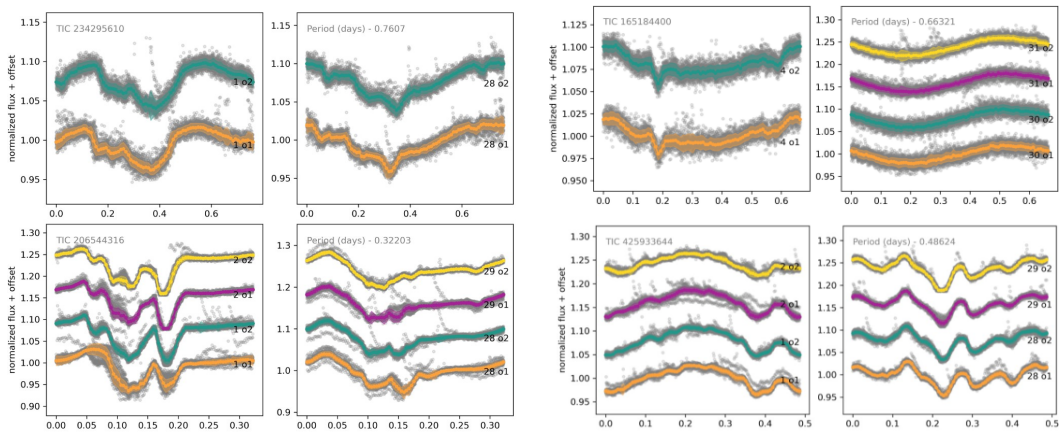


(a) (b)

**Figure 3.6:** Evolution of four scallop-shell stars observed by TESS, with each star's identifier labeled in the first column. The first column shows observations from Cycle 1, while the second column presents data from Cycle 3, corresponding to a two-year gap. Within each column, different sectors from the same cycle are plotted separately. Gray points represent raw data, while colored points show the median phased lightcurve. Changes in features are evident after two years. Panel (a): Features evolve over time, but similar patterns remain recognizable. Panel (b): The first row illustrates a star transitioning from a distinct scallop-shell pattern to a smooth, sinusoidal modulation typical of spots, effectively losing its scallop-shell characteristics. Conversely, the second row shows a star evolving from a semi-sinusoidal modulation into a scallop-shell pattern. From Popinchalk et al. [Pop+23].

dust disks as their main cause similar to dipper and burster stars [Bou+24]. Only a small number do show significant IR excess [Sta+17; Zha+19]. If dust were involved, this indicates that scallop-shell stars may have different grain size, density, and structure of dusts compared to disk-bearing objects.

## 3.2 Possible explanations

In the pursuit to understand the cause behind complex modulation of scallop-shell stars, Günther et al. [Gün+22] compiled, summarized, and scrutinized various hypotheses and their observation constraints. While there are indeed a quite number of suggested mechanisms, this section discusses only two, which are cosnidered as the two most promising ideas. Both of these ideas involve spots. Spots can explain the large modulation of scallop-shell stars, supported by the fact that their stability timescales are similar to those of starspots. Therefore, both ideas are primarily tasked to explain the sharp peaks, dips, and overall complexity of the modulation.

### 3.2.1 Co-rotating clouds and spots

Stauffer et al. [Sta+17] suggested that the modulation is caused by clouds of material near the Keplerian co-rotation radius (Figure 3.9). These clouds could qualitatively explain the sharp features and strict periodicity superimposed on the modulation of spots. The asymmetric, irregularly shaped dips can also be attributed to the cloud's distribution. The biggest challenge for this model is explaining how such

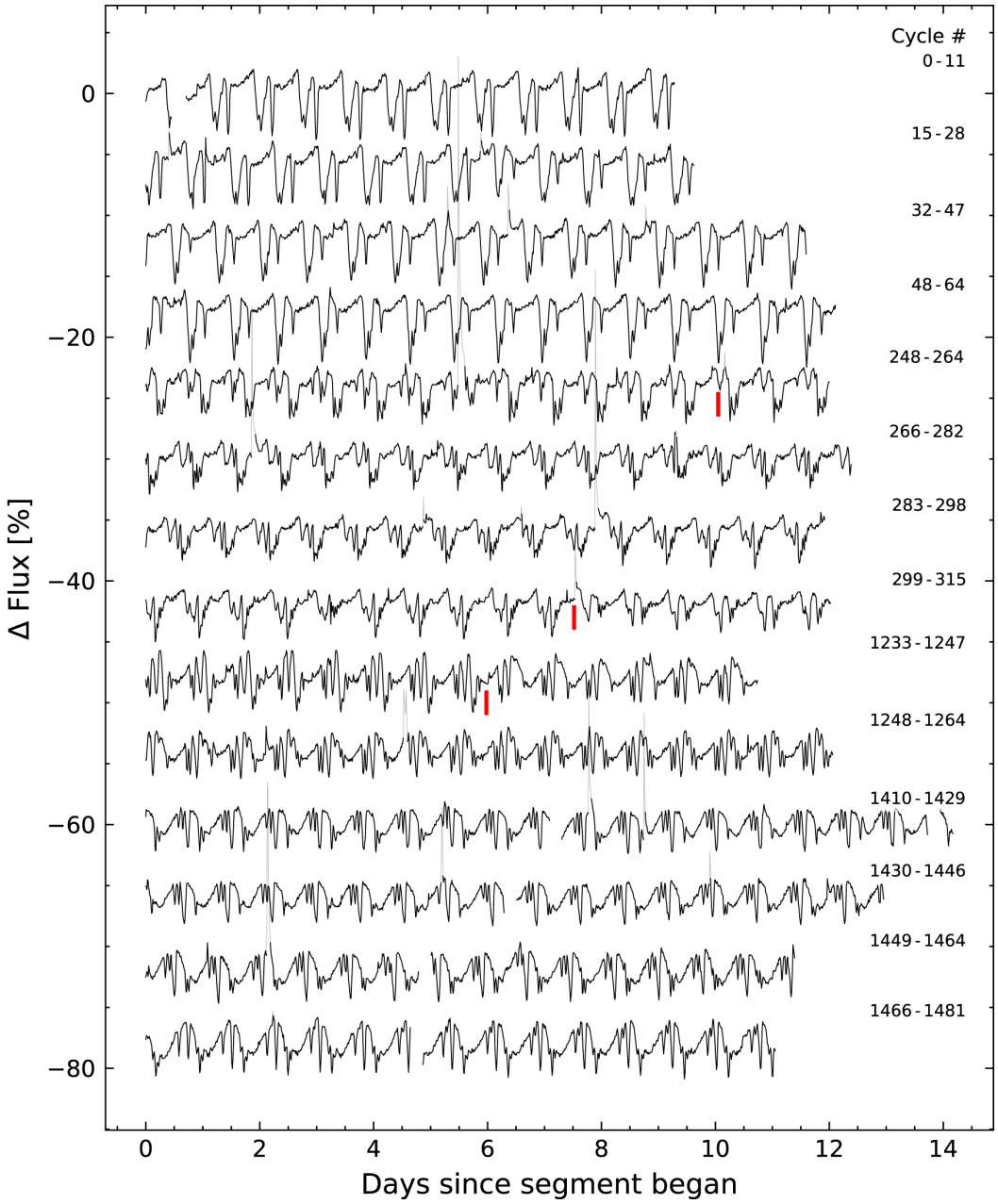


**Figure 3.7:** Remarkable lightcurve evolution of TIC 402980664 for over three years. Data were acquired in Sectors 18–19, 25–26, 53, and 57–58. Flares are colored in gray. The red vertical lines highlight instantaneous state, or pattern, changes. This can happen with or without a flare. From Bouma et al. [Bou+24].

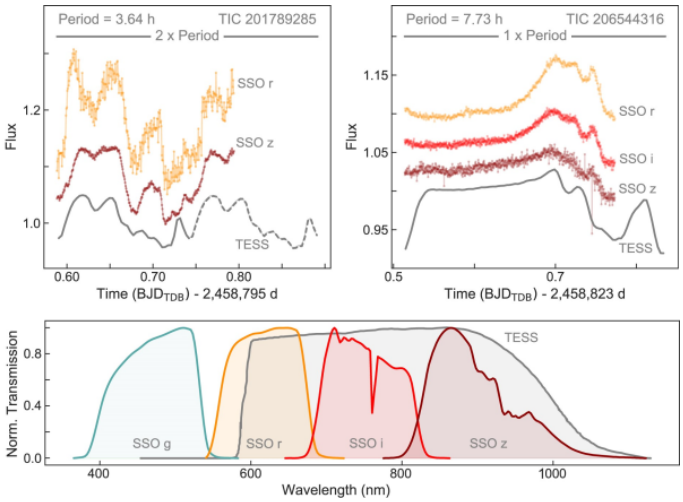


**Figure 3.8:** Comparison of multi-wavelength observations of two scallop-shell stars TIC 201789285 and TIC 206544316 (top) and the passbands used compared to TESS (bottom). There is a clear color dependency of the lightcurve, with features being much more prominent in bluer passbands. From Günther et al. [Gün+20].

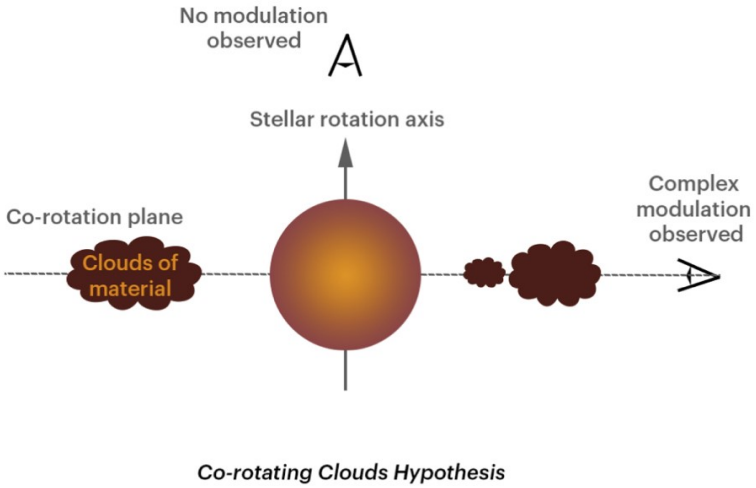


**Figure 3.9:** Illustration of the co-rotating cloud hypothesis by Stauffer et al. [Sta+17]. In this hypothesis, the clouds are magnetically trapped near the Kepler co-rotation radius. The illustration shows that the scallop-shell phenomena is dependent on how the star is inclined towards the observer. From Günther et al. [Gün+22].

clouds form in the co-rotating radius. The most favored explanation is that they are magnetically trapped [e.g., San+22]. This requires an understanding of what material gets trapped, how it becomes co-rotating, and how it gets trapped in the first place.

If the material is dust, it could account for the observed color dependency and the opacity needed to obscure the star. Variations in grain size and density might also determine whether the star exhibits IR excess. However, the crucial question is what mechanism allows dust clouds to be magnetically trapped. Sanderson et al. [San+22]

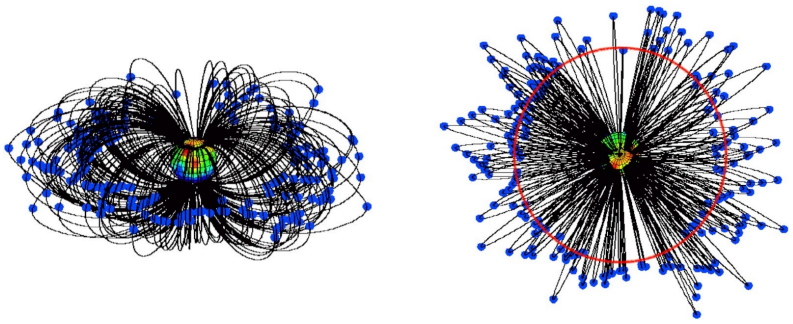

**Figure 3.10:** A model of the co-rotating cloud hypothesis. The model shows magnetic field structure of V374 Peg with dust-cloud locations shown as blue clumps. Left: observer's view at inclination 70°. Right: view from above the rotation axis, with co-rotation radius marked as a red circle. From Sanderson et al. [San+22].

proposed that these clouds originate from tidally disrupted or evaporating planetesimals [e.g., Gai+24]. As the dust enters the stellar corona, it becomes collisionally charged, couples to the magnetic field, and settles in magnetic stable points (Figure 3.10). These points are defined as stable gravitational-centrifugal potential minima within complex magnetic field configurations around rotating stars [Fer00; Jar+01]. Nevertheless, it remains unclear how dust at a few stellar radii remains stable for two years without evaporating or sublimating. More detailed spectroscopic observation of the star's continuum could help in confirming whether dust is involved.

If the material is gas or plasma, magnetically trapping ionized plasma might be more straightforward than trapping dust. This scenario comes from noting the similarity between scallop-shell stars and magnetic B stars, which are suggested to have circumstellar gas trapped within their co-rotating radius [TOG05]. The material could originate from CMEs confined by the stars' strong magnetic fields [Alv+18; Alv+19; Fra+19; Fra+22] or from the centrifugal breakout of prominences [DJ24; Pal+22]. Bouma et al. [Bou+24] even suggested that large prominences, rather than trapped gas clouds, could be responsible for the modulation. If gas cloud or prominence is responsible, then changes in H$\alpha$ signature in time should be expected with the phase of the modulation. However, the main issue with this scenario is opacity. Gas and plasma are optically thin, it is unclear how they could produce absorption of up to 10%.

### 3.2.2 Misaligned dust disk and spots

Zhan et al. [Zha+19] proposed a model in which one or more misaligned dust rings orbit the star and create a dust disk (Figure 3.11). Unlike magnetically trapped dust at the co-rotation radius, this model allows for stable periodic modulation over many years, with both spots and the dust disk contributing to optical color dependency. Although this model eliminates the need for trapped material at large distances, it requires young M dwarfs to host close-in, misaligned dust disks. This raises the question of why such disks persist until around 200 Myr, given that most young stars lose their disks after $\sim$ 10 Myr [PD24].

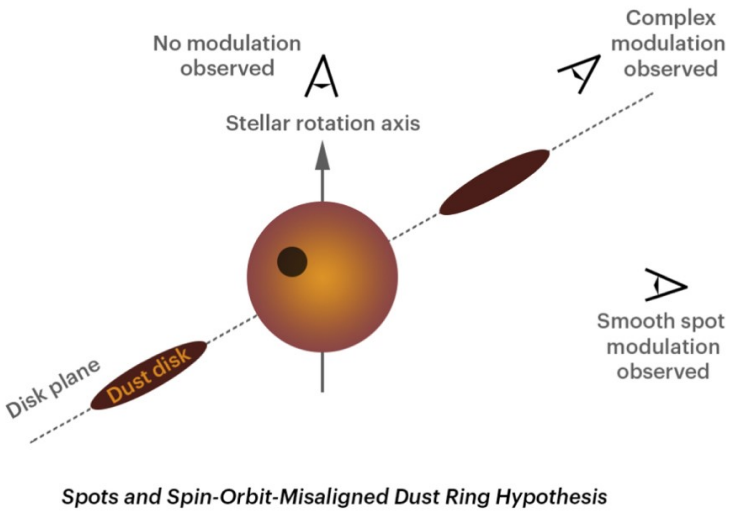


**Figure 3.11:** Illustration of the dust disk by Zhan et al. [Zha+19]. In this hypothesis, the modulation is caused by a misaligned dust disk. The illustration also shows that the scallop-shell phenomena is dependent on how the star is inclined towards the observer. From Günther et al. [Gün+22].

Several possibilities exist to explain this hypothesis. First, there is a distinction between primordial and debris disks. Primordial disks retain significant gas for planet formation, while debris disks lack substantial gas and typically appear in systems older than 10 Myr [Wya+15]. The disks around scallop-shell stars may be debris disks rather than star-forming primordial disks, which usually dissipate earlier. Notably, old disks have been observed around M dwarfs to even 45 Myr [Fla+19; Sil+20], known as Peter-Pan disks. Some of these still show accretion, suggesting that M dwarfs may retain primordial disks longer than expected. The next challenge is explaining their misalignment. Two possible mechanisms exist: first, perturbations from passing stars [e.g., Ros+14], and, second, spin-magnetic axis obliquity. If dust is magnetically confined, such an obliquity could lead to a misaligned disk. Observations confirm that young stars can exhibit spin-magnetic axis misalignment [see Bel+23, and references therein].

Despite its strengths, this model has several caveats. While old debris disks around M dwarfs have been observed until around ~ 45 Myr, it is still unclear how they could persist for 200 Myr. Additionally, Wyatt et al. [Wya+15] noted that debris disks are typically optically thin and exhibit IR excess [e.g., Sil+20], while the majority of the scallop-shell stars do not [Sta+17; Zha+19]. However, the properties of this dust disk, such as density and grain size, may differ from those of disk-bearing objects, potentially explaining why these stars do not exhibit significant IR excess like dippers and bursters. Peter Pan disks also show that M dwarfs can retain their accreting disks until ~ 45 Myr. The long timescale, up to 200 Myr, may represent the time it takes for some scallop-shell stars to evolve into debris disk systems.

# 4 Data and Methodology

## 4.1 Object of study: TIC 206544316

A scallop-shell star with a change in modulation pattern after a flare was found in TESS by Zhan et al. [Zha+19]. The flare shows a 4× increase in brightness. Hereafter, I refer to it as a giant flare. This makes the star a good candidate to study possible interactions between a flare and the material causing the modulation. The stellar properties of TIC 206544316 are given in Table 4.1.

| TIC 206544316 | |
|---|---|
| R.A. J2000 (deg) [1] | 18.41887 |
| Dec. J2000 (deg) [1] | -59.65975 |
| Spectral type [2] | M4.5V |
| $T_{\rm eff}$ (K) [3] | 3100 ± 100 |
| $d$ (pc) [1] | 42.85 ± 0.04 |
| Radius ($R_\odot$) [3] | 0.48 ± 0.04 |
| Mass ($M_\odot$) [3] | 0.22 |
| $T$ (mag) [4] | 11.63 ± 0.01 |
| $V$ (mag) [4] | 14.75 ± 0.15 |

**Table 4.1:** Stellar properties of the scallop-shell star TIC 206544316. (1) Gaia DR3 [Lin+21]; (2) via Pecaut and Mamajek [PM13]; (3) Günther et al. [Gün+22]; (4) TIC v8 [Sta+18a]. The effective temperature $T_{\rm eff}$ and spectral type is taken from observed values that include stellar activity while the stellar radius $R_*$ is taken from values without activity derived by Günther et al. [Gün+22].

To investigate whether the flare could actually be the cause of the modulation change, the flare latitude $\theta_f$ must be well constrained. This requires several statistically-confident stellar parameters, with the most important being the stellar inclination $i_*$. Geometrically, there is a degeneracy between the inclination of the stellar rotation axis $i_*$ and the flare latitude $\theta_f$. Therefore, stellar inclination $i_*$ has to be accurately defined to break the degeneracy and obtain a more reliable constraint on flare latitude $\theta_f$.

The first problem comes when there are two different values of $v \sin i_*$ for TIC 206544316 in the literature, as shown in Table 4.2. Unfortunately, neither measurements were reported with uncertainties. This makes it unclear whether

their values overlap and which projected rotational velocity $v \sin i_*$ and stellar inclination $i_*$ I should adopt. As a result, I decided to derive the stellar inclination $i_*$ independently in thesis (Section 4.5).

| $v \sin i_*$ | Source |
|---|---|
| ~ 70 km/s | Kraus et al. [Kra+14] |
| ~ 77 km/s | Zhan et al. [Zha+19] |

**Table 4.2:** Previously, the reported value from Kraus et al. [Kra+14] was 46.8 ± 5.4 km/s. This meant that there was almost a 30 km/s difference in the existing literature. Through a correspondence with the author, it was clarified that the reported quantity was actually the FWHM of the spectral-line broadening function and could not be used as $v \sin i_*$ directly. The correct $v \sin i_*$ value is around 70 km/s.

If constraining the flare latitude $\theta_f$ were a recipe, it would require three main ingredients: the flare light curve without stellar modulation (Section 4.6), a flare model to constrain $\theta_f$ (Section 4.7.2), and the stellar inclination $i_*$ (Section 4.5). Determining $i_*$ itself requires three stellar parameter: the rotation period $P_{\rm rot}$ (Section 4.4), the radius $R_*$, and the projected rotational velocity $v \sin i_*$ (Section 4.5.1). This section describes the data and methods I use to derive each of these parameters and models step by step, ultimately combining them to constrain $\theta_f$.

## 4.2 Observations and data

To derive all of the required parameters and datasets, I used both photometric and spectroscopic observations. I used photometric observations from TESS to analyze the lightcurves of TIC 206544316 and the giant flare, specifically to measure the stellar rotation period $P_{\rm rot}$ and obtaining the flare-only lightcurve. I then used spectroscopic observations to derive the projected roational velocity $v \sin i_*$, which is needed to determine the stellar inclination $i_*$. The method to derive $v \sin i_*$, (Section 4.5.1) requires spectra of the target star and a number of reference stars with low projected rotational velocity $v \sin i_*$. For the spectra of TIC 206544316, I used data from Gaia Radial Velocity Spectrometer [Gaia RVS; Cro+18] and the Magellan Inamori Kyocera Echelle [MIKE; Ber+03] spectrograph.

To select the reference stars, I imposed three main criteria: 1) the star has a similar spectral type with TIC 206544316, around M4.0V and M4.5V, 2) it has low $v \sin i_*$, around 2.5 km/s or lower, and 3) it was observed using Gaia RVS and a mid- to high-resolution spectrograph, with a data archive that is publicly accessible. I decided to use spectra from CARMENES [Qui+14], because several CARMENES CARMENES catalogs [e.g., Pas+19] reports $v \sin i_*$ values and has a public archive[2]. Cross-matching the available spectra in Gaia RVS and the CARMENES catalog resulted in four reference stars for TIC 206554316. Their stellar parameters can be

2 http://carmenes.cab.inta-csic.es/gto/welcome.action

seen in Table 4.3. Therefore, I used ten spectroscopic observations of five different stars observed with three different instruments.

| KARMN ID | J05366+112 | J08526+283 | J10416+376 | J11509+483 |
|---|---|---|---|---|
| Other identifier | PM J05366+1117 | $\rho$ Cnc B | GJ 1134 | GJ 1151 |
| R.A. J2000 (deg) | 84.16025 | 133.16792 | 160.39992 | 177.73050 |
| Dec J2000 (deg) | 11.29661 | 28.31528 | 37.60933 | 48.37322 |
| Spectral type | M4.0V | M4.5V | M4.0V | M4.5V |
| $v \sin i_*$ | 2.4 km/s | $< 2$ km/s | $< 2$ km/s | $< 2$ km/s |

**Table 4.3:** Reference stars with low $v \sin i_*$ to derive the $v \sin i_*$ of TIC 206544316. All stellar parameters in this table were obtained from Passegger et al. [Pas+19].

### 4.2.1 TESS

From TESS, I used the two-minute photometric data (two-minute cadence) of TIC 206544316 from Sector 1 and Sector 2. I used the lightcurves from the Presearch Data Conditioning pipeline [PD-CSAP_FLUX; Jen+16] that I accessed through `lightkurve` [Lig+18]. The lightcurve from Sector 1 was observed from July 25 - August 22, 2018, while for Sector 2 they were observed from August 23 - September 21, 2018. The giant flare is located in Sector 1 and I used the lightcurve from this sector as my main dataset for analyzing the flare lightcurve (see Section 4.6). For determining the stellar period $P_{\rm rot}$, I used both Sector 1 and Sector 2 (see Section 4.4). The lightcurve of the giant flare is given in Figure 4.1. From the lightcurve, I defined the starting time of the flare dataset at $t_{\rm start} = 1334.5$ and the ending time at $t_{\rm end} = 1336.5$.

### 4.2.2 Gaia RVS

Gaia RVS is a space-based medium resolution ($\Delta\lambda/\lambda \approx 10,500 - 12,500$ Å) near-infrared integral-field spectrograph aboard the Gaia space observatory. It has a wavelength range of 847 – 874 nm, mainly observing the Ca II infrared triplet. The first dataset for deriving the projected rotational velocity $v \sin i_*$ is consisted of five Gaia RVS spectra: one spectrum of TIC 206544316 and the spectra of the four reference stars. I accessed the mean sampled spectra table through `VizieR` as part of Gaia Data Release 3 (DR3) Part 1 [Gai22].

### 4.2.3 MIKE

The second dataset for deriving $V \sin i_*$ consisted of one MIKE spectrum and four CARMENES spectra. The spectrum for TIC 206544316 was observed with MIKE. The MIKE spectrograph is a high-resolution ($\Delta\lambda/\lambda \approx 35,000$ Å) optical echelle spectrograph on the Clay Telescope at the Magellan Observatory. The spectrograph

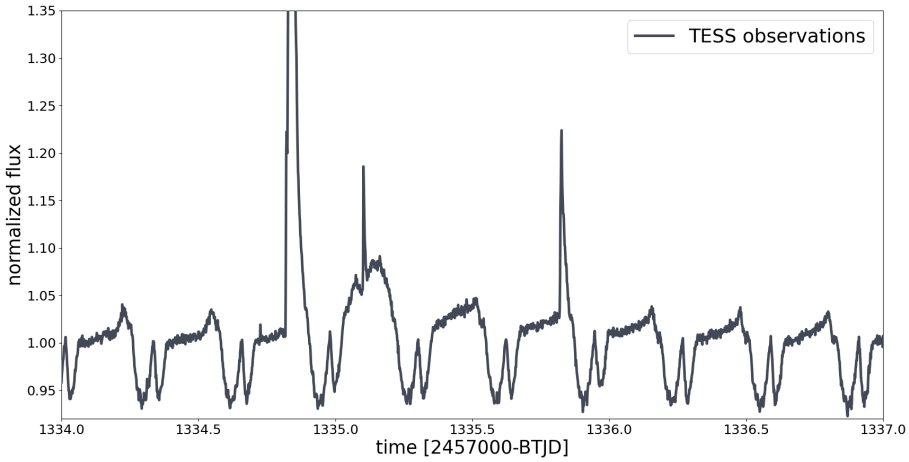


**Figure 4.1:** Lightcurve of TIC 206544316 from TESS. This section of the lightcurve displays the star's complex yet periodic modulation, characteristic of scallop-shell stars, along with a giant flare. The flare reaches a normalized flux 4× the quiescent flux but the plot is truncated to highlight other features.

covered a wavelength range of $\lambda = 3350 - 9000$ Å. The spectrum I used was part of an observational campaign in Kraus et al. [Kra+14] and the data were taken on July 16, 2012, with an exposure time of 160 seconds. I received the reduced, unnormalized spectrum.

To compare it with the reference spectra from CARMENES, the MIKE spectrum had to be normalized. Because I did not have access to the standard pipeline for normalizing MIKE spectra, which would provide a better continuum fit, I resorted to normalizing the spectrum using continuum fitting from `specutils`. The comparison between the fitted continuum from `specutils` and the unnormalized MIKE spectrum is shown in Figure 4.2 (a) for one of the échelle spectral orders. The normalized spectrum is shown in Figure 4.2. It can be seen that the normalization is not optimal, which caused some difficulties in Section 4.5.1. As a result, I carried out the derivation of $v \sin i_*$ from this dataset with this imperfectly normalized spectrum in mind.

### 4.2.4 CARMENES

In an ideal scenario, I would use MIKE spectra for the reference stars or a CARMENES spectrum for TIC 206544316. However, TIC 206544316 was not observed with CARMENES and spectra of the reference stars with MIKE were not publicly available. I obtained the spectra of the newest observations of the four reference stars from CARMENES Data Release 1 [DR1 Rib+23] which offered high-resolution ($\Delta\lambda/\lambda \approx 94,600$ Å) spectra of M dwarfs from the visual (VIS channel) to near-infrared (NIR channel). I used the VIS channel which covers a wavelength range of $\lambda = 5,200 - 9,600$ Å. The four reference stars were observed separately in 2020 (see Table 4.4) with 1800 seconds of exposure.

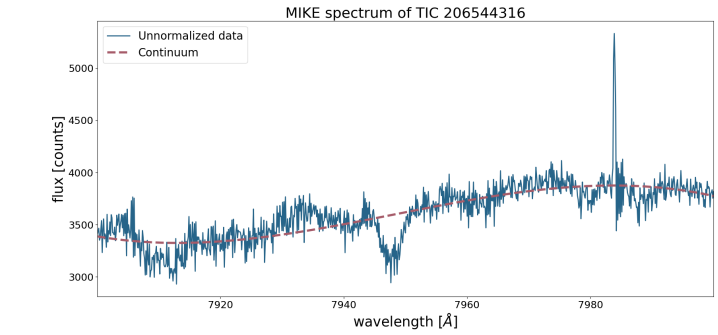


**(a)**

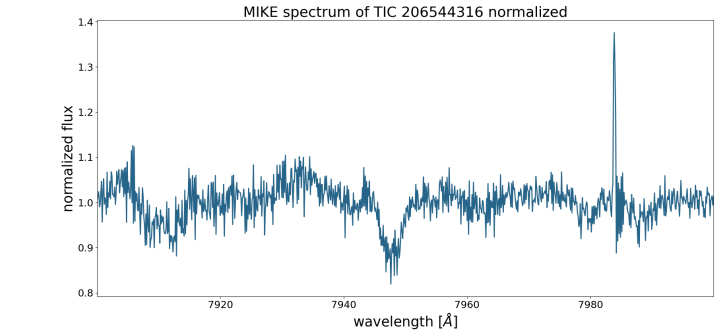


**(b)**

**Figure 4.2:** Spectra of TIC 206544316 from MIKE. Panel (a): unnormalized spectrum, panel (b): the normalized spectrum using `specutils`.

| KARMN ID | Observation dates |
|---|---|
| J05366+112 | December 25, 2020 |
| J08526+283 | March 11, 2020 |
| J10416+376 | February 6, 2020 |
| J11509+483 | December 29, 2020 |

**Table 4.4:** Observation dates of the four reference stars. From Ribas et al. [Rib+23].

## 4.3 Markov Chain Monte Carlo (MCMC)

In the quest to constrain the flare latitude $\theta_f$, the goal is not only to find the best-fit value of $\theta_f$ from the data, but more importantly, to determine the range of possible $\theta_f$ values along with their associated probabilities given the data $D$. In other words, **the end goal of this entire thesis is to obtain the probability distribution function (PDF) of $\theta_f$**. To achieve such task, I used Bayesian analysis. This means that, for each stellar or flare parameter required to constrain $\theta_f$, a single estimated value is not sufficient: I need their full PDF for a proper analysis.

### 4.3.1 Bayesian probabilistic inference

In a probabilistic inference, the posterior PDF $P(\theta|D)$, or the PDF for the parameter $\theta$ given data $D$, is given by the Bayes theorem as:

$$P(\theta|D) = \frac{\mathcal{L}(D|\theta)\,\pi_\theta(\theta)}{P(D)}, \tag{4.1}$$

where $\mathcal{L}(D|\theta)$ is the likelihood of parameter $\theta$ given data $D$, $\pi_\theta(\theta)$ is the prior PDF of the parameter, and $P(D)$ is the evidence, or the likelihood of the data $D$ unconditionally across all possible parameters. In the most simple scenario, $\theta$ refers to one parameter, which makes Equation 4.1 straightforward to compute. In other words, data $D$ is used to only constrain one parameter $\theta$. However, in real-world scenarios, especially in astrophysics [see HF18], $\theta$ is a set or collection of all possible parameters within data $D$. Simply put:

$$\theta = (\theta_1, \theta_2, \theta_3, ..., \theta_n) \tag{4.2}$$

where $n$ is the number of parameters, or it has $N$-dimension parameter space.

As mentioned above, $P(D)$ is the likelihood of data $D$ for across all parameters. Integrating it over the entire parameter space means that $P(D)$ can be written as:

$$P(D) = \int \mathcal{L}(D|\theta)\,\pi_\theta(\theta)\,d\theta. \tag{4.3}$$

Because $\theta$ is most likely a set of $n$ parameters, Equation 4.3 becomes a multi-variable integral. If all parameters are independent of each other, than the multi-variable integral can be solved one by one successively. However, such case is rare in real-life data. A large number of parameters and their dependencies, which has to be identified accurately, makes Equation 4.3 very difficult to calculate analytically and expensive to compute numerically. As a result, Equation 4.1 is often expressed as:

$$P(\theta|D) = \frac{1}{Z}\,\mathcal{L}(D|\theta)\,\pi_\theta(\theta), \tag{4.4}$$

with the evidence $P(D)$ is now represented as $Z$. When $P(D)$ cannot be reasonably computed, it can be seen from Equation 4.4 that $P(D)$ **can be ignored** because it is simply a normalization factor that is not dependent on any of the parameters, i.e., the integral of Equation 4.3 returns a value is the same for any individual points of $P(\theta|D)$. Therefore, Equation 4.1 is practically expressed as:

$$P(\theta|D) \propto \mathcal{L}(D|\theta)\,\pi_\theta(\theta), \tag{4.5}$$

which is the unnormalized or normalization-insensitive posterior PDF of parameters $\theta$, where the posterior is only dependent on the likelihood function and prior PDF.

### 4.3.2 MCMC in practice

After establishing how the posterior PDF can be derived, the next question is: **how can it be computed?** While it can sometimes be done analytically, the complex PDFs of the parameters and data might make such an approach impractical. Instead, the posterior PDF can be computed, or more accurately *sampled*, numerically using Markov Chain Monte Carlo (MCMC) methods. Markov Chain Monte Carlo consists of two probabilistic sampling methods: *Markov Chain* and *Monte Carlo*. The Monte Carlo method involves using random sampling to obtain numerical results, while the Markov Chain generates samples where the position or parameter of the next sample depends only on the previous sample. Together, they form MCMC, which essentially makes MCMC a random sampling method with a *biased random walk*.

The main advantage of MCMC is that it does not require a full analytic description of the properly normalized posterior PDF for the sampling to proceed. It only needs the ability to compute the ratio of the PDF at any pairs of points. This is feasible using the likelihood function $\mathcal{L}(D|\theta)$ and the prior PDF $\pi_\theta(\theta)$. In other words, MCMC does not return the *precise* probability value at any individual point. Instead, it returns the *relative* probability value of one point compared to another and computes Equation 4.5. This makes MCMC to be very good at sampling ill-normalized PDFs, which is valuable for computing Equation 4.4.

In general, MCMC works by generating a Markov chain through a random process (the Monte Carlo part) that produces a sequence of samples $x_1, x_2, ..., x_n$. By evaluating the likelihood function $\mathcal{L}(D|\theta)$ and prior PDF $\pi_\theta(\theta)$ at each step, and running the process long enough, the resulting set of samples $\{x_n\}_{n=1}^{N}$ should constitute a good representation of the posterior PDF $P(\theta|D)$. But, understandably, another question arises: **how is this guaranteed?** The answer lies in the algorithm to generate the Markov chain. Any MCMC algorithm must ensure that the equilibrium Markov chain from the set of samples $\{x_n\}_{n=1}^{N}$ does indeed represent the posterior PDF as efficient as possible. Section A.1 describes the simpler and commonly-used Metropolis-Hastings algorithm to give an idea of what does an MCMC do and why it works.

In this thesis, I used the Python-based `emcee` [For+13] to do my MCMC sampling. To compute the sampling, I calculated the Bayesian inferences in logarithmic for numerical efficiency and preventing underflow. For the algorithm, `emcee` uses the "stretch move" algorithm developed by Goodman and Weare [GW10] because it gives more efficient computation than the M-H algorithm (see Section A.2). To ensure that the resulting MCMC chain has converged and give a good representation of the posterior, I conducted the autocorrelation analysis (see Section A.3), as suggested by Hogg and Foreman-Mackey [HF18]. The autocorrelation time $\hat{\tau}$ measures how many steps needed to be taken for the chain to be completely independent of its starting point. When the chain has run for roughly $50\hat{\tau}$ (see Figure 4.3), I considered the chain has converged or it has run for more than 12 hours with visual inspection (see Figure C.3 for an example of a converged chain).

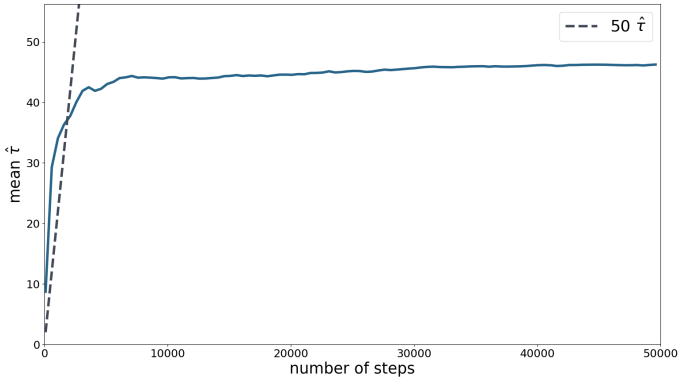


**Figure 4.3:** An example of an autocorrelation analysis from the MCMC procedure to obtain the PDF of $i_*$ for TIC 206544316 (see Section 4.5.2). The autocorrelation plot shows the value of $\hat{\tau}$ at each MCMC iteration (or step). The chain is considered to have converged when $\hat{\tau}$ reaches a plateau, meaning that $p(x)$ is the same for each iteration, which typically occurs when the number of iterations exceeds $50\hat{\tau}$. The dashed line marks the point corresponding to $50\hat{\tau}$ for each iteration. When the plot lies to the right of the dashed line, it indicates that the chain has converged.

## 4.4 Stellar rotation period $P_{\rm rot}$

One of the most used, if not *the* most used, method to derive periodicity in astrophysics is the Lomb-Scargle periodogram [Lom76; Sca82]. This section, based on the guideline of Lomb-Scargle periodogram by VanderPlas [Van18], outlines the theory behind the Lomb-Scargle periodogram and a practical solution to obtain the PDF of the rotation period $P_{\rm rot}$ for TIC 206544316, which is required for to derive the stellar inclination $i_*$.

### 4.4.1 Lomb-Scargle periodogram

At its heart, a periodogram is a Fourier transform. Section B.1 describes the classical periodogram and its relationship to the power spectrum. The classical periodogram assumes idealized conditions, where data are sampled uniformly. The Lomb-Scargle periodogram, on the other hand, allows for the determination of a periodogram that estimates the Fourier power spectrum from unevenly sampled data.

The derivation and assumption for the Lomb-Scargle periodogram is given in Section B.2. The Lomb-Scargle periodogram, which is essentially the generalized form of the classical periodogram, is given by:

$$P_{LS}(f) = \frac{1}{2}\left[\frac{\left(\sum_n g_n \cos\left(2\pi f[t_n-\tau]\right)\right)^2}{\sum_n \cos^2\left(2\pi f[t_n-\tau]\right)} + \frac{\left(\sum_n g_n \sin\left(2\pi f[t_n-\tau]\right)\right)^2}{\sum_n \sin^2\left(2\pi f[t_n-\tau]\right)}\right], \tag{4.6}$$

where $g_n$ is the true signal observed with discrete time, $f$ is the frequency, and

$t_n$ is the discrete time. The variable $\tau$ ensures insensitivity to global time shifts in the data:

$$\tau = \frac{1}{4\pi f} \tan^{-1}\left(\frac{\sum_n \sin 4\pi f t_n}{\sum_n \cos 4\pi f t_n}\right). \tag{4.7}$$

There are two important things to note for the Lomb-Scargle periodogram given in the equation above.

**First, the Lomb-Scargle periodogram works best if the underlying signal $g_n$ can be modeled with one, or more, sinusoidal waves.** This is because the Fourier transform of the signal, assumes that the signal, even if it is complex, can be represented as a sum of simple sinusoidal components from the contribution of the Euler equation $e^{-2\pi f t}$.

**Second, the periodogram is identical to a periodogram made from the $\chi^2$ goodness of fit of a simple sinusoidal wave.** This is noted down by VanderPlas [Van18] as one of the most important aspect of the Lomb-Scargle periodogram. A periodogram made this way is called the Least-squares periodogram, which was studied in depth by Lomb [Lom76] for astronomical data.

The lightcurve of TIC 206544316, as other scallop-shell stars, has distinct complex patterns that departs from "simple" sinusoidal waves typical of star spots modulation. While this might be against the first point of the previous paragraph, the major components of the TIC 206544316's lightcurve pattern can still be modeled by at least one sinusoidal wave in the first order. It is also still a reasonable approximation because, from the favored hypothesis in the literature, their sharp peaks and dips are *in addition* to a more dominant modulation from star spots, which can be modeled by superpositions of sine waves. I used the Lomb-Scargle periodogram as a first-order approximation of the stellar rotation period $P_{\rm rot}$. I used the periodogram class from `lightkurve` directly with choosing Lomb-Scargle as the method. I combined the lightcurves of TIC 206544316 from Sector 1 and Sector 2 of TESS before passing the lightcurves to the periodogram. The periodogram returned $P_{LS}$ (see Section 5.1).

However, $P_{LS}$ from the Lomb-Scargle periodogram does not come with uncertainties that are suitable for Bayesian analysis. It is nonphysical to derive the uncertainties of the period *purely* from the periodogram, because it is still the estimator of the power spectrum. The close connection of the Lomb-Scargle periodogram with the Least-squares periodogram drives this point home: **the periodogram is the measurement of how good the model fits the data from metrics such as $\chi^2$ analysis. It can not provide the PDF and uncertainties of each contributing parameters in the model.**

### 4.4.2 Uncertainties with MCMC

It is clear that, while the Lomb-Scargle periodogram can return a first-order period estimate, an additional step must be taken to obtain the PDF of the period $P_{\rm rot}$. I decided to calculate the uncertainty using MCMC. By assuming that the uncertainties in the lightcurve are Gaussian and independent, I combined results of all possible $P_{\rm rot}$ from a periodic model to derive the posterior with using `emcee`.

#### Cosine function

For a trial run, I used a cosine function with a linear slope to model the periodic sine signal given as:

$$y_{\rm model}(t) = A\cos\left(\frac{2\pi}{P}t + \omega\right) + mt + b, \tag{4.8}$$

with $A$, $P$, and $\omega$ representing the amplitude, period, and phase of the cosine wave, respectively, and $m$ and $b$ as the gradient of the linear trend and the offset. The likelihood function of the dataset with Gaussian uncertainties ($\sigma_n$) and the full set of parameters, $\Theta = [A, P, \omega, m, b]$, is written as:

$$\log \mathcal{L}(y|\Theta) = -\frac{1}{2}\sum_{n=1}^{N}\left[\frac{(y_n - y_{\rm model}(t_n;\Theta))^2}{\sigma_n^2} + \log \sigma_n^2\right], \tag{4.9}$$

where $\sigma_n$ represent the uncertainties of the fluxes from the lightcurve. The prior for the MCMC sampling are given in Table 4.5. I determined the initial values by estimating the maximum likelihood using `scipy`'s optimize module. For the period $P$, the initial value was $P_{LS}$.

| Parameter | Prior |
|---|---|
| $A$ | $\mathcal{U}(-0.1, 0.1)$ |
| $P$ (days) | $\mathcal{U}(P_{\rm LS} - 0.1, P_{\rm LS} + 0.1)$ |
| $\omega$ | $\mathcal{U}(-\pi, \pi)$ |
| $m$ | $\mathcal{U}(-100, 100)$ |
| $b$ | $\mathcal{U}(-100, 100)$ |

**Table 4.5:** Parameters of the cosine function and the prior PDF for the MCMC.

Before passing the lightcurve of Sector 1 and Sector 2 to the MCMC sampling, I smoothed the lightcurve to remove any flares and outliers. I calculated the rolling median and standard deviation of the flux for each data point within eight neighboring points, i.e., the median is calculated from four points before and after the that specific data point. If the flux value of this data point is higher than $1\sigma$ of the rolling median, I removed that data point. This method also removed the first

and last four data of my array, but this is a negligible number compared to the ≈ 30,000 data points that I have. I found that using a conservative value of $1\sigma$ offered a balance between removing the bigger flares automatically and allowing noise to exist in the data.

I then ran an MCMC simulation using 15 walkers and 10,000 iterations. The MCMC fit is given in Figure 5.2 corner plot given in Figure C.2. As expected, the cosine model barely represents the data at all. It did not converge properly, with a number of walkers straying from the more crowded distribution. This is clearly shown in Figure 5.2, where two solutions are presented. Since both perform equally poorly in representing the data, it is difficult to determine which one is "wrong". I ran this simulation multiple times and found the MCMC sampling with the cosine model to be very sensitive to changes in the initial values. The walkers easily got stuck in low-probability regions when the changes exceeded 0.01, as the model could not represent the data well. To obtain more accurate results, a better model is needed.

### Modulation template

To simplify the model and computation, I decided to use the folded lightcurve from Sector 1 and Sector 2 as a template instead of finding an analytical function that represent my dataset. This is because, even though are observations outside of these two sectors, the the nearest observations of TIC 206544316 from Sector 2 are Sector 28. Sector 28 was observed in July 2020, around two years after Sector 1 and Sector 2. The modulation pattern of scallop-shell stars change after one or two years (See Section 3.1 and Figure 3.6). Hence, I chose to only use Sector 2 additionally to Sector 1 because Sector 2 was observed subsequently to Sector 1 with similar modulation pattern.

To create the modulation template, I folded the smoothed lightcurves from Sector 1 and 2 from Section 4.4.2. To improve computational efficiency, I thinned the dataset by selecting every third data point, reducing the total number of data points to around 10,000. I folded the smoothed lightcurve using the period given by the Lomb-Scargle periodogram, with $P = P_{LS}$ and an arbitrarily chosen epoch $T_{\text{epoch}}$. The equation is given by:

$$\phi = \frac{t - T_{\text{epoch}}}{P} \mod 1. \tag{4.10}$$

The result is given in Figure 4.4 (a). It can be seen that, even though the bigger flares were removed, there were still smaller flares contaminating the modulation data. I binned the folded lightcurve to 300 bins and smoothed the folded lightcurve again using rolling median. I then removed data points above $1\sigma$. The final modulation template is shown in Figure 4.4 (b).

Let the modulation template $M$ be represented as a set of points:

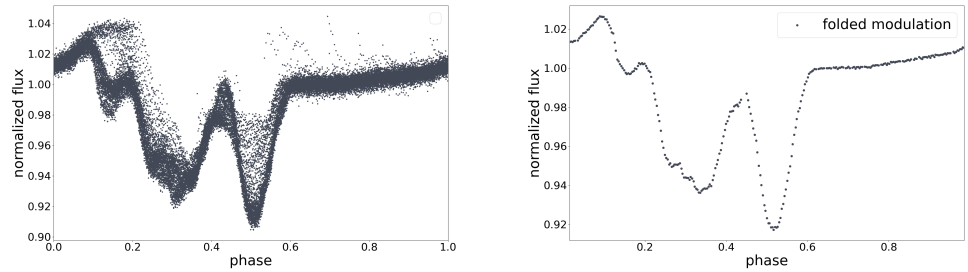


**(a)** **(b)**

**Figure 4.4:** Modulation model from the folded lightcurve. Panel (a): The smoothed (using rolling median) lightcurve from Sector 1 and Sector 2, folded using `lightkurve` with $P_{\text{LS}}$. Panel (b): The folded lightcurve from (a), further smoothed using a rolling median, with $1\sigma$ outliers removed, and then binned. The lightcurve in panel (b) is the modulation template used in the MCMC simulation.

$$M = \{(\phi_n, F_n) \mid n = 1, 2, ..., N\}, \tag{4.11}$$

where $\phi_n$ are the phases from the folded lightcurve and $F_n$ are their corresponding smoothed and binned fluxes. I then interpolated the modulation template $M$ using the linear interpolation module from `numpy` to create the modulation function. The interpolated modulation function is expressed as $y = I_M(\phi)$.

To allow some degree of freedom, I introduced a vertical stretch and a horizontal offset to the modulation template that is independent of the epoch. To apply the vertical stretch, I calculated $\bar{y}$, the average value of the modulation template, and defined a stretch factor $S$. The horizontal offset is denoted by $O$. Therefore, for each data point $t$ in the dataset, the full model function $y_{\text{model}}$ can be written as:

$$y_{\text{model}}(t) = \bar{y} + (S \times [I_M(\phi) - \bar{y}]) + O. \tag{4.12}$$

The intuition behind the stretch factor is that when $S = 1$, Equation 4.12 simplifies to the interpolated modulation function with only the offset $O$ applied. However, when the model is stretched by a factor of $S$, each data point is scaled relative to the average value $\bar{y}$, effectively placing it at a distance of $S$ from $\bar{y}$. For example, if $S = 2$, then a data point at time $t$ that was previously located a distance $y$ from $\bar{y}$ is now located at a distance of $2y$ from $\bar{y}$.

In its more complete form, the model function is expressed as:

$$y_{\text{model}}(t) = \bar{y} + \left(S \times \left[I_M\left(\frac{t - T_{\text{epoch}}}{P} \mod 1\right) - \bar{y}\right]\right) + O. \tag{4.13}$$

The likelihood function for this model is also represented with Equation 4.9. The difference is that the modulation model only depends on four parameters $\Theta = [P, T_{\text{epoch}}, S, O]$. The priors are given in Table 4.6.

| Parameter | Prior |
|---|---|
| $P$ (days) | $\mathcal{U}(-0.1, 0.5)$ |
| $T_{\text{epoch}}$ | $\mathcal{U}(1000, 2000)$ |
| $S$ | $\mathcal{U}(0, 5)$ |
| $O$ | $\mathcal{U}(-100, 100)$ |

**Table 4.6:** Parameters of the modulation model and the prior PDF for the MCMC with the modulation template.

For the initial value of $T_{\text{epoch}}$ I used $T_{\text{epoch}} = \min(T) + 0.2$. For the period, I used $P_{LS}$ from the Lomb-Scargle periodogram, while the stretch factor $S$ to be 1 and the offset $O$ to be 0. I passed the entire lightcurve of Sector 1 and Sector to this MCMC sampling with 15 walkers and 30,000 iterations. The computation was considerably longer than the previous model because it did interpolation at every time step, even though it has less parameters and iterations. The corner plots are given in Figure C.4 and the final period from this method (see Section 4.4), with its uncertainties, is assigned as $P_{\text{rot}}$.

## 4.5 Stellar inclination $i_*$

Deriving the stellar inclination $i_*$ requires three observable measurements: the stellar rotation period $P_{\text{rot}}$, stellar radius $R_*$, and the projected rotational velocity $v \sin i_*$. This is because the observed component of the equatorial velocity $v_{\text{eq}}$ depends on the stellar inclination $i_*$. An illustration of this can be seen in Figure 4.5. From the relationship between the projected rotational velocity $v \sin i_*$ and the true equatorial rotational velocity $v_{\text{eq}}$, the stellar inclination $i_*$ can be calculated as:

$$i = \sin^{-1}\left(\frac{v \sin i_*}{v_{\text{eq}}}\right) = \sin^{-1}\left(\frac{v \sin i_*}{2\pi R/P_{\text{rot}}}\right). \tag{4.14}$$

The stellar rotation period $P_{\text{rot}}$ is determined in Section 4.4, with results given in Section 5.1. The stellar radius $R_*$, on the other hand, is adopted from Günther et al. [Gün+22] (see Section 4.1). This section describes the methods of determining the $v \sin i_*$ from spectroscopic observations and the statistical framework of inferring $i_*$ from the available parameters. The end-goal is to generate the PDF of $i_*$, which serves as the informed prior PDF to obtain the posterior PDF of the flare latitude $\theta_f$ using an MCMC sampling.

### 4.5.1 Projected rotational velocity $v \sin i_*$

To infer the $v \sin i_*$ of TIC 206544316, I used the cross-correlation method [RJG12]. Cross-correlation is a measure of similarity of two series as a function of the displacement from one to the other. In this context, the method works as follow:

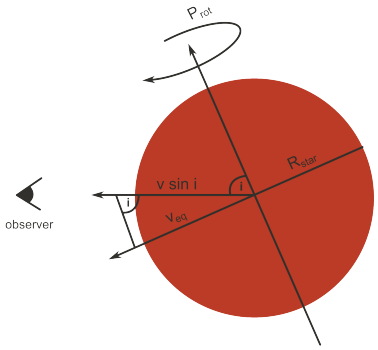


**Figure 4.5:** Illustration of the projected rotational velocity $v \sin i_*$ depends on the inclination of the star's rotational axis to our line of sight as observers.

a spectrum from a slowly rotating star is cross-correlated with the same spectrum that is *artificially broadened to different rotational velocities* (see Figure 4.6 and 4.7). Each cross-correlation then gives different cross-correlation function (CCF) corresponding to a different projected rotational velocity $v \sin i_*$. Each CCF has its own full width at half maximum (FWHM). The FWHM, or the width of the CCF, therefore provides a calibrated measure of the value of $v \sin i_*$. An example of how the FWHM changes depending on the $v \sin i_*$ can be seen in Figure 4.8.

After obtaining the FWHM of CCFs corresponding to different velocities, I can then fit the calibration function with a third-degree polynomial $f$, where:

$$\begin{aligned} f(\mathrm{FWHM}) &= v \sin i_* \\ \sum_{k=0}^{3} a_k \, \mathrm{FWHM}^k &= v \sin i_* \end{aligned} \tag{4.15}$$

and $a_k$ as the polynomial coefficients. The spectrum of the target star is then cross-correlation with the original reference spectrum. The FWHM of the resulting CCF is converted into $v \sin i_*$ according to calibration function in Equation 4.15.

The challenges in obtaining $v \sin i$ from M dwarfs are numerous. Choosing a spectral region to compare or model must be done carefully. M dwarfs are magnetically active (Section 2.1), thus individual magnetically sensitive lines are prone to magnetic broadening or other activity-related effects [see e.g., Laf+23; Pas+19]. They also have dense molecular lines, which makes spectral lines susceptible to blending. Additionally, M dwarfs emit most of their radiation in the near-infrared (NIR), which can be affected by telluric contamination if observed from ground-based telescopes.

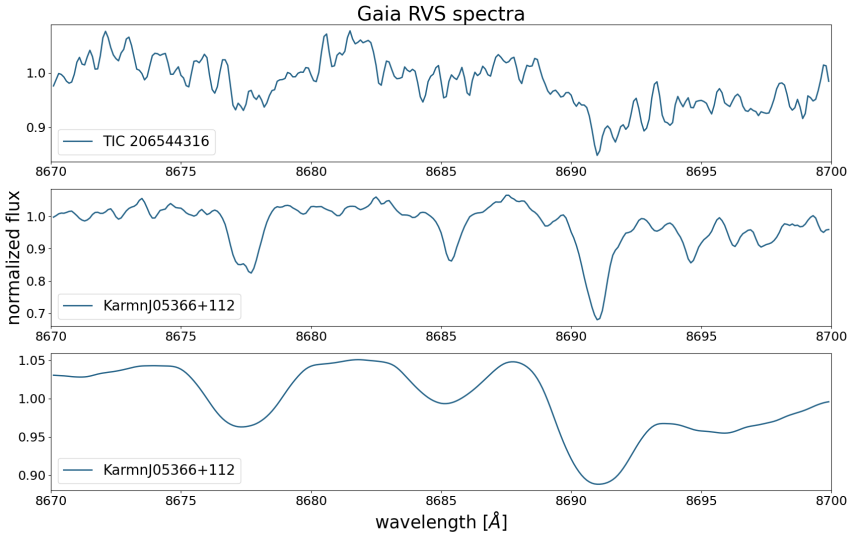


**Figure 4.6:** The spectra region from Gaia RVS that were used in the cross-correlation method. Top: the spectrum of TIC 206544316. Middle: spectrum of KarmnJ05366+112, one of the reference stars. Bottom: the reference star's spectrum artificially broadened to ~ 70 km/s. Note that while the top and middle spectra look completely different, the artificially broadened spectrum shows some resemblance with the top spectrum. This qualitatively confirms that TIC 206544316 has high $v \sin i_*$.

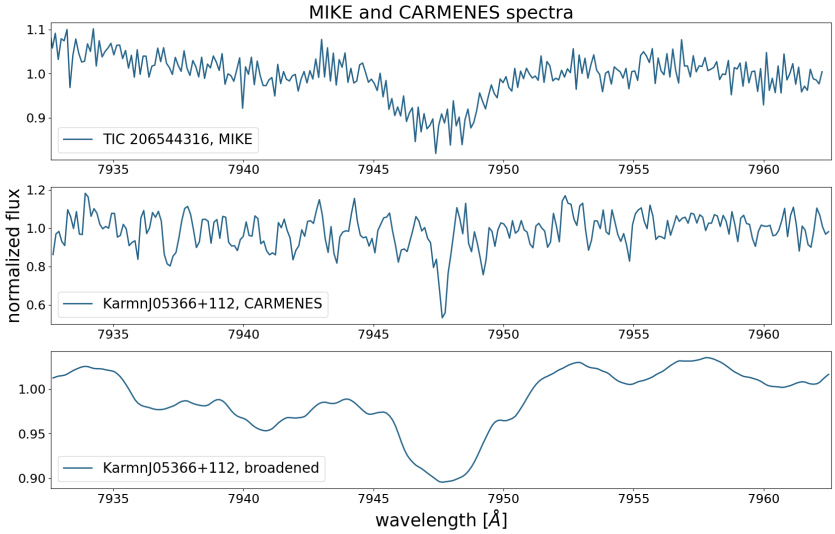


**Figure 4.7:** The spectra region from MIKE and CARMENES that were used in the cross-correlation method. Top: the spectrum of TIC 206544316 from MIKE. Middle: spectrum of KarmnJ05366+112 from CARMENES. Bottom: the reference star's spectrum artificially broadened to ~ 70 km/s.

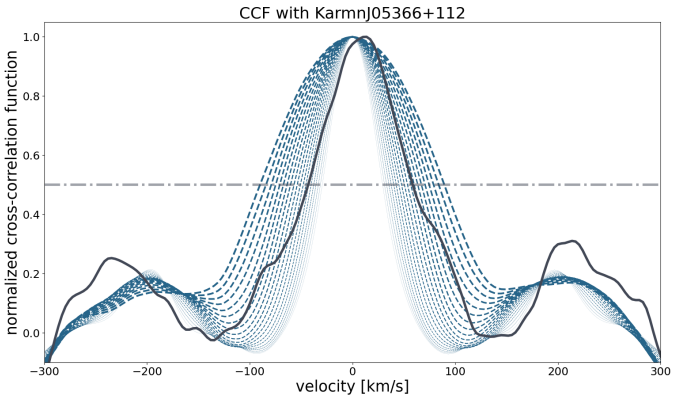


**Figure 4.8:** Cross-correlation profile of the reference star KarmnJ05366+112 with a series of artificially broadened spectra. Blue dashed lines show the normalized cross-correlation functions of each artificially-broadened spectrum with the non-broadened reference spectrum. Darker lines correspond to higher $v \sin i_*$. The grey dash-dotted line corresponds to the FWHM of the CCF. The width of each of the CCFs at the dash-dotted line is the FHWM used in the calibration function. The red line is the CCF rom the object spectrum with the reference spectrum. It can be seen that the peak of the CCF function is shifted, indicating a shift in the line absorption. However, I believe this is not due to a Doppler shift, but rather because it is difficult to precisely determine the center of the line absorption in Figure 4.6.

All of aforementioned factors can introduce uncertainties due to mismatches between the target spectrum and the reference spectra, especially when $v \sin i_*$ is determined by directly comparing individual spectral lines to artificially broadened spectra. In contrast, the cross-correlation method mitigates problems with individual lines and allows boosting the signal by compressing the information from many lines into a single value: the **FWHM** of the CCF. The final $v \sin i_*$ can also be obtained as an average from different spectral regions and multiple reference stars.

TIC 206544316 was observed using two different instruments (Section 4.2), Gaia RVS and MIKE. For each observation, I have four reference stars to cross-correlate. The Gaia RVS spectrum is correlated with four Gaia RVS spectra (hereafter the Gaia RVS dataset). The MIKE spectrum is correlated with four CARMENES spectra (herafter the MIKE-CARMENES dataset). Each dataset returned four $v \sin i_*$ values, corresponding to CCFs (see Section D) from the cross-correlation between four reference stars and the target star, which then were averaged to give each dataset one $v \sin i_*$ value.

The Gaia RVS dataset was observed using the same instrument and were processed with the same pipeline, which minimizes instrumental uncertainties. The MIKE-CARMENES dataset, on the other hand, was not. MIKE and CARMENES have two very different spectral resolution, $R \approx 35,000$ and $R \approx 96,000$, respectively. To address this, the CARMENES spectra, with higher spectral resolutions, were binned to match the spectral resolution of MIKE. Therefore, the MIKE-CARMENES dataset is more prone to additional systematic uncertainties from using two differ-

ent instruments.

In the beginning of the data analysis, I tried to choose spectral regions, each covering approximately 20 Å, centering around or including several magnetically-insensitive lines that does not have any telluric contamination or emission lines, a practice that was also done by Reiners et al. [RJG12]. I based my selection on the table of line-by-line sensitivity to stellar activity in M dwarfs by Lafarga et al. [Laf+23]. However, the properties of the Gaia RVS spectra and the circumstances of how I got the MIKE spectrum led to several difficulties fulfilling this above mentioned requirement. There are two reasons for this difficulty.

First, spectra from Gaia RVS has a wavelength range of only 270 Å and they are dominated with the Ca II infrared triplet, which is the primary target of Gaia RVS. On the other hand, Ca II triplet show correlations with Ca II & H K line as chromospheric activity indicators [e.g., Bus+07]. Second, the MIKE spectrum was not properly normalized because of my lack of access to the MIKE reduction pipeline (see Section 4.2.3). Cross-correlation is fundamentally a measure of similarity and I require structure in the spectrum to be compared to the reference spectra. Thus, using spectral regions with ambiguous normalization, as opposed to the properly normalized and processed CARMENES spectra, would not yield optimal results. Both situations considerably limited the spectral regions to be analyzed.

On the other hand, while using magnetically-insensitive lines would prove to be ideal, the contribution from magnetic activity on these lines are not significant due to the high equatorial velocity $v_{\mathrm{eq}}$ of the target star. Any broadening and blending would be due to the rotational velocity and this makes avoiding magnetically-sensitive lines unnecessary. With that being said, for Gaia RVS spectra, avoiding the Ca II triplet would still be preferable. For the MIKE spectrum, finding spectral region where the target spectra closely resemble the artificially-broadened CARMENES spectra, i.e., a flat continuum with clear absorption lines, is ideal to help reduce unnecessary uncertainties.

As a result, the final selection of spectral regions is based on two criteria: 1) the region does not contain emission lines or known magnetically active lines, such as the Ca II triplet; and 2) the target spectra resemble the artificially broadened reference spectra as closely as possible. The second criterion is more likely to be satisfied if the selected regions contain strong absorption lines. Due to normalization problems, isolated lines work best for the MIKE spectrum (see Figure 4.7), since blended lines can appear as "flat" features that resemble the continuum but are actually not part of it. Additionally, I need some *structure* in the spectrum to cross-correlate it with another structure.

Finally, the CCFs of both datasets were calculated from a single spectral region each and covering different wavelength ranges. For the Gaia RVS dataset, the spectral region spans 8670 – 8673 Å, covering around 13 Å, that includes the Fe II lines 8677 and 8691 Å and the Ti I lines 8678 and 8685 Å. Meanwhile, the MIKE-

CARMENES dataset covers the spectral region 7932.5 – 7962.5 Å with a width of around 30, Å, centering around the Rb line 7947.5 Å.

### 4.5.2 Bayesian inference of stellar inclination $i_*$

As shown in Equation 4.14, calculating the stellar inclination $i$ is straightforward when all the required observables are available. However, problems come when the PDF of $i$ is of interest, as it is necessary for deriving the PDF of $\theta_f$. Taking a closer look at the relationship between the parameter, it could be seen that $v \sin i_*$ is not statistically independent of the equatorial rotational velocity $v_{\rm eq}$. This is because $v \sin i_*$ is the *projected* observable component of $v_{\rm eq}$ and always follows the relationship:

$$v \sin i_* \leq v_{\rm eq}. \tag{4.16}$$

Since there are parameters that are not statistically independent, the propagation of uncertainties can no longer assume Gaussian distributions. To address this, Masuda and Winn [MW20] provided the Bayesian analysis to infer stellar inclination $i_*$ that takes into account the statistical dependency of $v \sin i_*$ and $v_{\rm eq}$.

#### Assumptions and general premise

Consider that deriving $i_*$ requires two datasets, $d_v$ and $d_u$. Here $d_v$ is the dataset to derive $v_{eq}$ and $d_u$ to derive $v \sin i_*$. For consistency purposes, $v \sin i_*$ is now referred to as $u$ and $v_{\rm eq}$ as $v$. The dataset $d_v$ to constrain $v$ usually comes from multiple datasets, such as photometric time series to determine the stellar period $P_{\rm rot}$ and spectroscopic observations to derive the stellar radius $R$. Likewise, the dataset $d_u$ to constrain $u$ comes from observations. This is usually a mid- to high-resolution spectrum that shows the effects of the Doppler-rotational broadening on the star's spectral lines (see Section 4.5.1). Therefore, the likelihood functions for $v$ and $u$ can be computed as:

$$\mathcal{L}_v(v) \equiv P(d_v|v) \tag{4.17}$$
$$\mathcal{L}_u(u) \equiv P(d_u|u). \tag{4.18}$$

Masuda and Winn [MW20] assumed two things:

First, while $v$ and $u$ are statistically dependent, the datasets $d_v$ and $d_u$ to constrain them are independent. This means that, if the totality of data $D$ is described as:

$$D = \{d_v, d_u\}, \tag{4.19}$$

the combined likelihood of $D$ is separable:

$$\mathcal{L}(D) = P(D|v,u) = P(d_v|v,u)\, P(d_u|v,u) \tag{4.20}$$
$$= P(d_v|v)\, P(d_u|u) \tag{4.21}$$

$$= \mathcal{L}_v(v)\mathcal{L}_u(u). \tag{4.22}$$

Here $d_v$ and $d_u$ are independent of each other, and the values of $v$ and $u$ do not influence $d_u$ and $d_v$, respectively. As a result, $P(d_v|v,u)$ can be expressed as $P(d_v|v)$, the probability of $d_v$ given $v$, and vice versa.

Second, the quantities $v$ and the stellar inclination $i_*$ are independent and their prior PDF for these parameters is separable:

$$\pi_{v,i}(v,i) = \pi_v(v)\,\pi_u(u) \tag{4.23}$$

and consequently means:

$$P(v|i) = \pi_v(v) \tag{4.24}$$
$$P(i|v) = \pi_i(i), \tag{4.25}$$

where $\pi(v)$ is the prior distribution of $v$ and $\pi(u)$ of $u$.

However, note that the second assumption is not trivial. In certain cases, there might be an actual correlation between $v$ and $i_*$. For example, a sample of stars with measured rotation periods may be biased against low-inclination systems. This is because the photometric variability associated with rotation leans toward zero as the star approaches a pole-on rotation, where the observer would see only one hemisphere, and no modulation by rotation can be observed. As a result, systems with low $v$, or slow rotators with weak rotational variability, might preferentially have high inclinations because the signal-to-noise ratio to detect the rotation of these systems is higher for edge-on systems. Nevertheless, the effect is neglected for this Bayesian framework.

In contrast, the dependency of $v$ and $u$ results in the two parameters becoming prior dependent. This means that their prior PDF are not separable:

$$\pi_{u,v}(u,v) \neq \pi_v(v)\,\pi_u(u) \tag{4.26}$$

and:

$$P(u|v) \neq \pi_u(u). \tag{4.27}$$

Masuda and Winn [MW20] noted that **ignoring this dependency is the main source of errors in previous literature.**

### Marginal posterior of cos $i_*$

This section describes the mathematical procedure of the Bayesian inference and the numerical application from [MW20]. Note that this section uses cos $i_*$ instead of $i_*$ because the PDF is flat in cos $i_*$ for an isotropic orientation, i.e., a uniformly random stellar spin axis. A full justification is given in Section E.

To calculate the posterior PDF of $\cos i_*$ given data $D$, Bayes' theorem states:

$$P(\cos i_*|D) = \frac{\mathcal{L}(D|\cos i_*)\,\pi_{\cos i_*}(\cos i_*)}{P(D)}, \tag{4.28}$$

where $P(D)$ is the unconditional marginal distribution of the entire data $D$. As mentioned in Section 4.3, $P(D)$ is usually difficult to compute and is often ignored in both numerical and analytical analyses. Therefore, the posterior PDF can instead be written as:

$$P(\cos i_*|D) \propto \mathcal{L}(D|\cos i_*)\,\pi_{\cos i_*}(\cos i_*), \tag{4.29}$$

which is the unnormalized posterior PDF, depending only on the likelihood function and the prior PDF.

Although Equation 4.29 looks straightforward, the challenge lies in computing $\mathcal{L}(D|\cos i_*)$, the likelihood of data $D$ for any given $\cos i_*$. The likelihood of data $D$ in Equation 4.20 is given for all parameters or, more precisely, as a collection of parameters $\theta$ rather than individual ones. In fact, from $\mathcal{L}(D)$, the posterior PDF of the parameters can only be expressed as:

$$P(\theta|D) \propto \mathcal{L}(D|\theta)\,\pi_\theta(\theta), \tag{4.30}$$

with $\theta$ consisting all parameters that could be derived from data $D$, i.e., $u$, $v$, and $\cos i_*$. However, Equation 4.30 is usually not informative because the posterior PDF of individual parameters is often of interest. In this case, it is the posterior PDF of $\cos i_*$. To separate the posterior PDF of one parameter, Equation 4.30 must be integrated over the other "nuisance" parameters. Therefore, Equation 4.29 represents the *marginal* posterior of $\cos i_*$ derived from Equation 4.30. Computing the marginal posterior of $\cos i_*$ requires the marginal likelihood of $\mathcal{L}(D|\cos i_*)$, which is obtained by integrating Equation 4.20 over the remaining parameters.

To compute the marginal likelihood of $\cos i_*$, note that $u$ and $v$ can be written as functions of $\cos i_*$ and the other parameter respectively:

$$u(\cos i_*, v) = v\sqrt{1-\cos^2 i}, \text{ or} \tag{4.31}$$

$$v(\cos i_*, u) = \frac{u}{\sqrt{1-\cos^2 i}}. \tag{4.32}$$

This means that marginalizing $\cos i_*$ can be done by transforming $u$ and $v$ as functions shown in Equation 4.31 and 4.32, respectively, and integrating over the other parameter. Here I demonstrate marginalizing the likelihood of $\cos i_*$ over $v$ with transforming $u$ to $u(\cos i_*, v)$.

From Bayes' theorem, the marginal likelihood of $\cos i_*$ over the parameter $v$ can be written as:

$$\mathcal{L}(D|\cos i_*) = \int \mathcal{L}(D|u,v)\,P(v|\cos i_*)\,dv. \tag{4.33}$$

From Equation 4.24, $P(v|\cos i_*)$ is simply the prior PDF of $v$ because $i_*$ and $v$ are independent. Note that this is not valid when the marginal likelihood is integrated over the parameter $u$, since $u$ and $i_*$ are not independent. Substituting $\mathcal{L}(D|u,v)$ with Equation 4.22 gives:

$$\mathcal{L}(D|\cos i_*) = \int \mathcal{L}_u(u)\,\mathcal{L}_v(v)\,\pi_v(v)\,dv. \tag{4.34}$$

Transforming $u$ as functions of $v$ and $\cos i_*$ using Equation 4.31 then gives:

$$\mathcal{L}(D|\cos i_*) = \int \mathcal{L}_u(v\sqrt{1-\cos^2 i})\,\mathcal{L}_v(v)\,\pi_v(v)\,dv. \tag{4.35}$$

Note that transforming $u$ as a function of $v$ also takes into account the dependency between $u$ and $v$, since the likelihood $\mathcal{L}_u(u)$ must be integrated over $v$ as well. If $u$ and $v$ were independent, $\mathcal{L}_u(u)$ would be outside the integral. Lastly, from computing the marginal likelihood of $\cos i_*$, Equation 4.29 can now be written as:

$$P(\cos i_*|D) \propto \pi_{\cos i_*}(\cos i_*) \int \mathcal{L}_u(v\sqrt{1-\cos^2 i})\,\mathcal{L}_v(v)\,\pi_v(v)\,dv, \tag{4.36}$$

where $\pi_{\cos i_*}(\cos i_*)$ is defined in Equation E.1 and proven in Section ??. The prior PDF $\pi_{\cos i_*}(\cos i_*)$ is a constant for all possible $\cos i_*$. Therefore:

$$P(\cos i_*|D) \propto \int \mathcal{L}_u(v\sqrt{1-\cos^2 i})\,\mathcal{L}_v(v)\,\pi_v(v)\,dv, \tag{4.37}$$

is the final form of Equation 4.36, representing the marginal posterior PDF of $\cos i_*$ following the Bayesian inference procedure of Masuda and Winn [MW20] that takes into account dependent parameters.

### Numerical computation for the PDF of $\cos i_*$

Recall that the goal of this section is to obtain the PDF of $i_*$, which can also be expressed as $\cos i_*$, to serve as the informed prior PDF for MCMC sampling. While the analytical procedure outlined above gives a solution, computing the integral can be difficult when the likelihood functions and the prior PDFs are complex. This is often the case in real-world data, where not everything can be accurately represented by a straightforward PDF, such as a Gaussian distribution. To overcome this limitation, I used MCMC sampling to generate the posterior PDF of $\cos i_*$ from known observed values of the stellar period $P_{\rm rot}$, stellar radius $R_*$, and projected rotational velocity $v \sin i_*$, each characterized by their respective PDFs.

However, any posterior PDF that my MCMC sampling generates must match the analytical solution given in Equation 4.37. This guarantees that the obtained PDF follows the framework given by Masuda and Winn [MW20] and addresses the dependency of the $v_{\rm eq}$ and $v \sin i_*$. Masuda and Winn [MW20] did provide illustrative cases where the posterior PDFs of $\cos i_*$ were computed analytically and numerically with MCMC. The illustrative cases were given for a star with

$v_{\mathrm{eq}} = 10 \pm 2$ km/s and different values of $v \sin i_*$, including $9.8 \pm 2$ km/s and $4.0 \pm 2$ km/s. Unfortunately, the generated PDF and assumptions of $P_{\mathrm{rot}}$ and $R_*$ of each of the cases were not published. Any testings of independent results with the results of Masuda and Winn [MW20] could only be done by visually comparing the plot of the PDF and the analytical solution. Meaning: the integral of Equation 4.37 must be solved.

Fortunately, Bowler et al. [Bow+23] provided the closed-form of Equation 4.37, which is written as:

$$P(\cos i_* | D) \propto \frac{e^{-\frac{\left(v \sin i_* - \frac{2\pi R_*}{P_{\mathrm{rot}}} \sqrt{1-\cos^2 i}\right)^2}{2\left(\sigma^2_{v \sin i_*} + \sigma^2_{v_{\mathrm{eq}}}(1-\cos^2 i)\right)}}}{\sqrt{\sigma^2_{v \sin i_*} + \sigma^2_{v_{\mathrm{eq}}}(1 - \cos^2 i)}}, \tag{4.38}$$

where $\sigma_{v \sin i_*}$ and $\sigma_{v_{\mathrm{eq}}}$ are the uncertainties of $v \sin i_*$ and $v_{\mathrm{eq}}$, respectively, from observational measurements. While Equation 4.38 provides a way to test and compare my MCMC sampling result, the solution does not come without a caveat. The main problem of the closed-form solution is that it assumes that $v \sin i_*$, $P_{\mathrm{rot}}$, $R_*$, and especially $v_{\mathrm{eq}}$, can be represented by Gaussian distributions. This is, of course, because solving Equation 4.37 analytically is easier with computable and often realistic distributions.

The assumption that the observed measurements follow a Gaussian distribution is usually true for $v \sin i_*$, because $v \sin i_*$ are directly measured from the line broadening. In other words, $v \sin i_* \sim \mathcal{N}(v \sin i_*, \sigma^2_{v \sin i_*})$. However, this might not be true for $v_{\mathrm{eq}}$. In fact, the distribution of $v_{\mathrm{eq}}$ is not analytically straightforward in most cases. The equatorial velocity is derived from two observables: $P_{\mathrm{rot}}$ and $R$. Each of them may be represented by a Gaussian distribution, such that $P_{\mathrm{rot}} \sim \mathcal{N}(P_{\mathrm{rot}}, \sigma^2_{P_{\mathrm{rot}}})$ and $R_* \sim \mathcal{N}(R_*, \sigma^2_{R_*})$ from observational measurements. In contrast, the distribution of $v_{\mathrm{eq}}$ from:

$$v_{\mathrm{eq}} = \frac{2\pi R_*}{P_{\mathrm{rot}}} \tag{4.39}$$

$$v_{\mathrm{eq}} \propto \frac{\mathcal{N}(R_*, \sigma^2_{R_*})}{\mathcal{N}(P_{\mathrm{rot}}, \sigma^2_{P_{\mathrm{rot}}})} \tag{4.40}$$

may not necessarily be a Gaussian. This is because the quotient, or the ratio, of two independent Gaussian distributions generally **does not** yield a Gaussian

distribution [3].

However, Bowler et al. [Bow+23] pointed out there are cases where the ratio of two independent Gaussian distributions can still be approximated with a Gaussian distribution. The approximation is valid if the denominator Gaussian has a small uncertainty. Intuitively, the denominator Gaussian must be precise that it can be approximated as a constant, making Equation 4.40 effectively not a ratio of two Gaussian distributions. In the application of $v_{\mathrm{eq}}$, this means that stellar rotation period $P_{\mathrm{rot}}$ measurement must have an uncertainty $\lesssim 20\%$ of its measured values. Bowler et al. [Bow+23] provided the closed-form solution to compute the stellar inclination $i_*$ of a range of stars based on observational measurements of $v \sin i_*$, $P_{\mathrm{rot}}$, and $R_*$. All of their $P_{\mathrm{rot}}$ measurements have uncertainties $\lesssim 20\%$, which means the equatorial velocity $v_{\mathrm{eq}}$ of all stars in Bowler et al. [Bow+23] can be approximated with a Gaussian distribution and the closed-form solution of Equation 4.37 is valid for every one of them.

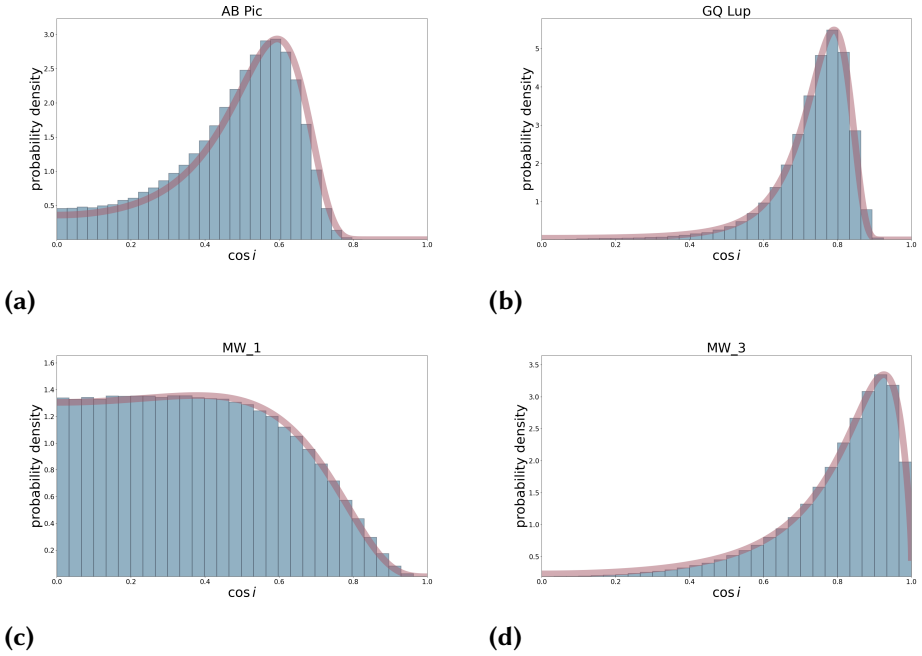


**Figure 4.9:** PDF of $\cos i_*$ for four benchmark cases. Panel (a): AB Pic, (b): GQ Lup, with measurements from Bowler et al. [Bow+23]. Panel (c): Illustrative case no. 1, (d) no. 3, from Masuda and Winn [MW20]. Continue in Figure F.1. Blue bars are the marginal posterior PDF from my MCMC simulation while the pink line is the analytical marginal posterior PDF from Equation 4.38.

3 The mathematical derivation of why this is the case is described nicely in this blog: https://davmre.github.io/blog/statistics/2015/03/27/gaussian_quotient accessed in August 2024. The main intuitive argument is that, for the ratio of two Gaussians to result in a Gaussian, the reciprocal of a Gaussian $1/\mathcal{N}(\mu, \sigma^2)$ would also need to be Gaussian. However, this is not true in the case of $1/\mathcal{N}(\mu, \sigma^2)$ because $1/e^{-x} = e^x$ implies that the "probability" increases as $x$ moves further away from $\mu$ and it has an open-bell curve. This makes $1/\mathcal{N}(\mu, \sigma^2)$ invalid as a probability distribution.

Hence, I could use the measurements in Bowler et al. [Bow+23] and Masuda and Winn [MW20] as a benchmark for my MCMC sampling. I numerically computed the posterior PDF of $\cos i_*$ using MCMC for three random stars (AB Pic, GQ Lup, HN Peg) from the reported $v \sin i_*$, $P_{\rm rot}$, and $R_*$ with their respective uncertainties in Bowler et al. [Bow+23]. For the four cases from Masuda and Winn [MW20], I assumed a $R_* = 1.0 \pm 0.1\, R_\odot$ and $P_{\rm rot} = 5.090 \pm 0.88$ days which were tailored to give $v_{\rm eq} = 10 \pm 2.0$ km/s. All measurements can be represented by a Gaussian distribution.

For the MCMC computation, the likelihood function is derived from the PDFs of the observed values of $P_{\rm rot}$, $R_*$, and $v \sin i_*$. The informed prior is a uniform PDF for $\cos i_*$ between 0 and 1. In each iteration, I randomly generated values for $P_{\rm rot}$ and $R$ and calculated their individual likelihoods based on their respective PDFs. Using these values, I computed the corresponding $v_{\rm eq}$. Then, by sampling $i_*$ from the uniform distribution in $\cos i_*$, I calculated $v \sin i_*$ and evaluated its likelihood using the observed $v \sin i_*$ PDF. Based on the likelihoods of the randomly generated values, the MCMC estimates the PDF of $\cos i_*$ computationally. For each star, I ran 50,000 iterations with 50 walkers.

I then compared the posterior PDF of $\cos i_*$ from my MCMC sampling with the analytical solution given in Equation 4.38. The comparisons are given in Figure 4.9 and Figure F.1. From the results of the benchmarking, it could be concluded that my MCMC sampling gave similar results to the analytical solutions of Bowler et al. [Bow+23] in cases that Gaussian distributions are valid for all observables. Using MCMC sampling in this case is therefore a more powerful and versatile option than the analytical solution, since the posterior distribution of $\cos i_*$ can be computed without requiring any of the observables to have Gaussian distributions.

The final $i_*$ PDF for TIC 206544316 is computed using the same MCMC procedure that has been benchmarked. The PDF for $R_*$ is from Table 4.1, $P_{\rm rot}$ from Section 4.4.2, and $v \sin i_*$ from Section 4.5.1. Similar to the benchmarking, I ran 50,000 iterations with 50 walkers.

## 4.6 Flare lightcurve: removing stellar modulation

After deriving the required stellar parameters from the photometric and spectroscopic data, the next "ingredient" to constraining the flare latitude $\theta_f$ is to get the flare-only lightcurve. This means removing the stellar modulation, or extracting the flare signal from the modulation, before proceeding with any modeling or calculations.

To remove the stellar modulation, I used a method similar to that described in Section 4.4.2. A template modulation pattern was created from the folded lightcurve. To make sure that the modulation template closely resembled the pattern during the flare, I used only the five modulation cycles preceding the giant flare. The dataset is defined as:

$$D_{\text{pre-flare}} = \{(t_n, F_n) \mid n = 1, 2, ..., N\}, \tag{4.41}$$

where $1332 < t_n < 1334.5$.

Next I used $P_{\text{rot}}$ from Section 4.4.2 to fold the lightcurve with the same $T_{\text{epoch}}$. I calculated the phase for each time point using Equation 4.10. I then binned the folded lightcurve to 300 bins and used rolling median to smooth the lightcurve. Any values above $1\sigma$ were removed. The modulation pattern is also represented with Equation 4.11. Interpolating the modulation pattern returned a function to generate an array of the underlying modulation, which is expressed by Equation 4.13. Hence, the flare is removed by calculating:

$$F_{\text{flare-only}}(t) = F(t) - I_M\left(\frac{t - T_{\text{epoch}}}{P} \mod 1\right), \tag{4.42}$$

along $1334.5 < t < 1336.5$, when the flare occurred (see Section 4.2.1). $F(t)$ is the flux at any given time $t$.

I also removed small sympathetic flares by inspecting the resulting lightcurve manually. I removed three flares in the dataset, two are instantly recognizable in Figure 4.1, but the other one was detected after the modulation pattern was removed. The third flare is a small increase in brightness at $t = 1336$. The resulting lightcurve that is passed to my MCMC sampling is given in Figure 5.4.

## 4.7 Flare localization

Localizing a flare on other stars than the Sun is challenging because we can not resolve the star as a disk. Section 2.3.2 outlines methods that have been used in literature to localize stellar flares and the challenges each of them hold. To localize the giant flare in TIC 206544316, I used the method developed by Ilin et al. [Ili+21b]. This method makes use of flares that last longer than a full rotation of the star, which are statistically more plausible to happen in fast-rotating stars, such as scallop-shell stars.

The premise is this: a flare that occurs long enough on a star that rotates fast enough will be modulated by the star's rotation. As a result, the lightcurve of these flares have a distinct shape, characterized by the movement in and out of view of the flaring region. This is illustrated in Figure 4.10. They are called **rotationally-modulated flares.** The advantage of this method is the possibility to localize the flare solely from its lightcurve compared to Doppler imaging that is generally more expensive and methods that require additional occulting object.

The first step to localize the giant flare of TIC 206544316 with this method is to confirm that it is a rotationally-modulated flare. The flare lightcurve (see Figure 5.9) from Section 4.6 shows that it indeed has the decaying bumps from being modulated by the star's rotation, making the giant flare a giant rotationally-modulated flare. There are two ways to extract the flare latitude from the rotationally-modulated

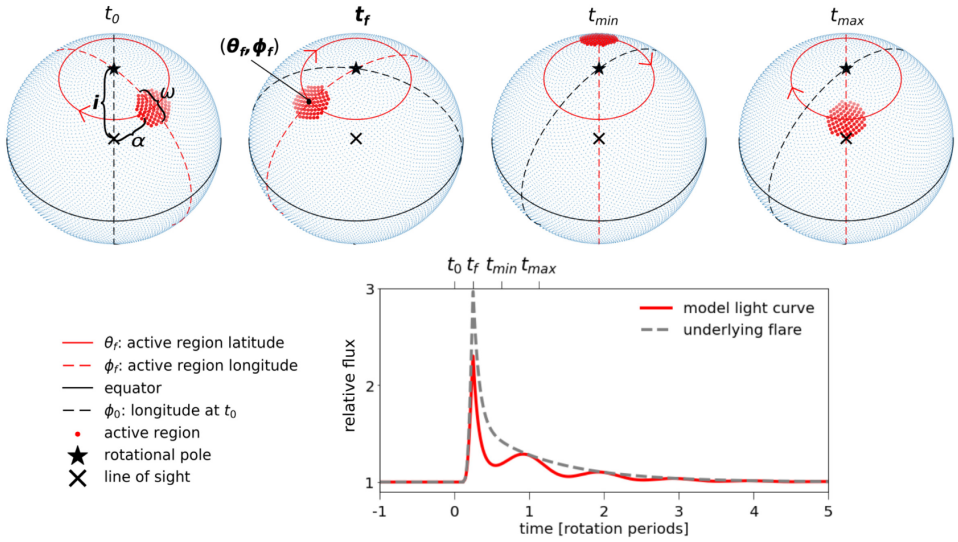


**Figure 4.10:** Flare modulation model. From left to right: a rotating star with a flaring region (red dots) is shown, starting at the beginning of observation time, $t_0$ and progressing to the peak flare time, $t_f$. It continues through $t_{\min}$, where the flare appears on the far side, and ending at $t_{\max}$, with the flare visible on the near side. The angle $\alpha$ denotes the angular distance between the stellar rotational pole (black star), while $\omega$ represents the full opening angle of the circular flaring region. As the flare cools and dims, rotational modulation produces a bumpy profile in the flare lightcurve (red line), despite the underlying flare maintaining the exponential decay characteristic of a classical flare (dashed grey line). From Ilin et al. [Ili+21b].

flare.

The first and simpler method is to use the **night length** (Section 4.7.1), the length of time the flare is behind the star. The second method is to model the rotationally-modulated flare (Section 4.7.2). The shape of the lightcurve of these flares vary depending on the stellar inclination $i_*$ and the flare latitude $\theta_f$. By modeling the presence or absence of the flare and its morphology, if $i_*$ is already known, then $\theta_f$ can be inferred.

### 4.7.1 Night length

The Earth's rotation axis is tilted at an angle of 23.5° away from its orbital axis as the Earth orbits the Sun. This means, on certain time of the year, regions at different latitude experience different length of day and night. Similarly, this concept can be applied to a flare that is rotationally-modulated. If the stellar inclination is known, the duration where the flare is in front of the star (day length) or behind (night length) can be used to approximate its latitude $\theta_f$. Due to the shape of the lightcurve, it is easier to determine the night length instead of the day length, because it is simply the gap between each bumps.

Illustration of deriving the flare latitude from the night length is given in Figure

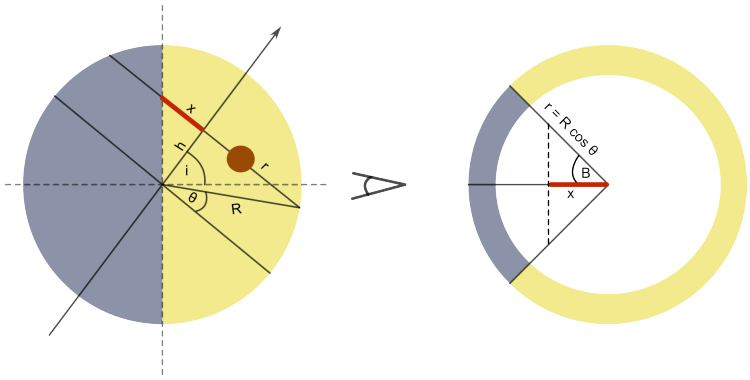


**Figure 4.11:** Illustration of determining the flare latitude $\theta_f$ from night length. Left: A flaring region (grey circle) located at a specific latitude on the stellar surface. The side of the star facing the observer is the day side (yellow), while the opposite side is the night side (grey). If the stellar inclination $i_*$ is known, then the amount of time the flaring region spends on the day or night side becomes a function of its latitude, similar to the variation in day length on Earth. Right: The star viewed from its rotational pole, illustrating the proportion of day (yellow) and night (grey) experienced at a given latitude.

4.11. Let circle $O_f$ represent the location of the flare at latitude $\theta_f$. From the left figure in Figure 4.11, it can be seen that:

$$\tan\left(\frac{\pi}{2} - i_*\right) = \frac{x}{h} \rightarrow h \tan\left(\frac{\pi}{2} - i_*\right) = x \tag{4.43}$$

$$\cos\theta_f = \frac{r}{R} \rightarrow R \cos\theta_f = r \tag{4.44}$$

$$\tan\theta_f = \frac{h}{r} \rightarrow r \tan\theta_f = h \tag{4.45}$$

Substituting Equation 4.44 and 4.45 to Equation 4.43 yields:

$$h \tan\left(\frac{\pi}{2} - i_*\right) = x \tag{4.46}$$

$$R \cos\theta_f \tan\theta_f \tan\left(\frac{\pi}{2} - i_*\right) = x \tag{4.47}$$

$$R \sin\theta_f \tan\left(\frac{\pi}{2} - i_*\right) = x \tag{4.48}$$

Figure 4.11 at the right shows the percentage of the sphere at day and night for a specific latitude if it was seen from the poles. The night length is the arc corresponding the angle $2B$. I can therefore write:

$$R \cos\theta_f \cos B = x. \tag{4.49}$$

Substituting Equation 4.48 to Equation 4.49 allows me to derive the angle B:

$$R \cos\theta_f \cos B = R \sin\theta_f \tan\left(\frac{\pi}{2} - i_*\right) \tag{4.50}$$

$$B = \arccos\left(\tan\theta_f \, \tan\left(\frac{\pi}{2} - i_*\right)\right). \tag{4.51}$$

The night length can then be described as the ratio of the arc subtended by angle $2B$ to a full circle. This is written as:

$$P_{\text{night}} = \frac{2B}{2\pi} \times P_{\text{rot}}. \tag{4.52}$$

Substituting Equation 4.51 to Equation 4.55, with considering only one hemisphere, thus $\theta_f$ only ranges from $(0, 90)$, results in:

$$\frac{P_{\text{night}}}{P_{\text{rot}}} = \frac{1}{\pi} \arccos\left(\tan\theta_f \, \tan\left(\frac{\pi}{2} - i_*\right)\right) \tag{4.53}$$

$$\cos\left(\frac{P_{\text{night}}}{P_{\text{rot}}} \times \pi\right) = \tan\theta_f \, \tan\left(\frac{\pi}{2} - i_*\right), \tag{4.54}$$

where $\theta_f$ then can be expressed as:

$$\theta_f = \arctan\left(\frac{\cos\left(\frac{P_{\text{night}}}{P_{\text{rot}}} \times \pi\right)}{\tan(\frac{\pi}{2} - i_*)}\right). \tag{4.55}$$

To determine the night length $P_{\text{night}}$, I visually marked the start and end of each bump in the flare lightcurve (see Figure 5.9). From the markings, it can be seen that there are four "bump gaps" with their corresponding night length. Each values of $P_{\text{night}}$ is expressed in fraction of $P_{\text{rot}}$. Since all four values were identical, I did not need to average them and instead used one representative value.

I used this method to derive the PDF of the flare latitude $\theta_f$ as a first approximation because of it is simpler compared to modeling the entire lightcurve. To get the PDF, I substituted the PDF of $i_*$ (Figure 5.7 (a)) from Section 4.5.2 to Equation 4.55. I then used the resulting PDF of $\theta_f$ to compare the results with the PDF of $\theta_f$ from the MCMC. This PDF of $\theta_f$ is notated as $P(\theta_f|D_{\text{night}})$.

### 4.7.2 Modeling a rotationally-modulated flare

Modeling the lightcurve of the rotationally-modulated flare offers a more sophisticated method of determining the flare latitude compared to the night length method. Modeling the lightcurve means using the full shape of the data, which gives better constraints of the PDF for $\theta_f$.

Ilin et al. [Ili+21b] developed an open-source Python software that modeled rotationally-modulated flares named `MalachiteMountains`. The basis of the model is placing a flaring region from an erupting flare on a rotating sphere with a certain latitude $\theta_f$ and longitude $\Phi_f$. The integrated flux that is observed is determined by the visible area of the flaring region as it decays and gets modulated by the stellar rotation (see Figure 4.10). By taking different coordinates of the flare $(\theta_f, \Phi_f)$, the stellar inclination $i_*$, and the underlying flare parameters, the

model can help approximate the best values that describe the data. To get the final posterior PDF of $\theta_f$, I used this flare modulation model and sampled the posterior PDF using MCMC.

The flare modulation model operates under several assumptions:

**First, the underlying flare, which is the shape of the flare that is it not modulated, is based on an empirical flare model**. `MalachiteMountains` originally uses the Davenport classical flare model [Dav+14]. This is described as:

$$F_{\rm rise} = 1 + 1.941\,{\rm FWHM}_i - 0.175\,{\rm FWHM}_i^2 - 2.246\,{\rm FWHM}_i^3 - 1.125\,{\rm FWHM}_i^4 \tag{4.56}$$

$$F_{\rm decay} = 0.6890\,e^{-1.600\,{\rm FWHM}_i} + 0.3030\,e^{-0.2783\,{\rm FWHM}_g}, \tag{4.57}$$

where $\mathrm{FWHM}_i$ and $\mathrm{FWHM}_g$, the FWHM of the impulsive and gradual decay phase, respectively, along with the flare amplitude $A_f$, describe the intrinsic shape of the flare lightcurve.

**Second, the flare emission is described as a blackbody with an effective temperature $T_f = 10,000$ K in the optical**. The source of this emission is from the photospheric footprint of the flaring loop, i.e., the flaring region. In Section 2.3.1, I discussed that the validity of the blackbody as a flare radiation model is still an ongoing investigation. While it is indeed true that more observations of flare spectra argue against a blackbody emission for a flare in the optical, the dataset that I have are from TESS that lies in the redder part of the optical range. In this area of the electromagnetic spectrum, the flare emission does not differentiate significantly regardless if it is described a blackbody or any other flare radiation model. What matters from the radiation model for this context is the role of the temperature of the flare $T_f$ in affecting the size of the flaring region. In the flare modulation model, hotter $T_f$ would return larger flaring region.

**Third, the flare is optically thick**. This assumption is related to the second assumption. The flare emission with a blackbody is modeled to originate from the flaring region on the photosphere, which is optically thick. Its optical thickness allows the flare to be modulated. If the flare is optically thin its emission would still be visible even as it begins to rotate behind the star. This would cause a more drastic drop in emission when it is finally hidden by the star, rather than a gradual dimming. The shape of the dimming from each bumps in the lightcurve shows a gradual dimming that is expected of an optically-thick emission source, making this assumption reasonable within the data that I am working with.

**Fourth, the flaring region is modeled as a simple spherical cap and is co-spatial with the location of magnetic field emergence**. In our Sun, flares occured in magnetically-complex regions (Section 2.3.2). Ilin et al. [Ili+21b] noted that non-circular regions may cause departures from the flare modulation model, but it is more problematic for when the flaring region moves across the stellar

limb than when it is fully in view. Ilin et al. [Ili+21b] found that effect of limb darkening the flare modulation model is negligible, making the non-circular regions not an immediate concern. What may exist as a caveat of this model is the assumption that the flaring region and the location of the magnetic field emergence, that causes the flare, stays in the same place for the entire duration of the flare. Interpretation of the result of this modeling that involves the location of the flaring region and the magnetic field concentration has to take this into account.

**Lastly, differential rotation is negligible**. It is known that differential rotation exists in the Sun, where the rotation speed is slower in the solar poles than in its equator. This results in different $P_{\rm rot}$ for a range of latitude in the solar surface and one value of $P_{\rm rot}$ should give poor fit to the lightcurve. However, Barnes et al. [Bar+17] found that fully convective M dwarfs show results that are more consistent with solid body rotation. The single $P_{\rm rot}$ value describes my dataset well with a stable period (see Section 4.4 and Figure 5.3). Regardless, if differential rotation does exist in the star, and it is solar-like, Ilin et al. [Ili+21b] noted that any result derived from the flare modulation model is closer to the equator than the real flare latitude.

### Modeling framework

With the general assumptions and limitations are addressed, `MalachiteMountains` works in three parts:

1. Determine the flaring region size from the flare parameters,
2. Distribute the flaring region into spatial elements, and
3. Apply modulation to the flare lightcurve and sum the spatial elements to get the modeled luminosity.

Let $L_{f,\rm max}$ be the maximum observable flare luminosity, which is the luminosity of a flaring region that is centered on the line of sight. If the specific flare flux is defined by $F_{f,s}(T_f)$, where $T_f$ is the effective temperature and $\omega$ is the full opening angle of the cap with values between 0 and $\pi$ (see Figure 4.10), $L_{f,\rm max}$ can be written as:

$$L_{f,\rm max} = \pi\, R^2\, F_{f,s}(T_f)\, \sin^2\!\left(\frac{\omega}{2}\right). \tag{4.58}$$

$L_{f,\rm max}$ is also a product of $A_f$ with the quiescent luminosity $L_*$ of the star in the TESS band:

$$L_{f,\rm max} = A_f \cdot L_*. \tag{4.59}$$

Combining Equation 4.58 and 4.59 returns the radius of the flaring region:

$$\frac{\omega}{2} = \arcsin\left(\sqrt{\frac{A_f \cdot L_*}{\pi\, R^2\, F_{f,s}(T_f)}}\right). \tag{4.60}$$

The flaring region with radius $\omega/2$ centered on $(\theta_f, \Phi_f)$ is then represented as an ensemble of $N$ data points. The ensemble has an even spatial distribution, such that each spatial element emit the same flux:

$$F_f(t) = L_F(t)/N, \tag{4.61}$$

where $F_f(t)$ is the empirical flare model.

The model requires time to be expressed as phase in radian, which is similar to Equation 4.10 but without the modulo. It can be written as:

$$t_f = \frac{2\pi(t - T_{\text{epoch}})}{P_{\text{rot}}}. \tag{4.62}$$

I converted the lightcurve of TIC 206544316, $F_{\text{flare-only}}(t)$ in days to $F_{\text{flare-only}}(t_f)$ in radian. In this case, $T_{\text{epoch}}$ is not the epoch of the flare modulation in Section 4.4.2. Instead, it is the defined starting time of the flare.

The flare modulation is defined by the geometrical foreshortening [see Ili+21b, for more details]. For a given area $A$, the foreshortened area with an incidence angle $\alpha$ is $A \cos\alpha$. Every spatial element $(\theta_f, \Phi_f)$ of the flare can therefore be expressed as:

$$F_f(\theta_f, \Phi_f, t_f) = F_f(t_f)\ \cos\alpha(\theta_f, \Phi_f, t_f), \tag{4.63}$$

where $\alpha(\theta_f, \Phi_f, t_f)$ is given by:

$$\alpha = \arccos\Big(\sin\theta_f\ \cos i_*\ +\ \cos\theta_f\ \sin i_*\ \cos(\Phi_f - \Phi_{f,0} - t_f)\Big), \tag{4.64}$$

with $\Phi_{f,0}$ as the flare longitude when the flaring region is on the line of sight.

The night length in Equation 4.53 determines whether the spatial element is visible. As the sphere rotates and $\Phi_f$ evolves in time, the step function $d$ can be determined from the night length and $\Phi_{f,0}$. The step function $d$ returns 1 when the spatial element is visible, and 0 when it is hidden. Finally, from the step function $d$ the flare modulation model can now be fully expressed as:

$$F_{\text{model}}(\theta_f, \Phi_f, t_f) = F_f(\theta_f, \Phi_f, t_f)\, d(\theta_f, \Phi_f, t_f). \tag{4.65}$$

### Flare model: Classical flare

At the beginning of my data analysis, I used the cassical flare model [Dav+14] that is automatically embedded in `MalachiteMountains` (see Figure 2.4). This means $F_f(t_f)$ is described by Equation 4.56. Hence, the flare modulation model in Equation 4.65, for a decoupled underlying flare model, has seven parameters:

$$\Theta = [i_*, \theta_f, \Phi_{f,0}, A_f, \text{FWHM}_i, \text{FWHM}_g, t_{\text{peak}}], \tag{4.66}$$

where $i_*$, the stellar inclination, $\theta_f$, the flare latitude, and $\Phi_{f,0}$, the flare longitude at $t_0$, determine the geometry of the modulation, and $A_f$, the flare amplitude, along

with the FWHM of the impulsive and decay phases, FWHM$_i$ and FWHM$g$, and $t$peak describe the underlying flare model. In the model, $t_{\rm peak}$ is the time of the flare's peak. This time signals the end of the impulsive phase and switches to the gradual decay phase.

By modeling the uncertainties of the lightcurve ($\sigma_n$) as Gaussian and independent, the likelihood function can be defined as:

$$\log \mathcal{L}(F|\Theta) = -\frac{1}{2}\sum_{n=1}^{N}\left[\frac{(F_{\text{flare-only}}(t_f) - F_{\text{model}}(t_f;\Theta))^2}{\sigma_n^2} + \log \sigma_n^2\right]. \tag{4.67}$$

The uninformative prior PDFs for the parameters are given in Table 4.7. The PDF $P(\cos i_*|D)$ is provided as a discrete distribution. To obtain probabilities from the prior PDF, I linearly interpolated the PDF at each time step.

| Parameter | Prior |
|---|---|
| Uninformative | |
| $\Phi_{f,0}$ | $\mathcal{U}(0, 2\pi)$ |
| $A_f$ | $\mathcal{U}(2, 8)$ |
| FWHM$_i$ | $\mathcal{U}(0, 0.01\pi)$ |
| FWHM$_g$ | $\mathcal{U}(0, 0.025\pi)$ |
| $t_{\rm peak}$ (radian) | $\mathcal{U}(0, 30)$ |
| Informative | |
| $\cos i_*$ | $\log P(\cos i_*\|D)$ |

**Table 4.7:** Parameters of the model and the prior PDF for the MCMC for the classical flare. $P(\cos i_*|D)$ is derived in Section 4.5.2.

I sampled the posterior PDF using `emcee` with parallelization using 16 CPU threads. While the prior PDFs and the equation looks straight-forward, the reality was far from that. In fact, for lack of better wordings to express the frustration I felt at this point of the data analysis, the MCMC sampling was an *epic fail*. It never converged, no matter how many iterations I tried and how many walkers I deployed. I changed the priors and initial values for each parameters to see how the parameters contribute to the likelihood estimation. I coupled and de-coupled the flare with different values. Nothing seemed to work during *any* of the runs[4].

The problem appears to be that the bumps did not behave like a normal exponential decay. To fit the first bump, the $F_{\rm model}$ for the later bumps were too low, and

4 Possibility of graduation, at that point, was internally questioned. Seriously, internally questioned.

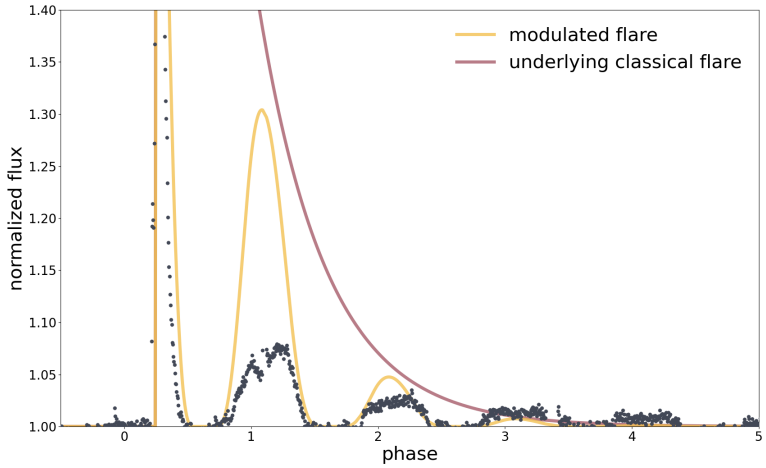


**Figure 4.12:** A simulated rotationally modulated flare (yellow) is generated using the classical flare (red line) as the underlying, non-modulated flare. However, the modulated flare does not match the data (black) because the $\mathrm{FWHM}_g$ must be large enough to span all four bumps. However, when it is, the first two bumps, especially the first, are overestimated while the later bumps are still underestimated.

vice versa (Figure 4.12). The model never gave a solution that balanced the bumps. After some time of running the MCMC sampling with the classical flare model, I came to the conclusion that the giant flare in TIC 206544316 cannot be described by the classical flare model. A new flare model is needed to describe this flare.

### Flare model: Peak-bump flare

An alternative to the classical flare model is the peak-bump flare model described by Howard and MacGregor [HM22, see Figure 2.6]. The peak-bump flare model describes an additional bump during the gradual phase that occurred after the flare peak. The model essentially adds a Gaussian bump on top of the classical flare model. It is, at this point, only a mathematical model. The Gaussian bump is arbitrarily chosen such that it is not tied into a specific physical process. It serves as a function to explain the additional bump.

The additional Gaussian bump is described by:

$$\mathcal{N}(t;\Theta_{\mathrm{bump}}) = A_{\mathrm{bump}}\, e^{-\frac{1}{2}\frac{(t-t_{\mathrm{bump}})^2}{\sigma^2_{\mathrm{bump}}}}, \tag{4.68}$$

where $\Theta_{\mathrm{bump}} = [A_{\mathrm{bump}}, t_{\mathrm{bump}}, \sigma_{\mathrm{bump}}]$. The parameters correspond to the amplitude, the location of the center, and the standard deviation of the Gaussian bump. The peak-bump flare model is fully written as:

$$F_{\mathrm{model}}(\theta_f, \Phi_f, t_f, \Theta_{\mathrm{bump}}) = \big(F_f(\theta_f, \Phi_f, t_f)\, d(\theta_f, \Phi_f, t_f)\big) + \mathcal{N}(t_f;\Theta_{\mathrm{bump}}). \tag{4.69}$$

Therefore, the full set of parameters are now defined by:

$$\Theta = [i_*, \theta_f, \Phi_{f,0}, A_f, \mathrm{FWHM}, t_{\mathrm{peak}}, A_{\mathrm{bump}}, t_{\mathrm{bump}}, \sigma_{\mathrm{bump}}]. \tag{4.70}$$

For computational efficiency, I decided to couple the impulsive and gradual phase, as originally defined in Davenport et al. [Dav+14]. The coupled flare model uses $\mathrm{FWHM} = \mathrm{FWHM}_i = \mathrm{FWHM}_g$ in Equation 4.56. The likelihood function remains the same as Equation 4.67. The additional peak-bump parameters and their prior PDF are given in Table 4.8.

| Parameter | Prior |
|---|---|
| Uninformative | |
| $\mathrm{FWHM}_f$ | $\mathcal{U}(0, 0.01\pi)$ |
| $A_{\mathrm{bump}}$ | $\mathcal{U}(0, 10)$ |
| $t_{\mathrm{bump}}$ (radian) | $\mathcal{U}(t_{\mathrm{peak}}, 30)$ |
| $\sigma_{\mathrm{bump}}$ | $\mathcal{U}(0, 100)$ |

**Table 4.8:** Additional parameters and the prior PDF for the MCMC simulation using a peak-bump flare model. $\Phi_{f,0}$, $A_f$, $t_{\mathrm{peak}}$, and $\cos i_*$ follow the prior PDF in Table 4.7.

I ran the MCMC sampling with `emcee` with 70,000 steps and 20 walkers. I also did parallelization with 16 CPU threads. Even with the parallelization, and reducing the number of parameters by coupling the flare, the running time of the MCMC sampling is around 7-8 hours. The MCMC sampler converged to an equilibrium Markov chain for all parameters, showing that the peak-bump flare is better at describing the observed lightcurve than the classical flare model.

## 4.8 Flare bolometric energy $E_{\mathrm{bol,f}}$

Another flare parameter that is of interest is the flare's bolometric energy $E_{f,\mathrm{bol}}$. Ideally, this would be derived from the flare's spectral energy distribution. However, for this particular flare, no spectroscopic data are available, as there was no dedicated observation campaign during the TESS monitoring. Only the TESS white-light flare lightcurve is available. Still, this does not make estimating the energy impossible. Shibata et al. [Shi+13] proposed a method for estimating flare energy using only the white-light flare lightcurve. Their approach assumes that the flare emission can be approximated by a blackbody with an effective temperature $T_f = 10,000$ K.

Using the blackbody approximation, the bolometric flare luminosity $L_f$ can be calculated as:

$$L_f = \sigma_{\mathrm{SB}}\, T_f^4\, A_f, \tag{4.71}$$

where $\sigma_{SB}$ is the Stefan-Boltzman constant and $A_f$ is the area of the flaring region. The area $A_f$ can be estimated using the observed stellar luminosity $L'_*$, the observed flare luminosity $L'_f$, and the normalized flare amplitude $C'_{\mathrm{f}}$. The observed stellar luminosity $L'_*$ is given by:

$$L'_* = \int R_\lambda \, B_{\lambda(T_{\mathrm{eff}})} \, d\lambda \cdot \pi \, R_*^2, \tag{4.72}$$

while the observed flare luminosity $L'_f$ is:

$$L'_f = \int R_\lambda \, B_{\lambda(T_f)} \, d\lambda \cdot A_f, \tag{4.73}$$

where $\lambda$ is the wavelength, $B_{\lambda(T)}$ is the Planck function for a given $T$, and $R_\lambda$ is the response function of the instrument. For TESS, the passband $R_\lambda$ spans $\sim 6,000 - 10,000$ Å [Ric+14].

Furthermore, the normalized flare amplitude $C'_f$ is defined simply as:

$$C'_f = L'_f / L'_*. \tag{4.74}$$

Note that $C'_f$ is a function of time. Thus, by combining Equation 4.72, 4.73, and 4.74, $A_f$ can be estimated as:

$$A_f = C'_f \, \pi \, R_*^2 \, \frac{\int R_\lambda \, B_{\lambda(T_{\mathrm{eff}})} \, d\lambda}{\int R_\lambda \, B_{\lambda(T_f)} \, d\lambda}. \tag{4.75}$$

Finally, substituting Equation 4.75 into 4.71 gives the flare luminosity $L_f$ as a function of time. The bolometric flare energy $E_{f,\mathrm{bol}}$ can then be estimated by integrating $L_f$ over time:

$$E_{f,\mathrm{bol}} = \int L_f(t) \, dt. \tag{4.76}$$

To calculate $E_{f,\mathrm{bol}}$ for the giant flare, I used $T_{\mathrm{eff}}$ and $R_*$ from Table 4.1 and the flare lightcurve from Section 4.6.

# 5 Results

## 5.1 Stellar period $P_{\mathrm{rot}}$

In the effort to constrain the geometry of the material surrounding the scallop-shell star, the stellar rotation period $P_{\mathrm{rot}}$ serves as an important parameter for breaking the degeneracy between the stellar inclination $i_*$ and the flaring latitude $\theta_f$. As a first-order approximation, I derived the stellar period from TESS Sectors 1 and 2 using the Lomb-Scargle periodogram (Section 4.4.1). The resulting periodogram is shown in Figure 5.1. The period derived with the periodogram, $P_{\mathrm{LS}}$, corresponds to the period with the highest power and is reported as follows:

$$P_{\mathrm{LS}} = 0.3219345 \text{ days}.$$

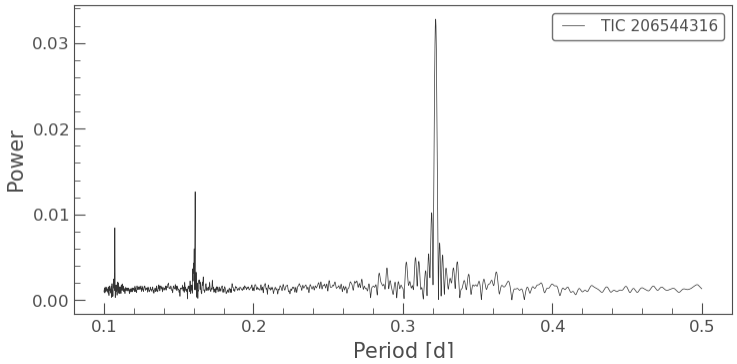


**Figure 5.1:** Lomb-Scargle periodogram for TIC 206544316 computed using `lightkurve`. The period with the highest power is taken as the Lomb-Scargle period.

However, the Lomb-Scargle periodogram is a disfavored method in this thesis, as it does not provide uncertainties that are useful for a Bayesian analysis and assumes the modulation is **only** represented by a cosine function (Section 4.4.1). To obtain the PDF of the stellar period, I used MCMC simulations 4.4.2. I computed MCMC simulations using two different likelihood functions: one based on a cosine function (Figure 5.2) and the other based on the empirical modulation template from the lightcurve (Figure 5.3).

The PDFs of each parameter, along with their correlations shown in corner plots, are given in Figures C.2 and C.4 for simulations using the cosine function and the modulation template, respectively. From the best-fit parameter samples, it can be seen that the model based on the cosine function fails to describe the data. As a result, the likelihood function was unable to constrain the MCMC walkers to converge on a single solution. This emphasizes raises red flags in using the Lomb-Scargle periodogram to stars with complex modulation patterns. The Lomb-Scargle

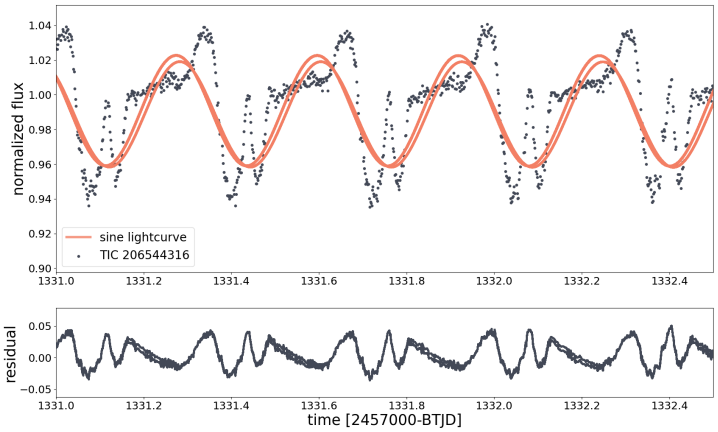


**Figure 5.2:** Sampling from the results of the MCMC simulations using a cosine function. The two sine curves show that the model fails to represent the data, leading the MCMC walkers to not converge properly and become stuck in alternative solutions. In such cases, where the model provides a poor fit, it is difficult to dismiss the diverging walkers simply as "strays."

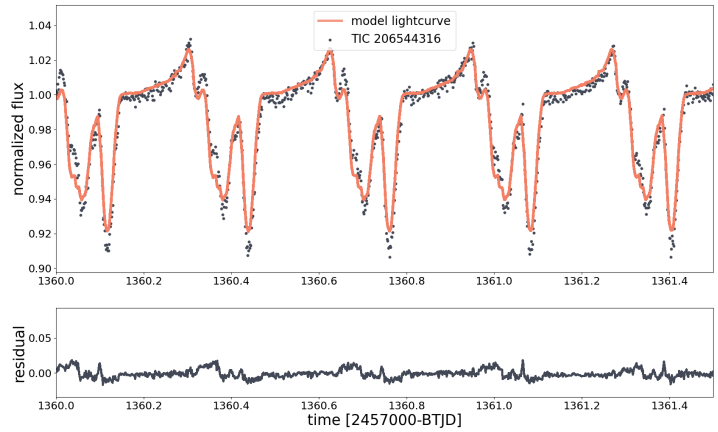


**Figure 5.3:** Sampling from the results of the MCMC simulations using the modulation template.

periodogram essentially returns a period assuming, or even enforcing, a sine/cosine modulation.

Hence, I adopted the PDF of the stellar period $P_{\rm rot}$ from the MCMC simulation using the modulation template, which yields:

$$P_{\rm rot} = 0.3219615 \pm 0.0000002 \text{ days},$$

or in minutes:

$$P_{\rm rot} = 463.6246 \pm 0.0003 \text{ minutes}.$$

It can be seen that the uncertainty in the period is very small, on the order of sub-seconds. The shortest interval between data points in the TESS dataset used (Section 4.2.1) is only two minutes. Therefore, it is reasonable to question whether the small uncertainties produced by the MCMC simulation makes physical sense. To address this, I examine the ephemeris equation to see why such small period uncertainties are expected. The ephemeris equation is given as:

$$T = T_{\rm epoch} + n\,P_{\rm rot}, \tag{5.1}$$

where $T_{\rm epoch}$ is the epoch of ephemeris and $n$ is the number of cycles. The period determination used data from Sector 1 and Sector 2, which covered $\sim$ 56 days of observations. Given the stellar period $P_{\rm rot}$, there are about 174 modulation cycles within the full data span.

Now, assume $P_{\rm true}$ and $T_{\rm true}$ represent the true period and time of a data point after $n$ cycles. Similarly, let $P_{\rm calc}$ and $T_{\rm calc}$ represent the calculated period and time of a data point after $n$ cycles. The difference between $T_{\rm true}$ and $T_{\rm calc}$ after $n$ cycles can then be expressed as:

$$T_{\rm true} - T_{\rm calc} = n(P_{\rm true} - P_{\rm calc}) \tag{5.2}$$

$$\Delta T = n\,\Delta P. \tag{5.3}$$

Equation 5.3 shows that time shifts become more noticeable after multiple cycles if the period is incorrect, meaning that the disagreement between the calculated time and the data accumulates over successive cycles. Consequently, a larger number of cycles naturally results in tighter constraints on the period fit.

Therefore, for a shift of two minutes between $T_{\rm true}$ and $T_{\rm calc}$ after 174 cycles, which would be noticeable from TESS 2-minute cadence, the following difference in period is approximately:

$$\Delta P \approx \frac{2\,\text{min}}{174}$$
$$\Delta P \approx 0.01\,\text{min.},$$

which indicates that the period uncertainties must be as small as 0.01 minutes to accurately account for the 174 modulation cycles.

Note that the uncertainties in $P_{\rm rot}$ derived from the MCMC analysis are still two orders of magnitude smaller than the estimated $\Delta P$. This is because the $\Delta P$ shown above corresponds to just one data point. **In reality, the entire modulation pattern in the last cycle is shifted**, involving a $\Delta P$ spread across roughly 100 data points. The MCMC simulation evaluates the overall likelihood across the dataset, allowing it to recover a more accurate posterior PDF. Furthermore, the modulation model is constructed directly from the dataset (Section 4.4.2). As a result, there exists an optimal configuration that fits the data the best, which leaves less wiggle room compared to an analytical model. The MCMC is able to identify that solution. Thus, the small uncertainty of $P_{\rm rot}$ is justified.

Note also that the $P_{\rm rot}$ derived in this section comes from the assumption that modulation pattern is caused by the star or something that is co-rotating with the star. I believe this assumption is reasonable because it can be seen in Figure 4.1 that the flare, which occurred in the stellar photosphere and shown to be modulated by the stellar rotation, is exactly in sync with the period and evolution of the modulation pattern, i.e., the impulsive brightening and the bumps from the gradual decay phase occurred in the same modulation phase.

## 5.2 Modulation change

From Section 5.1, I studied the modulation change through the phase-folded light curve. Figure 5.4 (a) shows the phase-folded light curve of Sector 1, with data points separated into pre-flare and post-flare segments. Two main differences between the pre- and post-flare modulation patterns can be observed. Parameters of the dips on the post-flare modulation pattern are given in Table 5.1.

**First, an instantaneous dimming occurring around $\phi \approx 0.2$.** The modulation pattern transitions from a smooth, curve-like structure in the pre-flare data into a sharp, jagged dip in the post-flare pattern. **Note that the flare occurred at exactly the same phase.**

**Second, there is a gradual dimming for dips around $\phi \approx 0.4$ and $\phi \approx 0.6$.** Notably, the dip at $\phi \approx 0.6$ deepens gradually over time, in contrast to the sudden change seen at $\phi \approx 0.2$. Even more interestingly, the dimming at $\phi \approx 0.6$ appears to have begun before the flare occurred. The evolution of this change is clearly illustrated in Figure 5.5.

Furthermore, the modulation continued to evolve until the end of Sector 1, after which it stabilized for the entire duration of Sector 2. This is illustrated in Figure 5.4 (b), where the modulation pattern shows no significant changes. The modulation pattern in Sector 2 closely resembles the post-flare modulation in Sector 1, except for the depth of the dip $\phi \approx 0.6$. Hence, the modulation model used in Section 5.1

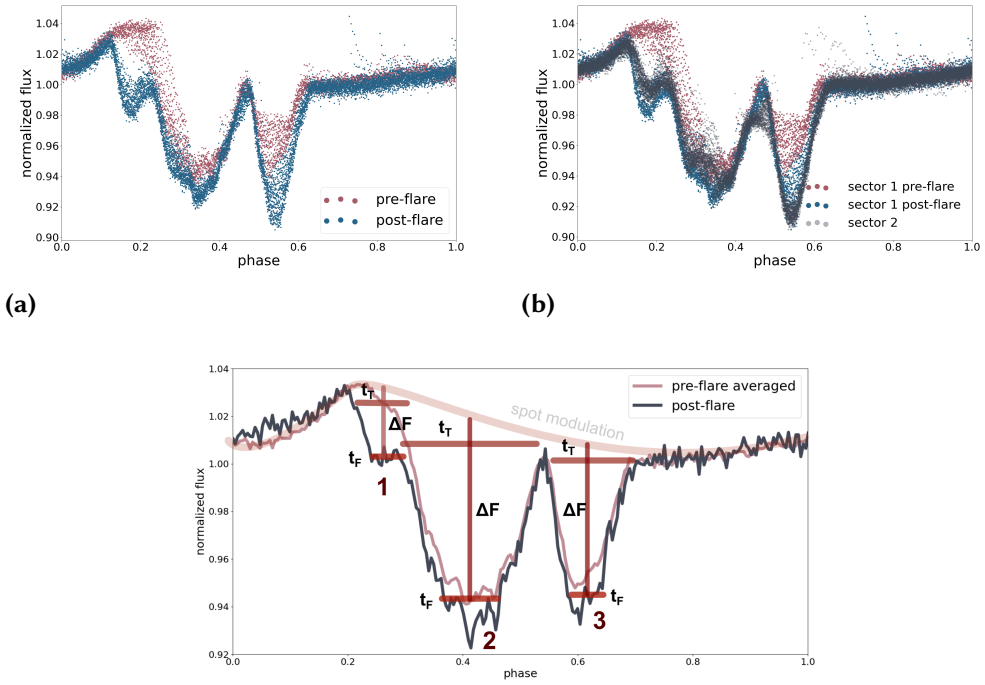


**(a)** **(b)**

**(c)**

**Figure 5.4:** Phase-folded light curves from Sector 1 (Panel a) and from both Sector 1 and Sector 2 combined (Panel b). Data points are color-coded by time: red represents TESS observations taken before the giant flare, blue represents those taken after the flare, and dark grey represents data from Sector 2. A stark change in the modulation pattern is observed in Sector 1 before and after the flare. In contrast, Sector 2 shows a very stable modulation pattern. This stable pattern in Sector 2 closely resembles the post-flare modulation seen in Sector 1. Panel (c): the modulation pattern marked with how the duration and depth of each dip is defined.

more closely matches the modulation in Sector 2 than the pre-flare modulation in Sector 1. The greater number of modulation cycles with the post-flare pattern likely washed out some of the structures from the pre-flare modulation. No giant flare occurred in Sector 2.

| Dip | 1 | 2 | 3 |
|---|---|---|---|
| Rotational phase $\phi$ | 0.2 | 0.4 | 0.6 |
| Total duration $t_T$ ($P_{\mathrm{rot}}$) | 0.12 | 0.25 | 0.15 |
| "Flat" duration $t_F$ ($P_{\mathrm{rot}}$) | 0.06 | 0.1 | 0.06 |
| Depth | 0.03 | 0.1 | 0.07 |

**Table 5.1:** Parameters of the different dips observed in the modulation pattern after the flare. Determination of each duration and depth is defined in Figure 5.4 (c).

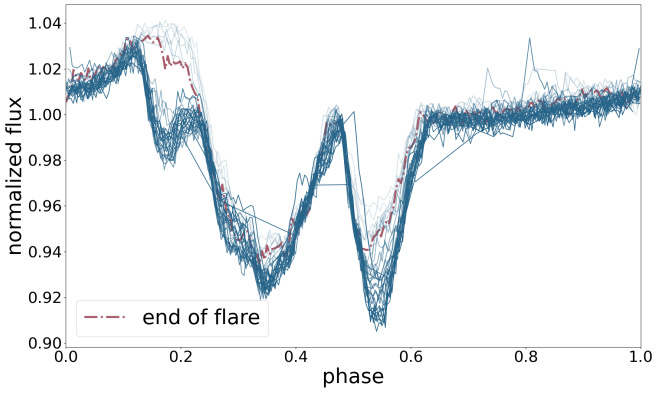


**Figure 5.5:** Evolution of the modulation pattern change in Sector 1. The thickness of the lines indicates the timing of the observations: thinner lines correspond to data taken near the beginning of Sector 1, while thicker lines represent data taken toward the end. The red dot-dashed lines mark the last modulation cycle before the giant flare. This plot reveals that the modulation change occurred in two parts: the left dip went an instantaneous change, while the right dip showed a gradual deepening over time.

| | Gaia RVS | MIKE-CARMENES |
|---|---|---|
| $v \sin i_*$ (km/s) | 67.89 ± 4.93 | 68.34 ± 5.70 |

**Table 5.2:** Average $v \sin i_*$ values derived from the calibration function for each reference star in the Gaia RVS and MIKE-CARMENES datasets.

## 5.3 Stellar inclination $i_*$

### 5.3.1 Projected rotational velocity $v \sin i_*$

The next parameter needed to remove the degeneracy between the stellar inclination $i_*$ and flare latitude $\theta_f$ is the projected rotational velocity $v \sin i_*$. I derived the projected rotational velocity $v \sin i_*$ of TIC 206544316 using the cross-correlation method from Section 4.5.1. The obtained $v \sin i_*$ values for the Gaia RVS and MIKE-CARMENES dataset are given in Figure 5.6 (a) and 5.6 (b), respectively. Each dataset provides a calibration function relating the FWHM of the cross-correlation function to $v \sin i_*$ based on the reference stars The best-fit $v \sin i_*$ for each dataset is obtained by averaging the calibrated $v \sin i_*$ from each independent reference star. These values are given in Table 5.2.

Both datasets gave similar results. Since the values are independent, meaning that they are derived from two separate datasets and spectral region, I can derive the best-fit $v \sin i_*$ for TIC 206544316 by averaging the values from both datasets. This returned:

$$v \sin i_* = 68.12 \pm 3.77 \text{ km/s}.$$

The projected rotational velocity $v \sin i_*$ further confirms that the star is a fast-rotator. At first glance, the $v \sin i_*$ values I obtained still do not include the value

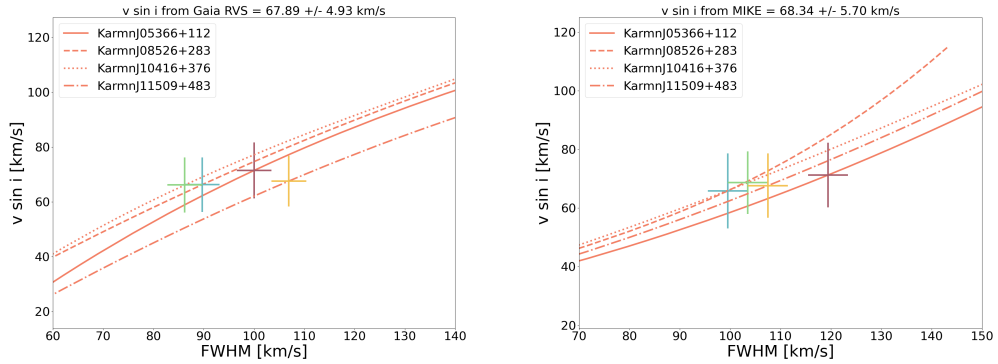


**(a)** **(b)**

**Figure 5.6:** Projected rotational velocity $v \sin i_*$ derived from the Gaia RVS (a) and MIKE-CARMENES (b) dataset. Pink lines: third order polynomial fits to the calibration functions ($f(\text{FWHM}) = v \sin i_*$, see Section 4.5.1) for four reference spectra. Four crosses: Fitted FWHM from the cross-correlation function with the corresponding $v \sin i_*$. Each cross indicates fits from different reference star.

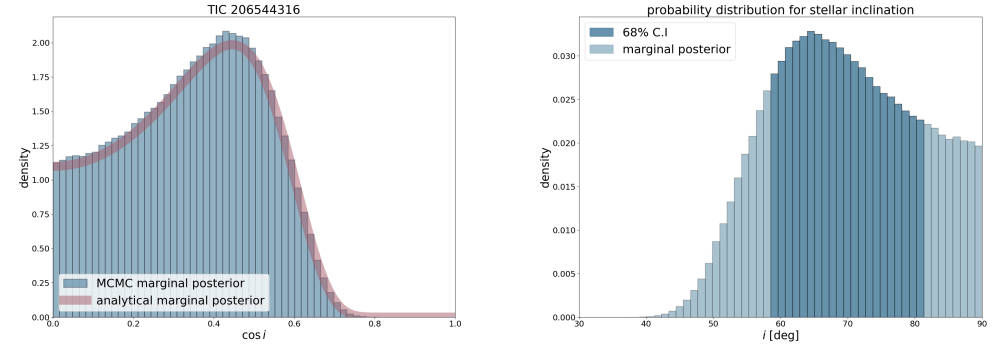


**(a)** **(b)**

**Figure 5.7:** The marginal PDF obtained from the Masuda and Winn [MW20] Bayesian analysis framework. Panel (a): PDF for $\cos i_*$. The blue histogram represent the PDF from the MCMC sampling. The pink line represents the analytical solution based on Bowler et al. [Bow+23]. Panel (b): PDF for $i_*$ from MCMC sampling. The dark blue histogram represent the distribution within 68% confidence interval, the 16th and 84th percentile.

of $v \sin i_* \approx 77$ km/s reported by Zhan et al. [Zha+19]. Because their analysis did not report any uncertainties, it is unclear whether the PDF of the values overlap. It is also unclear whether the $v \sin i_*$ values from Zhan et al. [Zha+19] is physically plausible. By calculating the equatorial velocity $v_{\text{eq}}$ using Equation 4.14 with $P_{\text{rot}}$ (Section 5.1) and $R_*$ (Table 4.1), I estimate the equatorial velocity $v_{\text{eq}}$ to be:

$$v_{\text{eq}} = 75.50 \pm 6.29 \text{ km/s}.$$

From the estimation of the equatorial velocity, I found that the $\approx 77$ km/s still falls within $1\sigma$ of the range of $v_{\text{eq}}$.

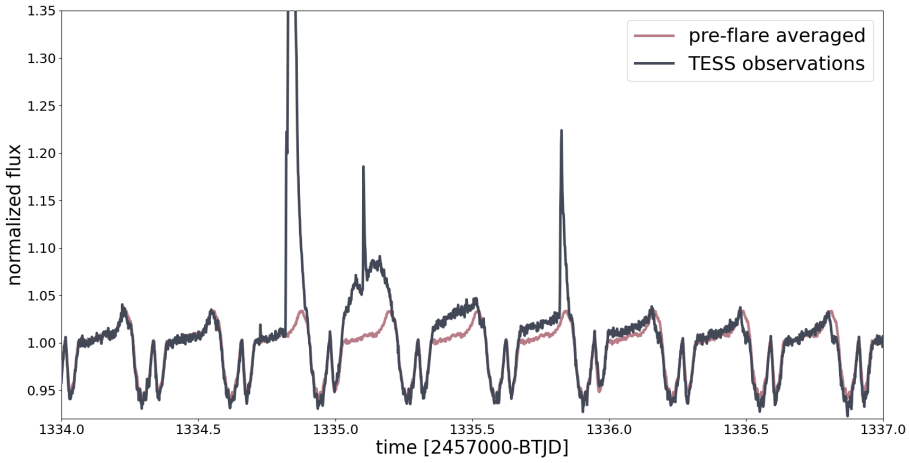


**Figure 5.8:** TESS lightcurve (black) overlined with a modulation template (pink) modeled from the pre-flare cycles. The obtained flare lightcurve is the substraction of the TESS lightcurve with the modulation template.

### 5.3.2 Marginal PDF of stellar inclination $i_*$

I then derived the PDF of the stellar inclination $i_*$ using the Bayesian framework of Masuda and Winn [MW20] (Section 4.5.2). I ran an MCMC simulation that has been benchmarked and compared to results from previous literature that used this framework. The stellar input parameters are the stellar period $P_{\rm rot}$ (Section 5.1), the stellar radius $R_*$ (Table 4.1), and the final $v \sin i_*$. The PDF of the stellar inclination $i_*$ from the MCMC analysis is given in Figure 5.7. Taking the 68% confidence interval (1-$\sigma$) from Figure 5.7 (b), which corresponds to the 84th and 16th percentiles, the stellar inclination $i_*$ derived from this analysis is given as:

$$i_* = 69^{+13}_{-11}\ ^\circ.$$

The results from the stellar inclination $i_*$ shows that TIC 206544316 has a near edge-on orientation. This means that a transiting material in the equator of the star would be observable, aligning with the hypothesis of an equatorial material as the cause of the scallop-shell phenomena.

## 5.4 Flare lightcurve

To remove the stellar modulation pattern and obtain the flare lightcurve, I created a modulation model using the method described in Section 4.4.2, but only taking into account the pre-flare modulations and the stellar period $P_{\rm rot}$. The TESS lightcurve with the pre-flare modulation model is shown in Figure 5.8. I then subtracted this pre-flare modulation model from the TESS lightcurve, giving me the flare-only lightcurve presented in Figure 5.9. As shown in Figure 5.9, it is clear that the giant flare of TIC 206544316 is a rotationally-modulated flare, displaying the characteris-

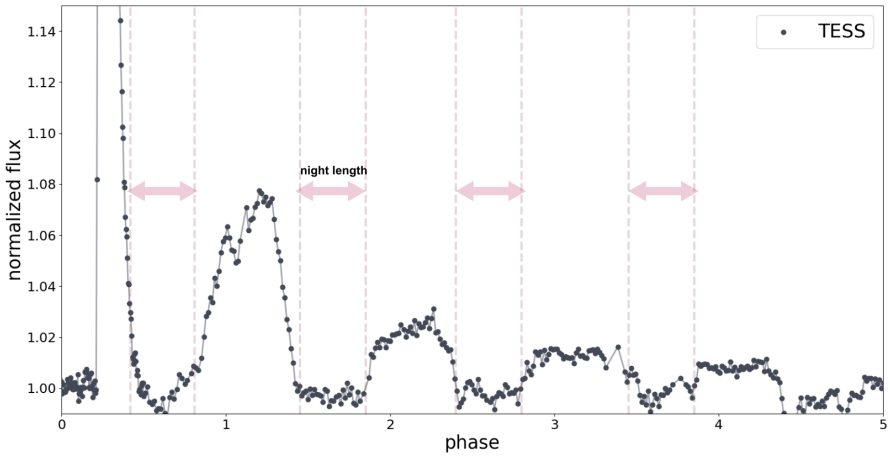


**Figure 5.9:** The flare-only lightcurve. The flare shows the characteristic decaying bumps of a rotationally-modulated flare, confirming that the flare is localizable. I observed four bumps that corresponded with four night lengths (faded red dashed lines). Note that the impulsive phase of the flare goes until 4× the quiescent flux and it is truncated in this plot to highlight the decaying bumps which mainly constraints the flare latitude.

tic decaying bumps.

From the flare lightcurve, I can then calculate the night length (Section 4.7.1), the time between two consecutive bumps when the flare is supposedly behind the star, for each of the decaying bump. There are four decaying bumps after the impulsive phase. The night length is $P_{\rm night} = 0.4\,P_{\rm rot}$ for all four bumps.

## 5.5 Flare latitude $\theta_f$

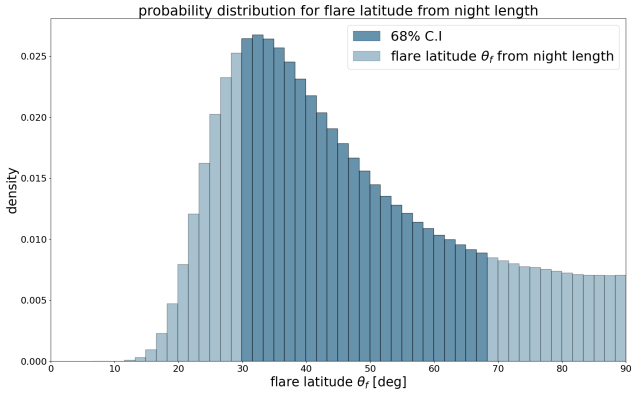


**Figure 5.10:** PDF of the flare latitude $\theta_f$ using the night length. The dark blue histogram represent the distribution within 68% confidence interval, the 16th and 84th percentile.

### 5.5.1 Night length

With the PDFs of all the necessary parameters to constrain the flare latitude now available, I proceeded to calculate the flare latitude. As a first approximation, I used the night length method (Section 4.7.1) to estimate the flare latitude $\theta_f$. By sampling the PDF of the stellar inclination $i_*$ from Figure 5.7 (b) and applying the Equation 4.55, I obtained the PDF of $\theta_{f,\mathrm{nl}}$ which is shown in Figure 5.10. The distribution indicates that the most probable values of $\theta_f$ fall within the range of $30 - 40°$, suggesting a low-latitude flare.

### 5.5.2 MCMC simulation results

| TIC 206544316 | |
|---|---|
| $P_{\mathrm{rot}}$ (min) | $463.6246 \pm 0.0003$ |
| $v \sin i_*$ (km/s) | $68.12 \pm 3.77$ |
| $i_*$ (deg) | $79.72^{(+1.12}_{-1.02)}$ |
| **Flare parameters** | |
| $A_f$ | $5.94 \pm 0.09$ |
| $\mathrm{FWHM}_f$ (min) | $9.56 \pm 0.02$ |
| $A_{\mathrm{bump}}$ | $1.110 \pm 0.002$ |
| $\mathrm{FWHM}_{\mathrm{bump}}$ (min) | $119.2^{(+11.1}_{-11.3)}$ |
| $\log_{10} E_f$ | $36.6502^{(+0.0007}_{-0.0006)}$ |
| $\theta_f$ (deg) | $35.70^{(+0.60}_{-0.63)}$ |

**Table 5.3:** Stellar and flare properties of TIC 206544316 from this thesis.

I then ran an MCMC simulation to derive the flare latitude $\theta_f$ using the full dataset and the PDFs collected (Section 4.7.2). The post-impulsive phase of the flare lightcurve (Figure 5.9) is binned for computation efficiency. 5.11 shows the best-fit result, illustrating the underlying flare and how it looks like after being modulated by the star's rotation. The full posterior PDFs of all parameters are presented in Figure 5.12.

The underlying flare shows an evident peak-bump profile, which tries to account for the height of the different bumps. The Gaussian component added to exponential decay of the classical flare model manages to reproduce the first and third bumps quite well. However, it overestimates and underestimates the second and fourth bumps, respectively. This suggests that adding a Gaussian to a classical flare model provides a better fit to the data for explaining the additional bumps, at least in comparison to using a classical flare model alone that did not converge into any reasonable solution. Nonetheless, it still does not fully capture all the

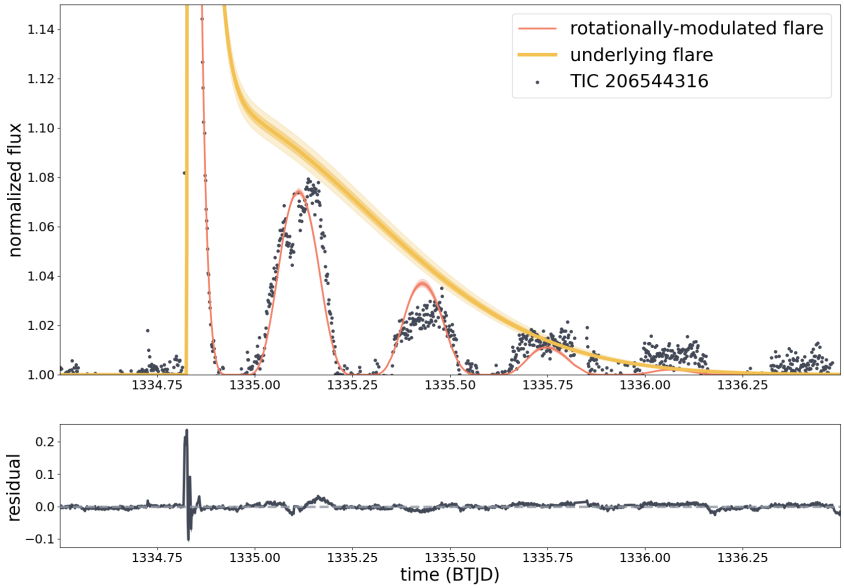


**Figure 5.11:** Sampling of best-fit results from the MCMC. The yellow line represents the underlying flare not modulated by the star's rotation, while the red line represents the rotationally-modulated flare. The shaded regions indicate the uncertainties in the fit: the lighter (more faded) region corresponds to the 2-$\sigma$ uncertainty, while the darker (more opaque) region corresponds to the 1-$\sigma$ uncertainty.

observed features, suggesting that better modeling of peak-bump flares is necessary.

From the underlying flare, I then calculated the bolometric energy of the flare, $E_{f,\mathrm{bol}}$, using the method described in Section 4.8. The results of the MCMC simulations, along with the parameters from the previous sections, are given in Table 5.3. The key highlight of this analysis is that the flare latitude $\theta_f$ derived from the MCMC simulations indicates a low-latitude flare:

$$\theta_f = 35.70^{+0.60}_{-0.63}\ ^\circ,$$

**which is excitingly low enough to interact with any material near the stellar equator!** The stellar inclination $i_*$ is also further constrained by taking into account data from the lightcurve. Notably, I found that the flare latitude $\theta_f$ from the MCMC simulation, based on a more comprehensive rotationally-modulated model that takes into account the entire shape of the lightcurve, closely match the value derived from the simpler night length method. This validates the result, as two independent methods return a similar outcome.

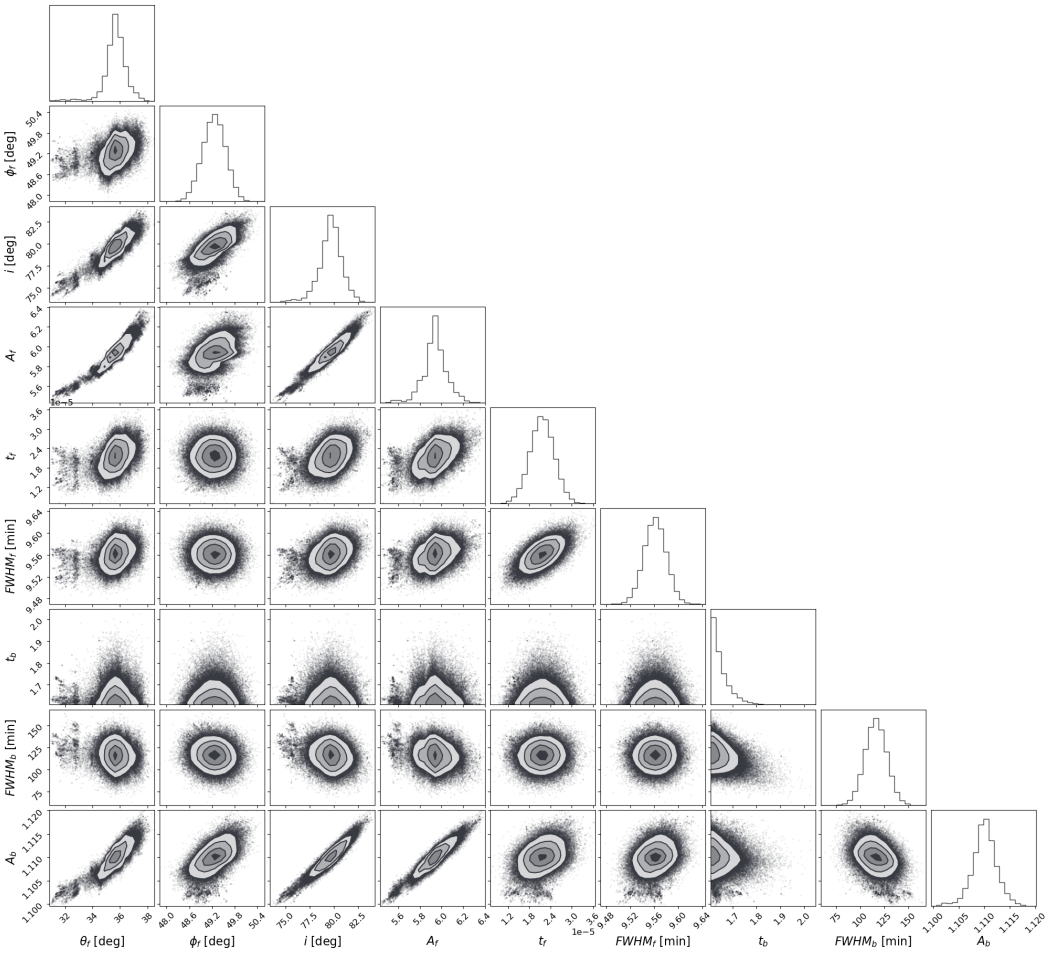


**Figure 5.12:** Posterior PDF of all involving parameters and the correlation between each parameters.

# 6 Discussion

## 6.1 Low-latitude superflare in a fast-rotating M dwarf

From the results in Section 5.5, I found a low-latitude flare on a fast-rotating M dwarf. This finding is interesting for two reasons. First, it is unexpected based on the current understanding of fast-rotating stars (Section 2.3.2). This is especially true given by the flare's high total energy of approximately $10^{36}$ erg, which lies at the upper end of the known energy distribution from M dwarf flares [Gün+20]. Second, the flare may be low enough to interact with any equatorial material that has been hypothesized as the source of the modulation seen in scallop-shell stars (Section 3.2). This section focuses on the former point, while the latter is discussed in Section 6.3.

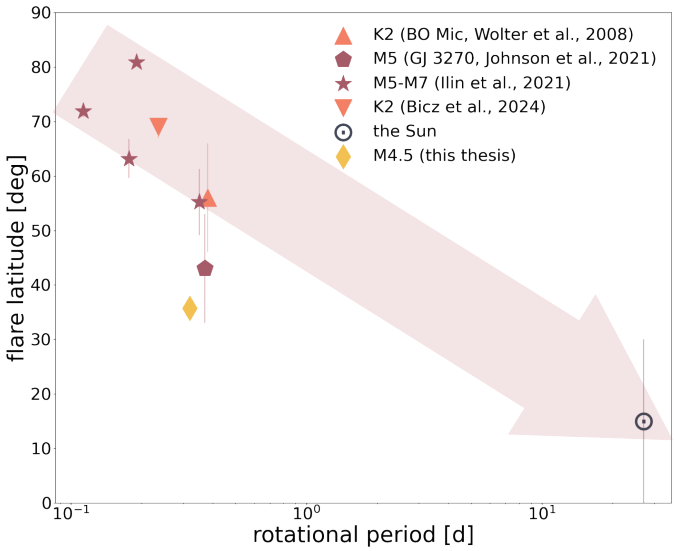


**Figure 6.1:** Updated plot of all localized flares as a function of their rotational period. This thesis adds a new data point, which strays away from the previously suggested possible connection between stellar flare latitudes and rotational period, represented by the pink arrow.

The low-latitude flare identified in this thesis adds to the small but growing sample of localized stellar flares. As shown in Figure 5.11, it has the lowest flare latitude in the current sample. This result is unexpected, especially given that TIC 206544316 is a fast-rotator. Rapidly-rotating stars are generally expected to generate high-latitude active regions (see Section 2.3.2), since strong Coriolis forces

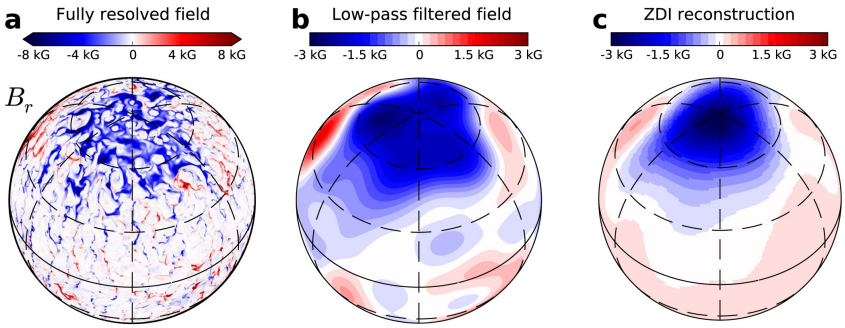


**Figure 6.2:** Simulations of the radial $B_r$ components of the magnetic field at the outer boundary of a fully-convective M dwarf (a), after applying a low-pass filter (b), and the magnetic field maps constructed by applying the ZDI technique with average $v \sin i_*$ of 20 km/s (c). From Yadav et al. [Yad+15].

are expected to deflect rising magnetic flux tubes that are formed at the base of the convection zone toward the poles. As a result, magnetically strong and complex active regions, those most likely to produce frequent and energetic flares, should be concentrated at high latitudes. Previous observations of localized flares on M dwarfs have generally supported this idea, but the flare I found in this thesis appears to challenge it.

However, it should be noted that this does not entirely rule out the presence of active regions near the stellar equator in fast-rotators. It simply suggests a *tendency* for more active regions to form near the poles. While ZDI of fast-rotators indeed often show polar spots, the technique may be biased against detecting equatorial features. Equatorial spots have been observed via exoplanet transits, even for fast-rotating stars (see Section 2.3.2). Simulations of magnetic fields in fully-convective M dwarfs, which are typically fast-rotators, 6.2 support this: equatorial active regions can indeed form even when they tend to cluster near the poles, but they may go undetected in ZDI reconstructions and tend to show weaker field strengths.

Nevertheless, the total energy derived of the flare here allows it to be classified as a superflare [Shi+13]. This raises a crucial question: **can flares of this magnitude be generated from low-latitude regions, where magnetic activity is generally weaker?**

To address this, I used the empirical relation between starspot sizes and flare energies. This is based on the idea that larger starspots host stronger magnetic fields. Stellar flares are sudden releases of magnetic energy stored in active regions. The magnetic energy within the active region, approximated by the spot size, can serve as an upper limit for the flare energy. This relation is well-observed in the Sun [see Shi+13, Figure 2 and references therein] and provides a way to estimate the magnetic energy and spot size required to produce the flare found in this thesis. Shibata et al. [Shi+13] proposed a scaling law between the flare energy upper limit and starspot size:

| $f$ | $A_{\rm spot}$ (area of solar hemisphere) |
|---|---|
| 0.1 | 17% |
| 0.5 | 6% |

**Table 6.1:** Approximated values of the starspot area based on Equation 6.2 in units of the solar hemisphere for $B = 2000$ G and $E_{f,\rm bol} \approx 6.4 \times 10^{36}$ erg.

$$E_{\rm flare} \approx f E_{\rm mag} \approx f \frac{B^2}{8\pi} A_{\rm spot}^{3/2} \tag{6.1}$$

$$\approx 7 \times 10^{32}\ {\rm erg} \left(\frac{f}{0.1}\right)\left(\frac{B}{10^3\ {\rm G}}\right)^2 \left(\frac{A_{\rm spot}/\left(2\pi R_\odot^2\right)}{0.001}\right)^{3/2}, \tag{6.2}$$

where $E_{\rm mag}$ is the magnetic energy stored in the active region, $f$ is the fraction of magnetic energy released during the flare, and $B$ is the magnetic field strength of the active region in Gauss. The flare energy ($E_{f,\rm bol}$) must be less than or equal to the magnetic energy in the region ($E_{\rm mag}$), with $f$ is typically assumed to be in the range of 0.1 to 0.5 [Her+21].

To estimate the required spot size, I assumed a magnetic field strength $B_{\rm spot}$ of 2 kG. I chose this value from observations of superflares on solar-type stars, which typically occur in regions with field strengths below 3 kG, with most of them showing field strengths around 2 kG [see Her+21; Not+19, Figure 3]. Similar values are also reported for K and M dwarfs [see Her+21, Figure 4]. Since the value of $f$ is also a key factor, I calculated the required spot area $A_{\rm spot}$ for both $f = 0.1$ and $f = 0.5$, using the derive flare energy of approximately $6.4 \times 10^{36}$ erg. The results, shown in Table 6.1, suggest that a starspot covering about 6-17% of the solar hemisphere would be needed to produce this flare.

The next step is to estimate whether such large starspots can exist at equatorial latitudes on fast-rotating stars. To investigate this, I looked up spot transits [Sil03] on two fast-rotating solar-type stars, Kepler-63 [NV20] and CoRoT-2 [Sil+10], both with rotation periods $P_{\rm rot} \sim 5$ days. I chose these stars because they are both solar-type, making them good test cases for studying Coriolis effects on stars that most likely generate magnetic flux tubes from the bottom of the convection zone. The spot parameters are listed in Table G.1. Calculating spot areas from their radii gives an average spot area of approximately 0.1% of the solar hemisphere. These values are one to two orders of magnitude smaller than the area required in Table 6.1. Even under the extreme assumption that all magnetic energy is released in a flare $f = 1$ for a spot with field strength of 3 kG, the minimum required spot size would still be around 2%. This suggests that, based on current observations, low-latitude starspots on fast-rotators lack the magnetic energy needed to produce a $10^{36}$ erg superflare.

There are three important caveats to this analysis:

**First, the comparison stars are solar-type stars expected to have solar-like dynamos**. On other hand, TIC 206544316 lies near the spectral transition between partially- and fully-convective M dwarfs, making it unclear whether it should follow solar-type magnetic behavior. If it does, an alternative mechanism is needed to generate the required magnetic energy for observed flare. One possibility is a flare-like outburst from magnetospheric accretion, which can resemble a flare depending on the accretion rate [Pau+18]. While some young M dwarfs still show signs of accreting disks (e.g., Peter Pan disks, see Section 3.2.2), TIC 206544316 shows no infrared excess and no accretion-related bursts in its modulation pattern (see burster stars in Section 3.1). This makes accretion an unlikely scenario, suggesting another mechanism must be responsible for the flare.

**Second, the empirical relation between starspot size and flare energy is based on the assumption that more energetic flares are produced by larger spots with stronger field strengths**. If this holds true for stars beyond the Sun, then superflares should occur more frequently at rotational phases corresponding to maximum spot coverage, i.e., lighcurve at minima. However, this correlation is not observed [e.g., Doy+19; DRD20; RV18]. Instead, superflares appear to occur randomly across the stellar surface. **Case in point: the superflare in this thesis.** It also occurred *exactly* on the maxima of the lightcurve (see Figure 5.8). This makes it harder to predict relationships between spot size and flare energy, or to predict where flares are likely to occur.

**Third, M dwarfs may not generate magnetic fields at the bottom of the convection zone, regardless whether they are partially- or fully-convective**. Due to their deep convection zones, M dwarfs may operate under a distributed dynamo, in which magnetic fields are generated throughout the convection zone [WD16]. In such cases, the locations of emerging active regions are not directly clear even with fast rotation. This could also help explain the result in Figure 6.1, where an M5-type star exhibits a flare at latitude $\theta_f \approx 43°$. While it is not extremely low, it is significantly lower than most other localized M dwarfs, especially for its rotation period.

Before I conclude this section, I think it is worth discussing the case of Kepler-63 [NV20]. The star is orbited by a giant planet on a near-polar orbit. The star itself has a low stellar inclination $i_*$, allowing spot transits to probe latitudes from 4° to 60°. Table G.1 shows only the low-latitude regions, but Kepler-63 shows an even distribution of spots across all latitudes (Figure G.1). It also shows a bimodal distribution with a notable lack of spot coverage at $\theta = 34°$. There is no significant difference in spot sizes between low- and high-latitude regions, which is also generally unexpected for a fast-rotating solar-type star. Netto and Valio [NV20] interpreted their results as an indication of different processes for the origin of the the low- and high-latitude spots. Note, however, that spot transits can only detect starspots smaller than the transiting planet. Larger spots may not be properly resolved in this system.

In summary, while a low-latitude superflare is unusual based on current understanding of stellar dynamos, it is certainly not impossible. This is mainly due

to our still-limited knowledge of how stellar dynamos work in stars other than the Sun. The finding of this thesis thus provides valuable constraints for stellar dynamo models and favors models, such as the distributed dynamo, that allow the emergence of active regions with sufficient magnetic energy to produce a $\approx 10^{36}$ erg flare at low latitudes.

## 6.2 A peak-bump flare

Not only that the star is a newly-classified group of young M dwarfs, the flare in this thesis, to my surprise, seems to be one as well. The underlying flare in Figure 5.11 shows that the flare has a large, highly impulsive peak followed by a second, more gradual Gaussian peak, or currently known as a peak-bump flare (Figure 2.6). Peak-bump flares are one of the variety of complex flare morphologies found in TESS observations, with 17% of complex flares showing this morphology [HM22].

While it may seem that the peak-bump morphology is a new phenomena, late-phase flares are in fact frequently detected in our Sun. They are typically observed in the extreme-UV (EUV) [e.g., Che+20b; Woo+11] and originate from the coronal loops. During the impulsive phase, the plasma in the loops are heated. The plasma take longer time to cool [Rea14], hence they are observed as a delayed secondary peak following the initial flare outburst. Note, however, that late-phase solar flares are not observed in white-light. This is because the source of the EUV late-phase is from optically-thin plasma. Solar white-light flares themselves are very difficult to obtain due to the bright background from the solar photospheric surface.

This naturally raises questions on the similarity of peak-bump flares and late-phase solar flares: **does the peak-bump morphology, observed in white-light, originate from the same process as the EUV late-phase solar flares?** Yang 6768 et al. [Yan+23] proposed that, instead of emission from the hot plasma on the loop contributing to the white-light emission, the emission comes from the condensation of the plasma. During the impulsive phase, the chromosphere is heated and triggers evaporation flow and increases the density in the corona loop. Then, as the plasma cools and condenses, it starts descending back the chromosphere, creating a phenomena called coronal rain [e.g., MK22; Scu+16]. Interestingly, in the case of fast-rotating stars, some of the condensed material may even collect into a mass reservoir near the co-rotation radius, called a slingshot prominence [DJ24; DJJ23]. Yang 6768 et al. [Yan+23] simulated that the free-bound emission from the cold, condensed optically-thin plasma can indeed produce the the peak-bump morphology observed in TESS broadband.

Another alternative to the origin of the peak-bump flare is perhaps a bit more intuitive: the photospheric backwarming. Heating does not happen only in the chromosphere and corona during the impulsive phase, it also happens in the photosphere (see Figure 2.2). It could be that the flare, with its $10^{36}$ erg energy, heats up the photospheric footpoints to such an extent that it takes a longer time for it too cool than those in the classical flare model. This is aligned with the assumption that

the white-light flare emission comes from the photosphere (see Section 2.3.1 and 4.7.2). A similar mechanism to the EUV late-phase solar flare, but in the photosphere instead of the optically-thin coronal loop. Because of M dwarf's low luminosity in the photosphere, the photospheric heating looks bright in white-light unlike in the case of our Sun. In such case, one would expect a trend of superflares showing peak-bump flares more of then than not. However, only around 42% of superflares ($E_{f,\mathrm{bol}} \geq 10^{32}$) are found to exhibit complex morphologies [HM22]. It is still unclear what specific conditions would allow and not allow a peak-bump morphology to surface.

Because the flare in this thesis is only observed in TESS, it is not possible to give any meaningful constraints on which explanation is favorable. Nevertheless, in the discussions that follow, I consider these possible scenarios where relevant.

## 6.3 Possible interaction with co-rotating material

Section 5.2 outlined the modulation change observed after the flare. An exciting consequence of identifying a low-latitude flare in this system is the possibility that the flare itself caused the modulation change, suggesting an interaction between the low-latitude flare and the equatorial material hypothesized to be responsible for the modulation. I believe there are two important clues that may help us understand what kind of interaction could have occurred, assuming such an interaction indeed took place.

**First, the modulation change corresponded to a dimming rather than a brightening**. This is counterintuitive and unexpected from a simple scenario of a flare hitting a cloud of material. If the flare interacted with the equatorial material, a brightening would be expected either because the material was dispersed or ejected from the system. However, this does not appear to be the case (Figure 6.3). Therefore, the scenarios discussed from here onward must result in more material coming between the star and the observer.

**Second, the flare has a peak-bump profile**. This clue is less direct and less constraining than the first. The origin of the peak-bump profile could be attributed to several scenarios (Section 6.2). Nevertheless, if an interaction scenario can also explain either the origin or consequence of the peak-bump profile, it is worth considering in the discussion.

### 6.3.1 Determining orbital distance

The first step in understanding what kind of interaction the flare might have with the co-rotating material is determining their locations. As seen in Section 5.2, there are three "dips" in the modulation pattern of TIC 206544316. In this section, I treat them as three "clumps" or "clouds" located at different parts of the rotational phase. Even if the material is in the form of a disk, I assume a scenario where a misaligned dust disk resembles more of a cloudy or clumpy disk. This section focuses on the

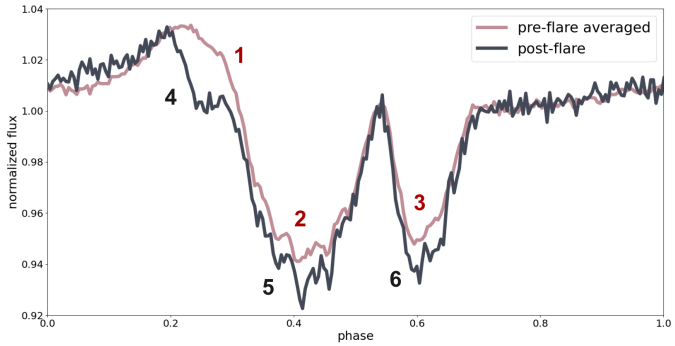


(a)

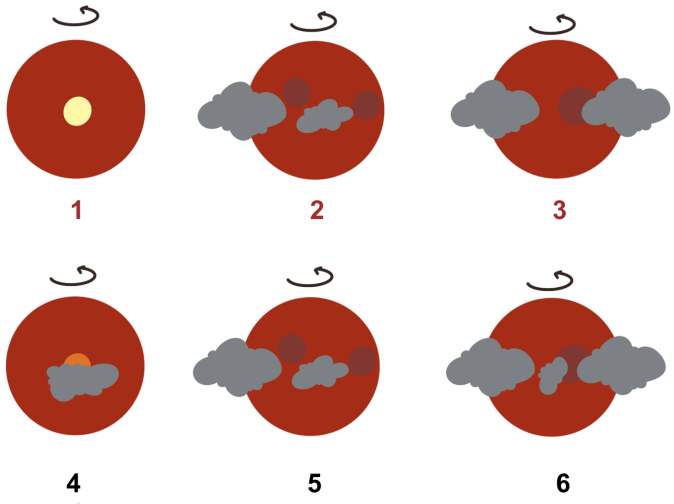


(b)

**Figure 6.3:** Observed modulation pattern and an illustration of what may be happening with the modulation pattern change. Panel (a): stellar disk with or without cloud that explains the dips in the modulation pattern before/during flare (1, 2, 3) and after flare (4, 5, 6). Panel (b): Simple sketch of the star on different rotational phase corresponding to the observed dips on the modulation pattern. Top: before/during flare. Bottom: after flare. Yellow circle marks the hot active region at the impulsive phase of the flare, while the orange circle represents the active region getting cooler at the gradual decay. Dark circles are spots. The main change happens on rotational phase $\phi \approx 0.2$ (1, 3). There is no cloud before or the flare happened because the rotational phase correspond to the maximum brightness of the modulation pattern. After the flare, there is a dimming and may be caused by a newly-added cloud between the observer and the star.

first dip $\phi \approx 0.2$, where the instantaneous dimming occurred.

Sanderson et al. [San+22] proposed a method to determine the orbital distance. This approach relies on the relationship between the duration of a transit and the orbital period. Let $T$ be the duration of the transit, determined from the FWHM of the transit dip. If $C$ is the circumference of the orbit, assuming a circular orbit with semi-major axis $a$, and $X$ is the portion of the orbit during which the transit occurs, then the following relation holds:

$$\frac{T}{P} \simeq \frac{X}{C} \simeq \frac{X}{2\pi a} \tag{6.3}$$

$$\frac{T}{P} \simeq \frac{2R_*}{2\pi a}, \tag{6.4}$$

for $X \approx 2R_*$. This then gives a relation between the duration of the transit and the orbital distance. However, this method of orbital distance determination only works for clumps or clouds that are small in radii. The depth of the dips gives a rough estimate of the radius of the cloud, which is given by:

$$\Delta F = \frac{A_{\text{cloud}}}{A_{\text{star}}} = \left(\frac{r_{\text{cloud}}}{R_*}\right)^2, \tag{6.5}$$

which can also be written as:

$$\frac{r_{\text{cloud}}}{R_*} = \sqrt{\Delta F}. \tag{6.6}$$

The first dip has a depth of $\approx 0.03$ from Table 5.1, which corresponds to $r_{\text{cloud}} \approx 0.17\,R_*$ from Equation 6.6. The cloud radius is too large for the assumption in Equation 6.4 to be valid. The ingress and egress of a cloud with such a radius must be taken into account. Therefore, the orbital distance of the cloud can no longer be determined using only the FWHM of the dip. An alternative method is required to determine the orbital distance.

To answer that, I adopted concepts from analysis of planetary transits. I followed the analysis by Seager and Mallen-Ornelas [SM03], which stated that the total duration of the transit, including ingress and egress, gives the orbital distance of the transiting body $a$ in terms of the stellar radius $R_*$:

$$t_T = \frac{P_{\text{rot}}}{\pi} \arcsin\left(\frac{R_*}{a}\left[\frac{[1 + (r_{\text{cloud}}/R_*)]^2 - \left[(a/R_* \cos i)^2\right]}{1 - \cos^2 i}\right]^{\frac{1}{2}}\right), \tag{6.7}$$

where $t_T$ is the total transit duration and $i$ is the orbital inclination. Assuming an orbital inclination $i = 90°$, then Equation 6.7 becomes:

$$t_T = \frac{P_{\text{rot}}}{\pi} \arcsin\left(\frac{R_*}{a}\left[1 + \frac{r_{\text{cloud}}}{R_*}\right]\right). \tag{6.8}$$

Substituting Equation 6.6 results in:

$$t_T = \frac{P}{\pi} \arcsin\left(\frac{R_*}{a}\left[1 + \sqrt{\Delta F}\right]\right), \tag{6.9}$$

$$\sin\left(\frac{t_T}{P_{\rm rot}}\pi\right) = \frac{R_*}{a}\left[1 + \sqrt{\Delta F}\right], \tag{6.10}$$

with the final form:

$$\frac{a}{R_*} = \frac{1 + \sqrt{\Delta F}}{\sin\left(\frac{t_T}{P_{\rm rot}}\pi\right)}. \tag{6.11}$$

I then substituted values of the first dip from Table 5.1, with total transit duration of $t_T \approx 0.12\,P_{\rm rot}$ and a depth of $\Delta F \approx 0.03$. According to Equation 6.11, the first dip has a distance of $a \approx 3\,R_*$, which corresponds to $d_{\rm cloud} \approx 2\,R_*$ from the stellar surface.

### 6.3.2 Material: dust

A co-rotating dust cloud is one of the favored hypotheses for scallop-shell stars. The cloud is thought to be confined by magnetic field (see Figure 3.10). Not only does a dust cloud eliminate the problem of having to explain the star having a possible misaligned dust disk until ~ 200 Myr, it also explains the observed color dependency and the opacity that causes the dips. However, there are a few key questions regarding the feasibility of this scenario and in I aim to address them in this section.

#### What is the dust temperature?

The first key question to this scenario is: **can the dust even survive near the stellar surface?** To give an approximation, I calculate the equilibrium temperature of a dust grain $T_d$ at its distance $d_{\rm cloud} \approx 2\,R_*$. Let the luminosity of the star, $L_{\rm star}$, be given by:

$$L_* = 4\pi R_*^2 \sigma T_{\rm eff}^4. \tag{6.12}$$

Then, let flux $F_d$ received by the dust grain at distance $d_{\rm cloud}$ be given by:

$$F_d = \frac{L_*}{4\pi d_{\rm cloud}^2}. \tag{6.13}$$

Because the dust is not a point source, I multiplied the flux with the cross-section of a dust grain, giving:

$$F_d = \frac{L_*}{4\pi d_{\rm cloud}^2} \times \pi r_d^2. \tag{6.14}$$

Assuming the dust grain acts like a blackbody, where it absorbs all incident

radiation and then re-emitting the, I can then combine Equations 6.12 and 6.14, which gives $T_d$ as:

$$L_d = F_d \tag{6.15}$$

$$4\pi r_d^2 \sigma T_d^4 = \frac{4\pi R_*^2 \sigma T_{\text{eff}}^4}{4\pi d_{\text{cloud}}^2} \times \pi r_d^2 \tag{6.16}$$

$$T_d = \left( \frac{R_*^2 \, T_{\text{eff}}^4}{4 \, d_{\text{cloud}}^2} \right)^{\frac{1}{4}} . \tag{6.17}$$

Substituting $T_{\text{eff}} = 3,100$ K and $R_* = 0.48, R_\odot$ from Table 5.3, gives $T_d = 1,550$ K.

The equilibrium dust temperature $T_d$ is certainly warm. However, it is not so hot that dust cannot survive at such a distance. Zhan et al. [Zha+19] calculated the sublimation times of different minerals composing the dust for different grain sizes (see their Figure 10). They found that a few minerals can indeed survive for more than a year at distances $d \leq 5\,R_*$ for typical scallop-shell stars, with maximum equilibrium temperatures around $T_d \approx 2,000$ K. In the case of this thesis, a dust cloud composed of minerals such as forsterite and corundum, in various grain sizes, can survive at $d_{\text{cloud}} \approx 2\,R_*$ from the stellar surface. These grains can be stable for around a year, which fits the stability requirement of scallop-shell star modulations.

However, the equilibrium dust temperature $T_d$ is valid if, and only if, the stellar photospheric radiation is the sole contributor to the luminosity. I believe this is not the case for many scallop-shell stars, especially for TIC 206544316. Like the Sun, magnetically active stars have hot coronae that emit X-rays at millions of Kelvin [see Güd04]. But unlike the Sun, the extent of these coronae is difficult to define in other stars. Flares, in turn, can offer some constraints.

Flare loop length is observed to correlate with the magnetic energy of its host active region [SY02]. Since flare energy also scales with magnetic field strength (see Section 6.1), flare energy can be used as an order of magnitude proxy for loop lengths [Mae+21; Rea+97]. Flares on M dwarfs have been shown to produce loop lengths of $L \approx 10^9 - 10^{10}$ cm [e.g., Ili+24a; Ram+21], with some M dwarf flares even showing loop lengths up to $L \approx 10^{11}$ cm [Kar+22]. If the flare in this thesis has a loop length at the higher end, which may well be the case given the high flare energy, then the flare might have a loop length of $\approx 10^{11}$ cm that corresponds to roughly $3\,R_*$. If that is not the case, then a more typical loop length in the range of $10^9 - 10^{10}$ cm would correspond to approximately $0.03 - 0.3\,R_*$.

The first dip indicates that there is a cloud of material located precisely at the rotational phase where the flare occurred. Because the material is assumed to be co-rotating, it can be inferred that the cloud is indeed located at the same position as the flare. The flare is also a low-latitude flare. This gives a simplified picture is that there is a giant loop around $\theta_f \approx 35°$ extending from the stellar surface to a specific loop length. Note again that $d_{\text{cloud}} \approx 2\,R_*$. If the loop length is $3\,R_*$, it is unlikely

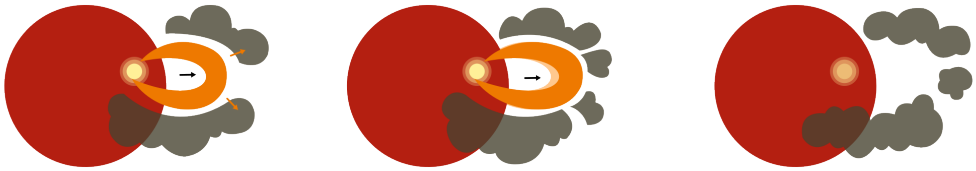

**Figure 6.4:** Simple illustration of a flare interacting with the surrounding material. After the impulsive phase, radiation pressure from the flare hits parts of the surrounding clouds (no cloud exists at the longitude where the flare occurred). However, the flare energy might only be enough to dislocate the clouds instead of ejecting/dispersing them. This then creates an additional dimming from added up material instead of brightening.

that the cloud is composed of dust, because this cloud of dust is possibly inside the stellar corona and is potentially exposed to temperatures of millions of Kelvin. No known dust should be able to survive such extreme conditions. However, if the loop length is instead in the range of $0.03 - 0.3\,R_*$, then it is much more plausible for the cloud to consist of dust, as it would not be subjected to such extreme temperatures.

### A confined dust grain vs the active star

Nonetheless, I believe it is worth discussing a scenario where a cloud of dust could survive near the flare site to see how the flare may interact with the surrounding material. I think the observed dimming (Section 5.2) can be explained by other forces from the flare, the following CME, and the stellar wind hitting parts of the nearby clouds (Figure 6.4). However, instead of completely ejecting the clouds, or evaporating them, the radiation pressure from the flare only has enough energy to dislocate the clouds. Hence creating an additional cloud on the line of sight between the observer and the flare (Section 6.3).

To see whether this scenario is plausible, I approximated the forces acting on a single dust grain at distance $d_{\text{cloud}}$. Here I only assumed a single grain because it simplifies the calculation in a situation with more unknowns than knowns. Sanderson et al. [San+22] proposed that dust grains can become confined by the star's magnetic field after being charged through collisions with the stellar corona. This occurs when the Lorentz force $F_L$ dominates over the gravitational force $F_G$, causing the dust to become trapped along magnetic field lines, but it is still able to move freely along them. Based on this, the two dominant forces acting on the grain are the Lorentz force and gravity. In this section, I break down the contribution of each at distance $d_{\text{cloud}}$ and compare them to the radiation pressure from the flare $F_{\text{rad}}$.

**First, the Lorentz force $F_L$.** I adopted the assumption from Sanderson et al. [San+22] that dust grains become charged by collisions with electrons and protons in the coronal plasma. They are thus assumed to acquire a negative charge. The resulting charge $q_d$ is calculated based on Ke et al. [KHL12]:

$$q_d = -\frac{30\pi\epsilon_0 r_d k_B T}{e}, \tag{6.18}$$

where $k_B$ is the Boltzmann constant, $\epsilon_0$ is the permittivity of free space, $e$ is the charge on one electron, $r_d$ is the radius of one dust grain, and $T$ is the plasma temperature.

For a dust grain confined in a dipole field with strength of $B$, the Lorentz force $F_L$ is given by:

$$F_L = q_d \, v_d \, B, \tag{6.19}$$

where $v_d$ is the velocity of the dust grain perpendicular to the magnetic field $B$. The magnetic field strength $B$ experienced by the dust grain scales with distance from the stellar surface and can be expressed as:

$$B = B_{\rm surf}\left(\frac{R_*}{d}\right)^3, \tag{6.20}$$

where $B_{\rm surf}$ is the surface magnetic field strength assumed to be responsible of confining the dust grain. Here I want to note that I am using $B_{\rm surf}$ for the surface field, not the large-scale dipole field. On the other hand, Equation 6.20 is the dipole equation. This practice follows the procedure from Sanderson et al. [San+22] where they compared surface field strength up to 5 kG. In reality, the large-scale dipole field, retrievable via ZDI measurements, is probably $10-20\%$ smaller [Koc+20; Rei+22]. Thus, Equation 6.20 can overestimate the actual magnetic field strength and may not probe the correct field.

For a dust grain moving towards the star, the velocity should be a fraction $f$ of the escape speed, given by:

$$v_d = f\, v_{\rm esc} = f\sqrt{\frac{2GM_{\rm star}}{d}}. \tag{6.21}$$

Finally, substituting Equation 6.18, 6.20, and 6.21 to 6.19 gives the Lorentz force experienced $F_L$ by the dust grain, expressed as:

$$F_L = -\frac{30\pi\epsilon_0 r_d k_B T}{e} f\sqrt{2GM_{\rm star}}\, B_{\rm surf}\, R_*^3\, d^{\frac{7}{2}}. \tag{6.22}$$

**Next, the gravitational force $F_G$.** I calculated the gravitational force $F_G$ experienced by one dust grain. Assuming that the dust grain is a sphere with density $\rho_d$, the gravitational force $F_G$ is defined as:

$$F_G = \frac{4\pi r_d^3 \rho_d}{3}\,\frac{GM_{\rm star}}{d^2}. \tag{6.23}$$

For a dust grain to be confined by the magnetic field and prevented from falling to the stellar surface, it must satisfy $F_L \geq F_G$.

| Parameter | Value | Source |
|---|---|---|
| Grain size $r_d$ | 1 $\mu$m | Sanderson et al. [San+22] |
| Density $\rho_d$ | 3,000 kg/m$^3$ | Zhan et al. [Zha+19] |
| Surface magnetic field strength $B_{\text{surf}}$ | 4 kG | Shulyak et al. [Shu+19] |
| Distance of dust $d_d$ | 2 $R_*$ | Section 6.3.1 |
| Coronal temperature $T$ | 5.7 MK | Jardine and Collier Cameron [JC19] |
| $f$ | 0.1 | Used in this thesis |

**Table 6.2:** Parameters of the dust grain used in this analysis.

The dust parameters used in the calculation are listed in Table 6.2. I adopted the surface magnetic field strength $B_{\text{surf}}$ from Shulyak et al. [Shu+19] for stars with rotation periods around $P_{\text{rot}} \sim 0.3$ days. The value listed here is the average magnetic field and the local field strengths can go beyond or lower than that by a factor of two. However, for an order-of-magnitude estimate, I think the average values provides a reasonable approximation of typical conditions. The dust density $\rho_d$ is taken from Zhan et al. [Zha+19], which is also the value used by Sanderson et al. [San+22]. The coronal temperature is based the fast-rotating star V374 Peg from Jardine and Collier Cameron [JC19]. Its fast-rotation of $P_{\text{rot}} = 0.45$ days should be representative of an M dwarf in the saturated regime like TIC 206544316.

I want to note that the choice of the velocity scaling factor $f$, and therefore the dust velocity $v_d$, is probably the most uncertain part of the calculation. Sanderson et al. [San+22] used $v_d$ to compute the Lorentz force $F_L$ acting on a moving dust grain before it becomes magnetically confined. It was used to examine whether magnetic confinement is possible. If confinement is possible, they argued that drag from the coronal plasma slows particles to a "stopping distance," representing stable points. In contrast, I want to see what is the Lorentz force $F_L$ experienced by a dust grain that is already in these stable points, where movement against the magnetic field is minimal. To represent this, I decided to adopt an arbitrary small value of $f = 0.1$, which should be low enough to approximate a grain at a stable point, while still allowing limited motion along magnetic field lines.

Substituting the dust and stellar parameters in Table 6.2 and 5.3, respectively, I obtained the Lorentz force experienced by one dust grain as $F_L \approx 10^{-10}$ N with gravitational force $F_G \approx 10^{-13}$ N. Additionally, I calculated $B = 0.15 B_{\text{surf}}$ to consider the large-scale dipole field assuming that Equation 6.20 overestimate the field strength. This returns $F_L \approx 10^{-11}$ N. This order of magnitude calculation confirmed that the strong magnetic field of the star should be able to confine the a dust grain magnetically against the gravitational force $F_L > F_G$, regardless if it is calculated with surface field strength or large-scale dipole field. I use both values of $F_L$ as lower and upper limit.

Next, I calculated the forces that might have an influence to the confined dust grain. Here I calculated three forces from three pressures: the radiation pressure of the flare $F_{\text{rad}}$, the dynamic presure from the stellar wind $F_{\text{wind}}$, and the dynamic

pressure from a CME $F_{\rm CME}$ from the $10^{36}$ flare, assuming that the flare is followed by a CME.

**First, the pressure from the radiation pressure of the flare $F_{\rm rad}$.** To estimate the radiation pressure, I calculated the flare luminosity at the maximum flux $L_{f,\rm max}$ using the method in Section 4.8, which gives me $L_{f,\rm max} \approx 10^{32}$ erg/s. I then calculated the flux received by the dust grain from the flare at its distance by substituting $F_{f,\rm max}$ to Equation 6.13. In Section 6.3.1, I assumed that the dust absorbs all incident radiation. However, to see how the effect of the radiation pressure $P_{\rm rad}$ on the dust, here I assumed that the dust grain *reflects* all incident radiation. Their results should differ by a factor two. Let the radiation pressure $P_{\rm rad}$ be expressed by:

$$P_{\rm rad} = \frac{2\,F_d}{c}. \tag{6.24}$$

The force experienced by the dust can thus be written as:

$$F_{\rm rad} = P_{\rm rad} \times \pi r_d^2 \tag{6.25}$$

$$= \frac{2L_{\rm star}}{4\pi d_{\rm cloud}^2\, c} \times \pi r_d^2. \tag{6.26}$$

Substituting $L_{f,\rm max}$ and values from Table 6.2 returns $F_{\rm rad} \approx 10^{-14}$ N as the force from the radiation pressure $P_{\rm rad}$ experienced for one dust grain at distance $d_{\rm cloud}$.

**Second, the force from the dynamic pressure of the stellar wind $F_{\rm wind}$.** This is challenging to estimate because stellar wind from cool stars can only be measured indirectly [see Vid21; Woo04]. However, the close distance of the dust cloud itself suggests that it may lie within a region where the wind has not yet accelerated, i.e., the sub-Alfvénic regime. To evaluate this, I calculated the average Alfvén surface radius $\overline{AS_R}$ using the average surface radial magnetic field $B_R^{\rm avg}$ obtained from ZDI. I adopted the scaling-law from Chebly et al. [Che+23]:

$$\log \overline{AS_R} = (0.42 \pm 0.06) \log B_R^{\rm avg} + (0.71 \pm 0.07), \tag{6.27}$$

which returns $\overline{AS_R}$ in units of the stellar radius $R_*$. Note that I only have the average surface magnetic field strength $B_{\rm surf}$, which is not directly equivalent to the radial component derived from ZDI. I followed the approach and assumptions in Ilin et al. [Ili+24b] to convert $B_{\rm surf}$ to $B_R^{\rm avg}$. This is also based on the assumption that ZDI measurements return roughly $10-20\%$ of the total surface field strength. Therefore, as an upper limit, I used $B_R^{\rm avg} \approx 0.15 B_{\rm surf}$ in Equation 6.27. This gives me:

$$\overline{AS_R} = 57.54 \pm 1.66\, R_*,$$

which suggests that the dust cloud lies within the sub-Alfvénic regime, where the stellar corona has not yet transitioned into stellar wind. As a result, the cloud interacts with a relatively stationary coronal environment. Naturally, because TIC 206544316 does not have any ZDI measurements, the conversion from

$B_R^{\text{avg}} \approx 0.15 B_{\text{surf}}$ might not be correct. However, comparing TIC 206544316 to low-mass stars with similar activity from $P_{\text{rot}}$ and spectral class that do have ZDI measurements, all of them suggest the $\overline{AS_R}$ to be in the order of tens of stellar radii [Che+23].

Even though the corona might be stationary, this does not mean that I cannot estimate the effect of the "stellar wind". Since the dust cloud is moving through this nearly stationary medium, I can compute the dynamic pressure $P_{\text{dyn,wind}}$ based on the relative velocity of the stationary corona impacting the moving cloud. To do this, I first calculated the velocity of the cloud, $v_{\text{cloud}}$, relative to a stationary reference frame. Using $P_{\text{rot}}$ and $r_{\text{cloud}}$, I found the cloud to be moving at:

$$v_{\text{cloud}} = 151.79\,\text{km/s}.$$

This is therefore the relative velocity of the corona in the rest frame of the dust cloud, so that $v_{\text{wind}} = v_{\text{cloud}}$. Note that this value is an upper limit because I assumed that the corona is completely stationary, i.e., $v = 0$ km/s, in the stellar rest frame. In reality, the corona might also be moving at a certain speed in the stellar rest frame, even though it remains in the sub-Alfvénic regime. Additionally, if the corona is moving at the escape velocity $v_{\text{esc}}$ at $r_{\text{cloud}}$, which is $v_{\text{esc}} \approx 300$ km/s, then the relative velocity experienced by the cloud is also $v_{\text{wind}} \approx 150$ km/s.

Next, I estimated the local coronal density at the $r_{\text{cloud}}$ assuming a radial decay of $\rho \propto r^{-2}$ [see Vid21]. At the base of the corona, I adopted a typical value of $\rho_* = 2 \times 10^{10}\,\text{cm}^{-3}$. which is often used for the Sun [Sok+13] and other cool stars [Alv+20; Ili+24b]. Assuming this $\rho_*$ is measured at $R_*$, the density at $r_{\text{cloud}}$ becomes:

$$\rho_{*,r_{\text{cloud}}} = 5 \times 10^{9}\,\text{cm}^{-3}.$$

Assuming a fully ionized hydrogen plasma, this corresponds to a mass density of:

$$\rho_{\text{wind}} = 8.36 \times 10^{-12}\,\text{kg/m}^3,$$

using only the proton mass $m_p$ to simplify the calculation.

With Equation 6.3.2, I can then calculate the dynamic pressure $P_{\text{dyn}}$, defined as:

$$P_{\text{dyn}} = \frac{1}{2}\rho v^2. \tag{6.28}$$

Finally, the force experienced by one dust grain from the dynamic pressure of the solar wind $F_{\text{wind}}$ can be obtained by multiplying the dust grain's cross-section similar to Equation 6.25. This is given by:

$$F_{\text{wind}} = P_{\text{dyn,wind}} \times \pi r_d^2 \tag{6.29}$$

$$= \frac{1}{2}\rho_{\text{wind}} v_{\text{wind}}^2 \times \pi r_d^2 \tag{6.30}$$

Substituting $\rho_{\rm wind}$ and $v_{\rm wind}$ to Equation 6.28, and using $r_d$ from Table 6.2, I obtained $F_{\rm wind} \approx 10^{-13}$ N.

**Lastly, the force from the dynamic pressure of a CME $F_{\rm CME}$.** As with the stellar wind case, calculating $F_{\rm CME}$ requires both the speed of the CME, $v_{\rm CME}$, and the mass density of the ejected plasma, $\rho_{\rm CME}$. Like stellar winds, CMEs from stars other than the Sun have not been observed directly, but there have been a number of efforts to constrain their properties indirectly [see e.g., Mos+19; OW17]. In this case, I assumed that the CME originated from the same reconnection event as the flare. In the Sun, not all flares are followed by CMEs [e.g., Yas+06] and some CMEs occur without flares [e.g., HH13]. However, for this discussion, the modulation change observed after the flare supports the assumption of a flare-associated CME.

Unfortunately, the dataset that I have does not allow me to calculate the speed of impact to the surrounding material. From the TESS lightcurve, the change in the modulation can be definitely seen after four cycles. By a simple calculation of $d_d$ and $t = 4\,P_{\rm rot}$, I get the lower speed limit of $v_{\rm CME} = 5$ km/s, which does not give any meaningful constraints. As a result, I used the empirical flare-CME relation from Notsu et al. [Not+19] to constrain $v_{\rm CME}$. This speed of CME in their studies were derived from the blueshift of Balmer lines that are followed after a flare, which was interpreted as the moving plasmoid toward the observer.

Notsu et al. [Not+24] proposed a scaling-law of:

$$v_{\rm CME} \propto E_{f,\rm bol}^{1/6}. \tag{6.31}$$

However, even the strongest flare in their dataset $\sim 10^{36}$ erg did not appear to follow this relation. As a result, I adopted a value of:

$$v_{\rm CME} = 1,000\,\text{km/s}.$$

which is typical for CME speed in low-mass stars as measured from Balmer line blueshifts [sese Mos+19, and references therein].

For the mass density, CME mass derivation typically assumed values of $n_H \approx 10^{11}$ cm$^{-3}$ [see Mos+19, and references therein]. Using the mass of hydrogen atom $m_H$, I can then obtain:

$$\rho_{\rm CME} = 1.67 \times 10^{-10}\,\text{kg/m}^3.$$

Finally, substituting $v_{\rm CME}$ and $\rho_{\rm CME}$ into Equation 6.30, I obtained the dynamic pressure force from the CME $F_{\rm CME} \approx 10^{-10}$ N. The forces are summarized in Table 6.3.

From the calculated forces, it can be seen that $F_L \approx F_{\rm CME} > F_G \approx F_{\rm wind} > F_{\rm rad}$. The Lorentz force $F_L$ mostly dominates over other forces, with $F_{\rm CME}$ being its only contender. In the case that the large-field dipole is used, then it is $F_{\rm CME} > F_L >$

| Force | Value |
|---|---|
| Lorentz force $F_L$ | $10^{-11} - 10^{-10}$ N |
| Gravitational force $F_G$ | $10^{-13}$ N |
| Force from radiation pressure $F_{\text{rad}}$ | $10^{-14}$ N |
| Force from dynamical pressure of wind $F_{\text{wind}}$ | $10^{-13}$ N |
| Force from dynamic pressure of CME $F_{\text{CME}}$ | $10^{-10}$ N |

**Table 6.3:** All acting forces on a dust grain at distance $d_{\text{cloud}}$ from the stellar surface.

$F_G \approx F_{\text{wind}} > F_{\text{rad}}$. Here I discuss the forces one by one.

**First, $F_{\text{rad}}$.** I found that the radiation pressure $F_{\text{rad}}$ is four orders of magnitude lower than the Lorentz force $F_L$ and one order of magnitude lower than the gravitational force $F_G$. This means that radiation pressure from the flare alone does not have enough energy to eject nor disperse the surrounding material if they are made by dust. While this makes senses to not have any material being ejected from the system, it is still unclear if the radiation pressure should have enough energy to shuffle or dislocate some material to cause the dimming.

An explanation for this insufficient impact is that the radiation pressure from the flare is underestimated around an order of magnitude. The flare in this analysis is assumed to have a blackbody temperature of $T = 10,000$ K. Flares, however, have been observed to show higher temperatures.The hottest observed to date is $T = 42,000$ K [How+20]. In the scenario that the flare in this thesis is also one of the flares that can reach such high temperatures, then substituting a $T = 40,000$ to the flare luminosity would result in the radiation pressure to be in the same order magnitude of the gravitational force. Perhaps then it has enough energy to be shuffled around while still being magnetically trapped.

**Second, $F_{\text{wind}}$.** I found that the force from the dynamic pressure of the stellar wind, $F_{\text{wind}}$, is on the same order of magnitude as the gravitational force $F_G$, but remains three order of magnitude lower than the Lorentz force $F_L$. This suggests that, even if the dust grain experiences pressure from the stellar wind due to its motion against the stationary corona, the resulting dynamic pressure is insufficient to overcome the strong magnetic force and eject the dust cloud. Because it is in the same order of magnitude with $F_G$, $F_{\text{wind}}$ can, in principal, shuffle the material around while it still being magnetically trapped.

However, because $F_{\text{wind}}$ is calculated under the assumption of a stationary corona, it does not fully explain the observed sudden dimming. If the dimming were caused by dynamic pressure from the stellar wind shuffling the material, given that $F_{\text{wind}}$ is comparable to gravity, then it raises the question of why this effect only appears at that specific time, following the flare. Unlike $F_{\text{rad}}$ and $F_{\text{CME}}$, the stellar wind be give a continuous force. Therefore, $F_{\text{wind}}$ may not be responsible for the sudden dimming but could contribute to the more gradual decrease seen in the third bump

(see Figure 6.3).

**Lastly, $F_{\mathrm{CME}}$.** I found that the force from the dynamic pressure of the CME, $F_{\mathrm{CME}}$, is the only one capable of significantly redistributing or even ejecting the material completely. However, there are two important caveats to this interpretation.

First, the strong magnetic field of TIC 206544316, typical of active M dwarfs, may actually prevent CME eruptions. Even if a CME does occur, its speed and kinetic energy might be significantly suppressed [Alv+18; Alv+19; Fra+19; Fra+22]. For the CME to generate a force comparable to the Lorentz force, i.e., $F_{\mathrm{CME}} \approx F_L$, it must reach a speed of at least $v_{\mathrm{CME}} > 250$ km/s for the lower limit and $v_{\mathrm{CME}} > 500$ for the upper limit. In this scenario, the CME would have to overcome the star's strong magnetic field to achieve such a velocity. Fortunately, the CME speeds compiled by Moschou et al. [Mos+19] for low-mass stars generally surpass this threshold, suggesting it is indeed plausible.

The second caveat is that, if CMEs from M dwarfs behave similarly to solar CMEs, then the CME speed could be excessively high for flares of this energy. For the lower limit, the CME already has enough force to fully eject the material rather than merely reshuffle or dislocate it. For the upper limit, $v_{\mathrm{CME}} > 2,000$ km/s is needed to have $F_{\mathrm{CME}}$ on the order of $10^{-9}$ N. Such high speeds have been observed in the Sun [see e.g., GMY19], and a moving plasmoid with $v \approx 5,000$ km/s has even been reported on the M dwarf AD Leo [HFR90]. In cases where the CMEs have forces that should eject the material from the system, the CME may not have been ejected radially. Instead, it might have had a different orientation relative to the stellar equator [see Xu+24]. A CME impacting the dust cloud at an angle may apply just enough force to shuffle the material without fully ejecting it, potentially explaining the observed dimming rather.

As shown so far, this analysis depends upon the idea that the strong magnetic field of fast-rotating scallop-shell star is sufficient to confine a dust grain magnetically. This is demonstrated by how the Lorentz force $F_L$ practically dominates over any other forces. However, there is still a big caveat of this analysis: **how does the dust grain get charged in the first place?**

While Sanderson et al. [San+22] proposed a case where the charging of the dust happens because of collisions with coronal plasma. However, I believe this scenario makes it even more complicated because it does not explain how any dust grain could survive in an environment with millions of Kelvin, especially if the coronal plasma is a prerequisite of it being charged. Stellar wind, on the other hand, can also charge dust grains via collisions. Yet, the location of the dust cloud appears to be within the sub-Alfvénic regime, where the wind may not have accelerated sufficiently. In that case, stellar wind could only be a viable charging mechanism if the dust grain had previously been located at a larger radial distance, far enough for the wind to reach the necessary speed.

Another possible scenario that does not require any additional forces is the

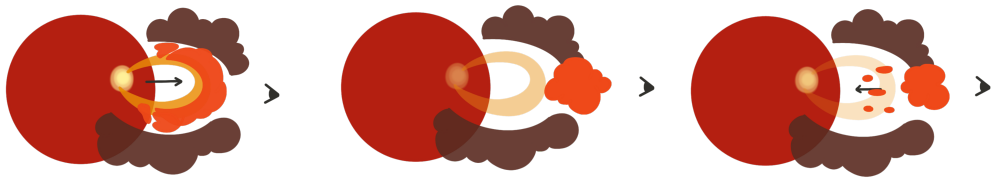

**Figure 6.5:** Simple illustration of a flare interacting with a cloud of gas. After the reconnection event, there is a blob of erupting plasomid ejected from the flare site. Instead of being ejected from the system, similar to an associated-CME, the blob of plasmoid is trapped by the magnetic field lines. The Lorentz force $F_L$ might be enough trapped the plasmoid because its kinetic energy is supressed by the strong magnetic field of the flare site. Some of the material might fall as coronal rain (the peak-bump profile) while some continue being trapped (the dimming).

reconfiguration of magnetic field lines after a flare. The reconnection that triggers a flare typically reconfigures not only the main loop but also the surrounding loops. It is possible that smaller dust clouds were trapped along the magnetic field lines (see Figure 3.10), but individually, they did not produce a noticeable dip. When the giant flare occurred, the reconfiguration of some magnetic field lines may have combined several smaller bumps into one larger, detectable bump. This can also simply be the material moving around the magnetic field line, as this possibility is noted in the previous section calculating $F_L$. In any case, many potential scenarios are possible given the limited data available. Therefore, the guesses presented in this section are essentially no better than the reader's own.

### 6.3.3 Material: gas

The other hypothesis besides a cloud of dust is a cloud of gas. The main caveat to this hypothesis is the origin of the opacity. A cloud of gas should be optically thin, and it is not directly clear how any cloud of gas would exhibit enough opacity to block parts of the stellar surface and create the observed dips. If the plasma or gas is ionized, which is a reasonable estimate if the material is within the stellar corona, then it does not need additional mechanism to why they can be magnetically trapped.

In this section, I propose a scenario on where the flare is followed by a CME or at least a plasmoid eruption that is associated with the flare (Figure 6.5). However, instead of it being ejected from the system, the material is trapped by the magnetic field lines, which supports the idea that CMEs may be confined by the star's strong magnetic field [Alv+18; Alv+19; Fra+19; Fra+22]. While the heated plasma from the reconnection cools down, some may fall as coronal rain, which give the peak-bump profile (Section 6.2), while some continue being trapped and cause the dimming.

An alternative scenario is that the erupting plasmoid contributed material into in an existing giant prominence [e.g., DJ24; Fer00; JC19; Wau+21], which is also suggested by Bouma et al. [Bou+24] as an alternative to the cloud of dust hypothesis. However, both scenarios depend upon the idea that these hot chromospheric

plasma, who should be optically thin, becomes optically thick **in the white-light broadband** at one point.

For such a scenario to occur, the cloud of gas must contain enough "absorbers" to create a detectable dip in TESS' red passband, ranging $6,000–10,000$, Å. This means the gas to be dense. Continuum opacity in this passband can come from two processes. First, bound-free absorption by the $H^-$ ion, i.e., a neutral hydrogen atom that has captured an electron. Bound-free absorption of $H^-$ can generate opacity for $\lambda \leq 16,400$, Å, since any photon with a shorter wavelength can photoionize the ion. In fact, this is the main process that contribute to continuum opacity in low-mass stars. Second, opacity can result from excitation of second-excited neutral hydrogen (n=3) for photons with $\lambda \leq 8204$, Å. Two problems for this scenario. First, if the gas has similar temperature to prominences, approximately $T \approx 8,000$ K, then $H^-$ ions are rare at such temperatures. In fact, for F-type stars and hotter, opacity is no longer dominated by bound-free absorption of $H^-$. Second that if the opacity is instead due to second-excited hydrogen, it is unclear whether enough of it would exist at this temperature to cause significant absorption.

## 6.4 Source of material?

Up until this point, it is clear that there are more questions than answer, both on the peak-bump flare or the nature of the equatorial material causing the scallop-shell phenomena. However, there is an even more interesting question that concludes this thesis' discussion: **what can be the source of the equatorial material of scallop-shell star?**

Answering this question is, of course, not an easy feat. Especially when it is far from clear *what* the material is even made of. If the material is dust, then perhaps the potential sources include evaporating planets [Gai+24] and debris from destroyed planetesimals [San+22]. If it's gas, other than the star itself from flares contributing the material, it may be nearby outgassing planet or rock. Hints of possible auroral emission in a radio-bright scallop-shell star [Kau+24] suggest that the material source might involve a Jupiter-Io-like configuration. Or it can also simply be debris disk swept away by the condensed plasma of slingshot prominences [DJ24] at large radii, making a gas-dust hybrid.

The answer is: at this point, no one knows. And that's exactly the point, there is a clear knowledge gap in our understanding of the evolution of young star-planet systems involving M dwarfs. This mystery has continued since the first discovery of scallop-shell stars in 2017, and I believe multi-wavelength observation campaigns can make significant progress. The takeaway from this discussion is simple: as more questions require answer, it's not time to hang up the detective hat, at least not yet.

# 7 Conclusions & Outlook

In this thesis, I studied TIC 206544316, a scallop-shell star observed with TESS that showed a long-duration giant flare modulated by the star's rotation. Following this flare, a permanent change in the modulation pattern suggested a possible interaction between the flare and surrounding material. The goal of this thesis is to localize the flare and evaluate whether and how it could interact with the surrounding environment. To achieve this, I did the following:

First, I constrained the stellar rotation period $P_{\rm rot}$ using MCMC and a modulation template derived directly from the lightcurve. I showed that periodograms enforcing sine functions provide only work as a first-order approximation for complex modulations.

Second, I derived the stellar inclination $i_*$ from the projected rotational velocity $v \sin i_*$ using Gaia RVS, CARMENES, and MIKE spectra, confirming TIC 206544316 as a fast-rotator, with $v \sin i_* = 68.12 \pm 3.77$ km/s, and a near edge-on configuration $i_* = 79.72^{\circ}_{(-1.02)}^{(+1.12)}$.

Third, I found a low-latitude superflare flare of $\theta_f = 35.70^{\circ}_{(-0.63)}^{(+0.60)}$ and $E_{f,\rm bol} \approx 10^{36}$ erg using the night length and flare modulation model with MCMC. This low-latitude flare is unusual for fast-rotators, especially for its energy. This finding supports dynamo models allowing magnetically-strong, low-latitude active regions even with fast-rotation. I also found that the flare shows a "peak-bump" flare profile, possibly due to coronal rain or photospheric backwarming.

Lastly, I analyzed the post-flare modulation change and found a dimming. This suggests that there is additional material added along the line of sight instead of material being ejected from the system. If the material is a magnetically-trapped dust, radiation pressure from the flare alone could not shuffle or dislocate the material around to cause the dimming, while dynamic pressure from a stellar wind or CME is a more plausible driver. If the material is gas, a trapped CME or flare-induced prominence formation could contribute the additional material, although the source of the broadband opacity required to produce a $\geq 3\%$ dip remains unclear.

In conclusion, I found the flare was low-latitude and capable of interacting with equatorial material. This work highlights the potential of flares as probes of the environments around young, planet-hosting M dwarfs and provides constraints on stellar dynamo models for fast-rotating stars. This thesis is also a call for more multi-wavelength observation campaign for scallop-shell stars. A project on investigating the properties of a giant prominence to cause the change in the modulation pattern is, at the time of this writing, being prepared.

# Bibliography


[ABL05] F. C. Adams, P. Bodenheimer, and G. Laughlin. **M dwarfs: planet formation and long term evolution**. *Astronomische Nachrichten* 326 (Dec. 2005). 913–919. DOI: 10.1002/asna.200510440.

[Alv+18] Julián D. Alvarado-Gómez et al. **Suppression of Coronal Mass Ejections in Active Stars by an Overlying Large-scale Magnetic Field: A Numerical Study**. *The Astrophysical Journal* 862 (Aug. 2018). 93. DOI: 10.3847/1538-4357/aacb7f.

[Alv+19] Julián D. Alvarado-Gómez et al. **Coronal Response to Magnetically Suppressed CME Events in M-dwarf Stars**. *The Astrophysical Journal* 884 (Oct. 2019). L13. DOI: 10.3847/2041-8213/ab44d0.

[Alv+20] Julián D. Alvarado-Gómez et al. **Tuning the Exospace Weather Radio for Stellar Coronal Mass Ejections**. *The Astrophysical Journal* 895:1 (May 2020). 47. DOI: 10.3847/1538-4357/ab88a3.

[AM21] Dimitra Atri and Shane R. Carberry Mogan. **Stellar flares versus luminosity: XUV-induced atmospheric escape and planetary habitability**. *Monthly Notices of the Royal Astronomical Society* 500 (Jan. 2021). L1–L5. DOI: 10.1093/mnrasl/slaa166.

[Bar+17] J. R. Barnes et al. **Surprisingly different star-spot distributions on the near equal-mass equal-rotation-rate stars in the M dwarf binary GJ 65 AB**. en. *Monthly Notices of the Royal Astronomical Society* 471:1 (Oct. 2017). 811–823. DOI: 10.1093/mnras/stx1482.

[Bar03] Sydney A. Barnes. **On the Rotational Evolution of Solar- and Late-Type Stars, Its Magnetic Origins, and the Possibility of Stellar Gyrochronology**. *The Astrophysical Journal* 586 (Mar. 2003). 464–479. DOI: 10.1086/367639.

[Bel+23] S. Bellotti et al. **The space weather around the exoplanet GJ 436b: I. The large-scale stellar magnetic field**. *Astronomy & Astrophysics* 676 (Aug. 2023). A139. DOI: 10.1051/0004-6361/202346675.

[Ben17] Arnold O. Benz. **Flare Observations**. en. *Living Reviews in Solar Physics* 14:1 (Dec. 2017). 2. DOI: 10.1007/s41116-016-0004-3.

[Ber+03] Rebecca Bernstein et al. **MIKE: A Double Echelle Spectrograph for the Magellan Telescopes at Las Campanas Observatory**. In: ed. by Masanori Iye and Alan F. M. Moorwood. Waikoloa, Hawai'i, United States, Mar. 2003, 1694. DOI: 10.1117/12.461502.

[BG10] Arnold O. Benz and Manuel Güdel. **Physical Processes in Magnetically Driven Flares on the Sun, Stars, and Young Stellar Objects**. *Annual Review of Astronomy and Astrophysics* 48 (Sept. 2010). 241–287. DOI: 10.1146/annurev-astro-082708-101757.

[Boc+10] John J. Bochanski et al. **THE LUMINOSITY AND MASS FUNCTIONS OF LOW-MASS STARS IN THE GALACTIC DISK. II. THE FIELD**. *The Astronomical Journal* 139:6 (June 2010). 2679–2699. DOI: 10.1088/0004-6256/139/6/2679.

[Bor+10] William J. Borucki et al. **Kepler Planet-Detection Mission: Introduction and First Results**. *Science* 327 (Feb. 2010). 977. DOI: 10.1126/science.1185402.

[Bou+20] L. G. Bouma et al. **PTFO 8-8695: Two Stars, Two Signals, No Planet**. *The Astronomical Journal* 160 (Aug. 2020). 86. DOI: 10.3847/1538-3881/ab9e73.

[Bou+24] Luke G. Bouma et al. **Transient Corotating Clumps around Adolescent Low-mass Stars from Four Years of TESS**. *The Astronomical Journal* 167:1 (Jan. 2024). 38. DOI: 10.3847/1538-3881/ad0c4c.

[Bow+23] Brendan P. Bowler et al. **Rotation Periods, Inclinations, and Obliquities of Cool Stars Hosting Directly Imaged Substellar Companions: Spin–Orbit Misalignments Are Common**. *The Astronomical Journal* 165:4 (Apr. 2023). 164. DOI: 10.3847/1538-3881/acbd34.

[Bus+07] I. Busà et al. **The Ca II infrared triplet as a stellar activity diagnostic: II. Test and calibration with high resolution observations**. *Astronomy & Astrophysics* 466:3 (May 2007). 1089–1098. DOI: 10.1051/0004-6361:20065588.

[Car63] Richard Christopher Carrington. **Observations of the spots on the Sun: from November 9, 1853, to March 24, 1861, made at Redhill**. Publication Title: Observations of the spots on the Sun: from November 9 ADS Bibcode: 1863oss..book.....C. Jan. 1863.

[Car64] H. Carmichael. **A Process for Flares**. *NASA Special Publication* 50 (Jan. 1964). 451.

[CB97] Gilles Chabrier and Isabelle Baraffe. *Structure and evolution of low-mass stars*. arXiv:astro-ph/9704118. Apr. 1997. DOI: 10.48550/arXiv.astro-ph/9704118.

[CG87] Arnab Rai Choudhuri and Peter A. Gilman. **The Influence of the Coriolis Force on Flux Tubes Rising through the Solar Convection Zone**. *The Astrophysical Journal* 316 (May 1987). 788. DOI: 10.1086/165243.

[CH18] Ann Marie Cody and Lynne A. Hillenbrand. **The Many-faceted Light Curves of Young Disk-bearing Stars in Upper Sco —- Oph Observed by *K2* Campaign 2**. *The Astronomical Journal* 156:2 (July 2018). 71. DOI: 10.3847/1538-3881/aacead.

[Che+20a] Howard Chen et al. **Persistence of Flare-Driven Atmospheric Chemistry on Rocky Habitable Zone Worlds**. *Nature Astronomy* 5:3 (Dec. 2020). 298–310. DOI: 10.1038/s41550-020-01264-1.

[Che+20b] Jun Chen et al. **Extreme-ultraviolet Late Phase of Solar Flares**. *The Astrophysical Journal* 890 (Feb. 2020). 158. DOI: 10.3847/1538-4357/ab6def.

[Che+23] Judy J. Chebly et al. **Numerical quantification of the wind properties of cool main sequence stars**. *Monthly Notices of the Royal Astronomical Society* 524 (Oct. 2023). 5060–5079. DOI: 10.1093/mnras/stad2100.

[CK06] G. Chabrier and M. Küker. **Large-scale 03b1^2-dynamo in low-mass stars and brown dwarfs**. *Astronomy and Astrophysics* 446 (Feb. 2006). 1027–1037. DOI: 10.1051/0004-6361:20042475.

[Cod+14] Ann Marie Cody et al. **CSI 2264: SIMULTANEOUS OPTICAL AND INFRARED LIGHT CURVES OF YOUNG DISK-BEARING STARS IN NGC 2264 WITH *CoRoT* and *SPITZER* —EVIDENCE FOR MULTIPLE ORIGINS OF VARIABILITY**. *The Astronomical Journal* 147:4 (Mar. 2014). 82. DOI: 10.1088/0004-6256/147/4/82.

[Cod+17] Ann Marie Cody et al. **A Continuum of Accretion Burst Behavior in Young Stars Observed by *K* 2**. *The Astrophysical Journal* 836:1 (Feb. 2017). 41. DOI: 10.3847/1538-4357/836/1/41.

[Cro+18] M. Cropper et al. **Gaia Data Release 2. Gaia Radial Velocity Spectrometer**. *Astronomy and Astrophysics* 616 (Aug. 2018). A5. DOI: 10.1051/0004-6361/201832763.

[CS23] Paul Charbonneau and Dmitry Sokoloff. **Evolution of solar and stellar dynamo theory**. *Space Science Reviews* 219:5 (Aug. 2023). 35. DOI: 10.1007/s11214-023-00980-0.

[Dai+18] Fei Dai et al. **Stellar Obliquity and Magnetic Activity of Planet-hosting Stars and Eclipsing Binaries Based on Transit Chord Correlation**. *The Astronomical Journal* 155 (Apr. 2018). 177. DOI: 10.3847/1538-3881/aab618.

[Dav+14] James R. A. Davenport et al. **Kepler Flares. II. The Temporal Morphology of White-light Flares on GJ 1243**. *The Astrophysical Journal* 797 (Dec. 2014). 122. DOI: 10.1088/0004-637X/797/2/122.

[Dav16] James R. A. Davenport. **THE KEPLER CATALOG OF STELLAR FLARES**. *The Astrophysical Journal* 829:1 (Sept. 2016). 23. DOI: 10.3847/0004-637X/829/1/23.

[DHH15] James R. A. Davenport, Leslie Hebb, and Suzanne L. Hawley. **Detecting Differential Rotation and Starspot Evolution on the M Dwarf GJ 1243 with Kepler**. *The Astrophysical Journal* 806 (June 2015). 212. DOI: 10.1088/0004-637X/806/2/212.

[DJ24] S Daley-Yates and Moira M Jardine. **Simulating stellar coronal rain and slingshot prominences**. en. *Monthly Notices of the Royal Astronomical Society* 534:1 (Sept. 2024). 621–633. DOI: 10.1093/mnras/stae2131.

[DJJ23] Simon Daley-Yates, Moira M Jardine, and Craig D Johnston. **Heating and cooling in stellar coronae: coronal rain on a young Sun**. en. *Monthly Notices of the Royal Astronomical Society* 526:2 (Sept. 2023). 1646–1656. DOI: 10.1093/mnras/stad2752.

[Doy+19] L. Doyle et al. **Probing the origin of stellar flares on M dwarfs using TESS data sectors 1-3**. *Monthly Notices of the Royal Astronomical Society* 489 (Oct. 2019). 437–445. DOI: 10.1093/mnras/stz2205.

[DRD20] L. Doyle, G. Ramsay, and J. G. Doyle. **Superflares and variability in solar-type stars with TESS in the Southern hemisphere**. *Monthly Notices of the Royal Astronomical Society* 494 (May 2020). 3596–3610. DOI: 10.1093/mnras/staa923.

[Fer00] J. M. Ferreira. **A model of slingshot prominences in rapidly rotating stars**. en. *Monthly Notices of the Royal Astronomical Society* 316:3 (Aug. 2000). 647–656. DOI: 10.1046/j.1365-8711.2000.03540.x.

[Fla+19] Kevin Flaherty et al. **The Planet Formation Potential around a 45 Myr Old Accreting M Dwarf**. *The Astrophysical Journal* 872 (Feb. 2019). 92. DOI: 10.3847/1538-4357/aaf794.

[For+13] Daniel Foreman-Mackey et al. **emcee: The MCMC Hammer**. *Publications of the Astronomical Society of the Pacific* 125 (Mar. 2013). 306. DOI: 10.1086/670067.

[Fra+19] F. Fraschetti et al. **Stellar Energetic Particles in the Magnetically Turbulent Habitable Zones of TRAPPIST-1-like Planetary Systems**. *The Astrophysical Journal* 874:1 (Mar. 2019). 21. DOI: 10.3847/1538-4357/ab05e4.

[Fra+22] Federico Fraschetti et al. **Stellar Energetic Particle Transport in the Turbulent and CME-disrupted Stellar Wind of AU Microscopii**. *The Astrophysical Journal* 937:2 (Oct. 2022). 126. DOI: 10.3847/1538-4357/ac86d7.

[Gai+24] E. Gaidos et al. **Climate change in hell: Long-term variation in transits of the evaporating planet K2-22b**. *Astronomy and Astrophysics* 688 (Aug. 2024). L34. DOI: 10.1051/0004-6361/202451332.

[Gai22] Gaia Collaboration. **VizieR Online Data Catalog: Gaia DR3 Part 1. Main source (Gaia Collaboration, 2022)**. *VizieR Online Data Catalog* 1355 (May 2022). I/355. DOI: 10.26093/cds/vizier.1355.

[Gas+13] T. Gastine et al. **What controls the magnetic geometry of M dwarfs?** *Astronomy & Astrophysics* 549 (Jan. 2013). L5. DOI: 10.1051/0004-6361/201220317.

[GCH17] Helen A. C. Giles, Andrew Collier Cameron, and Raphaëlle D. Haywood. **A Kepler study of starspot lifetimes with respect to light-curve amplitude and spectral type**. *Monthly Notices of the Royal Astronomical Society* 472 (Dec. 2017). 1618–1627. DOI: 10.1093/mnras/stx1931.

[Gey11] Charles J. Geyer. "Introduction to Markov Chain Monte Carlo." en. In: *Handbook of Markov Chain Monte Carlo*. 1st ed. New York: Chapman and Hall/CRC, May 2011, 3–48. ISBN: 978-0-429-13850-8. DOI: 10.1201/b10905-2.

[GMY19] N. Gopalswamy, P. Mäkelä, and S. Yashiro. **A Catalog of Type II radio bursts observed by Wind/WAVES and their Statistical Properties**. *Sun and Geosphere* 14 (Jan. 2019). 111–121. DOI: 10.31401/SunGeo.2019.02.03.

[Gne77] M.N. Gnevyshev. **Essential features of the 11-year solar cycle**. en. *Solar Physics* 51:1 (1977). DOI: 10.1007/BF00240455.

[Güd04] Manuel Güdel. **X-ray astronomy of stellar coronae**. *Astronomy and Astrophysics Review* 12 (Sept. 2004). 71–237. DOI: 10.1007/s00159-004-0023-2.

[Gün+20] Maximilian N. Günther et al. **Stellar Flares from the First *TESS* Data Release: Exploring a New Sample of M Dwarfs**. *The Astronomical Journal* 159:2 (Jan. 2020). 60. DOI: 10.3847/1538-3881/ab5d3a.

[Gün+22] Maximilian N. Günther et al. **Complex Modulation of Rapidly Rotating Young M Dwarfs: Adding Pieces to the Puzzle**. *The Astronomical Journal* 163:4 (Apr. 2022). 144. DOI: 10.3847/1538-3881/ac503c.

[GW10] Jonathan Goodman and Jonathan Weare. **Ensemble samplers with affine invariance**. *Communications in Applied Mathematics and Computational Science* 5 (Jan. 2010). 65–80. DOI: 10.2140/camcos.2010.5.65.

[Has70] W. K. Hastings. **Monte Carlo sampling methods using Markov chains and their applications**. en. *Biometrika* 57:1 (Apr. 1970). 97–109. DOI: 10.1093/biomet/57.1.97.

[Her+21] Konstantin Herbst et al. **From Starspots to Stellar Coronal Mass Ejections—Revisiting Empirical Stellar Relations**. *The Astrophysical Journal* 907 (Feb. 2021). 89. DOI: 10.3847/1538-4357/abcc04.

[HF18] David W. Hogg and Daniel Foreman-Mackey. **Data Analysis Recipes: Using Markov Chain Monte Carlo**. *The Astrophysical Journal Supplement Series* 236 (May 2018). 11. DOI: 10.3847/1538-4365/aab76e.

[HFR90] E. R. Houdebine, B. H. Foing, and M. Rodono. **Dynamics of flares on late-type dMe stars. I. Flare mass ejections and stellar evolution.** *Astronomy and Astrophysics* 238 (Nov. 1990). 249.

[HH13] Timothy A. Howard and Richard A. Harrison. **Stealth Coronal Mass Ejections: A Perspective**. *Solar Physics* 285 (July 2013). 269–280. DOI: 10.1007/s11207-012-0217-0.

[Hil+10] Eric J. Hilton et al. **M Dwarf Flares from Time-resolved Sloan Digital Sky Survey Spectra**. *The Astronomical Journal* 140 (Nov. 2010). 1402–1413. DOI: 10.1088/0004-6256/140/5/1402.

[Hir74] T. Hirayama. **Theoretical Model of Flares and Prominences. I: Evaporating Flare Model**. *Solar Physics* 34 (Feb. 1974). 323–338. DOI: 10.1007/BF00153671.

[HM22] Ward S. Howard and Meredith A. MacGregor. **No Such Thing as a Simple Flare: Substructure and Quasi-periodic Pulsations Observed in a Statistical Sample of 20 s Cadence TESS Flares**. *The Astrophysical Journal* 926:2 (Feb. 2022). 204. DOI: 10.3847/1538-4357/ac426e.

[How+20] Ward S. Howard et al. **EvryFlare. II. Rotation Periods of the Cool Flare Stars in TESS across Half the Southern Sky**. *The Astrophysical Journal* 895:2 (June 2020). 140. DOI: 10.3847/1538-4357/ab9081.

[HP91] Suzanne L. Hawley and Bjorn R. Pettersen. **The Great Flare of 1985 April 12 on AD Leonis**. *The Astrophysical Journal* 378 (Sept. 1991). 725. DOI: 10.1086/170474.

[Ibe67] Icko Iben Jr. **Stellar Evolution Within and off the Main Sequence**. *Annual Review of Astronomy and Astrophysics* 5 (Jan. 1967). 571. DOI: 10.1146/annurev.aa.05.090167.003035.

[Ibe74] I. Iben Jr. **Post main sequence evolution of single stars.** *Annual Review of Astronomy and Astrophysics* 12 (Jan. 1974). 215–256. DOI: 10.1146/annurev.aa.12.090174.001243.

[Ili+19] Ekaterina Ilin et al. **Flares in open clusters with K2 . I. M 45 (Pleiades), M 44 (Praesepe), and M 67**. *Astronomy and Astrophysics* 622 (Feb. 2019). A133. DOI: 10.1051/0004-6361/201834400.

[Ili+21a] Ekaterina Ilin et al. **Flares in open clusters with K2. II. Pleiades, Hyades, Praesepe, Ruprecht 147, and M 67**. *Astronomy and Astrophysics* 645 (Jan. 2021). A42. DOI: 10.1051/0004-6361/202039198.

[Ili+21b] Ekaterina Ilin et al. **Giant white-light flares on fully convective stars occur at high latitudes**. en. *Monthly Notices of the Royal Astronomical Society* 507:2 (Aug. 2021). 1723–1745. DOI: 10.1093/mnras/stab2159.

[Ili+23] Ekaterina Ilin et al. **Flaring latitudes in ensembles of low-mass stars**. *Monthly Notices of the Royal Astronomical Society* 523 (Aug. 2023). 4326–4339. DOI: 10.1093/mnras/stad1690.

[Ili+24a] E. Ilin et al. **The corona of a fully convective star with a near-polar flare**. *Astronomy and Astrophysics* 687 (July 2024). A138. DOI: 10.1051/0004-6361/202449541.

[Ili+24b] Ekaterina Ilin et al. **Planetary perturbers: flaring star-planet interactions in Kepler and TESS**. *Monthly Notices of the Royal Astronomical Society* 527 (Jan. 2024). 3395–3417. DOI: 10.1093/mnras/stad3398.

[Ili22] Ekaterina Ilin. **High lights: stellar flares as probes of magnetism in stars and star-planet systems**. PhD thesis. Potsdam: University of Potsdam, 2022.

[Irw+11] Jonathan Irwin et al. **ON THE ANGULAR MOMENTUM EVOLUTION OF FULLY CONVECTIVE STARS: ROTATION PERIODS FOR FIELD M-DWARFS FROM THE MEarth TRANSIT SURVEY**. *The Astrophysical Journal* 727:1 (Jan. 2011). 56. DOI: 10.1088/0004-637X/727/1/56.

[Jar+01] M. Jardine et al. **Prominence support in potential field configurations around rotating stars**. en. *Monthly Notices of the Royal Astronomical Society* 324:1 (June 2001). 201–205. DOI: 10.1046/j.1365-8711.2001.04332.x.

[JC19] Moira Jardine and Andrew Collier Cameron. **Slingshot prominences: nature's wind gauges**. en. *Monthly Notices of the Royal Astronomical Society* 482:3 (Jan. 2019). 2853–2860. DOI: 10.1093/mnras/sty2872.

[Jen+16] Jon M. Jenkins et al. **The TESS science processing operations center**. In: vol. 9913. ADS Bibcode: 2016SPIE.9913E..3EJ. Aug. 2016, 99133E. DOI: 10.1117/12.2233418.

[Joh+21] E. N. Johnson et al. **Simultaneous photometric and CARMENES spectroscopic monitoring of fast-rotating M dwarf GJ 3270: Discovery of a post-flare corotating feature**. *Astronomy & Astrophysics* 651 (July 2021). A105. DOI: 10.1051/0004-6361/202040159.

[Kar+22] Subhajeet Karmakar et al. **AstroSat observations of long-duration X-ray superflares on active M-dwarf binary EQ Peg**. *Monthly Notices of the Royal Astronomical Society* 509 (Jan. 2022). 3247–3257. DOI: 10.1093/mnras/stab3099.

[Kau+24] Simranpreet Kaur et al. *Hints of auroral and magnetospheric polarized radio emission from the scallop-shell star 2MASS J05082729$-$2101444*. Publication Title: arXiv e-prints ADS Bibcode: 2024arXiv241022449K. Oct. 2024. DOI: 10.48550/arXiv.2410.22449.

[KHL12] T. T. Ke, H. Huang, and D. N. C. Lin. **RAPID MID-INFRARED VARIABILITY IN PROTOSTELLAR DISKS**. *The Astrophysical Journal* 745:1 (Jan. 2012). 60. DOI: 10.1088/0004-637X/745/1/60.

[Koc+20] O. Kochukhov et al. **Hidden magnetic fields of young suns**. *Astronomy & Astrophysics* 635 (Mar. 2020). A142. DOI: 10.1051/0004-6361/201937185.

[Koc16] Oleg Kochukhov. **Doppler and Zeeman Doppler Imaging of Stars**. *Lecture Notes in Physics, Berlin Springer Verlag* 914 (Apr. 2016). 177. DOI: 10.1007/978-3-319-24151-7_9.

[Koc21] Oleg Kochukhov. **Magnetic fields of M dwarfs**. en. *The Astronomy and Astrophysics Review* 29:1 (Dec. 2021). 1. DOI: 10.1007/s00159-020-00130-3.

[Koe22] Chris Koen. **Multifilter observations of the complex periodic variations in eight pre-main sequence stars**. en. *Monthly Notices of the Royal Astronomical Society* 518:2 (Nov. 2022). 2921–2937. DOI: 10.1093/mnras/stac3276.

[Kow+13] Adam F. Kowalski et al. **TIME-RESOLVED PROPERTIES AND GLOBAL TRENDS IN dMe FLARES FROM SIMULTANEOUS PHOTOMETRY AND SPECTRA**. *The Astrophysical Journal Supplement Series* 207:1 (July 2013). 15. DOI: 10.1088/0067-0049/207/1/15.

[Kow+25] Adam F. Kowalski et al. **Rising Near-ultraviolet Spectra in Stellar Megaflares**. *The Astrophysical Journal* 978 (Jan. 2025). 81. DOI: 10.3847/1538-4357/ad9395.

[Kow24] Adam F. Kowalski. **Stellar flares**. *Living Reviews in Solar Physics* 21 (Dec. 2024). 1. DOI: 10.1007/s41116-024-00039-4.

[KP76] R. A. Kopp and G. W. Pneuman. **Magnetic reconnection in the corona and the loop prominence phenomenon.** *Solar Physics* 50 (Sept. 1976). 85–98. DOI: 10.1007/BF00206193.

[Kra+14] Adam L. Kraus et al. **A STELLAR CENSUS OF THE TUCANA-HOROLOGIUM MOVING GROUP**. *The Astronomical Journal* 147:6 (May 2014). 146. DOI: 10.1088/0004-6256/147/6/146.

[Kra67] Robert P. Kraft. **Studies of Stellar Rotation. V. The Dependence of Rotation on Age among Solar-Type Stars**. *The Astrophysical Journal* 150 (Nov. 1967). 551. DOI: 10.1086/149359.

[KWR93] James F. Kasting, Daniel P. Whitmire, and Ray T. Reynolds. **Habitable Zones around Main Sequence Stars**. en. *Icarus* 101:1 (Jan. 1993). 108–128. DOI: 10.1006/icar.1993.1010.

[Laf+23] M. Lafarga et al. **The CARMENES search for exoplanets around M dwarfs: Line-by-line sensitivity to activity in M dwarfs**. *Astronomy & Astrophysics* 674 (June 2023). A61. DOI: 10.1051/0004-6361/202245602.

[LBA97] Gregory Laughlin, Peter Bodenheimer, and Fred C. Adams. **The End of the Main Sequence**. en. *The Astrophysical Journal* 482:1 (June 1997). 420–432. DOI: 10.1086/304125.

[Lig+18] Lightkurve Collaboration et al. **Lightkurve: Kepler and TESS time series analysis in Python**. *Astrophysics Source Code Library* (Dec. 2018). ascl:1812.013.

[Lin+21] L. Lindegren et al. **Gaia Early Data Release 3. The astrometric solution**. *Astronomy and Astrophysics* 649 (May 2021). A2. DOI: 10.1051/0004-6361/202039709.

[Lom76] N. R. Lomb. **Least-squares frequency analysis of unequally spaced data**. en. *Astrophysics and Space Science* 39:2 (Feb. 1976). 447–462. DOI: 10.1007/BF00648343.

[Loy+18] R. O. Parke Loyd et al. **The MUSCLES Treasury Survey. V. FUV Flares on Active and Inactive M Dwarfs**. *The Astrophysical Journal* 867 (Nov. 2018). 71. DOI: 10.3847/1538-4357/aae2bd.

[Maa+22] A. J. Maas et al. **Lower-than-expected flare temperatures for TRAPPIST-1**. *Astronomy & Astrophysics* 668 (Dec. 2022). A111. DOI: 10.1051/0004-6361/202243869.

[Mae+21] Hiroyuki Maehara et al. **Time-resolved spectroscopy and photometry of M dwarf flare star YZ Canis Minoris with OISTER and TESS: Blue asymmetry in the H03b1 line during the non-white light flare**. *Publications of the Astronomical Society of Japan* 73 (Feb. 2021). 44–65. DOI: 10.1093/pasj/psaa098.

[Mar+24] David V. Martin et al. **The benchmark M dwarf eclipsing binary CM Draconis with TESS: spots, flares, and ultra-precise parameters**. *Monthly Notices of the Royal Astronomical Society* 528 (Feb. 2024). 963–975. DOI: 10.1093/mnras/stae015.

[Met+53] Nicholas Metropolis et al. **Equation of State Calculations by Fast Computing Machines**. en. *The Journal of Chemical Physics* 21:6 (June 1953). 1087–1092. DOI: 10.1063/1.1699114.

[MK22] E. I. Mason and K. L. Kniezewski. **To Rain or Not to Rain: Correlating GOES Flare Class and Coronal Rain Statistics**. *The Astrophysical Journal* 939:1 (Nov. 2022). 21. DOI: 10.3847/1538-4357/ac94d7.

[Mof74] T. J. Moffett. **UV Ceti flare stars: observational data.** *The Astrophysical Journal Supplement Series* 29 (Dec. 1974). 1–42. DOI: 10.1086/190330.

[Mor+11] M. Morales-Calderón et al. **Ysovar: The First Sensitive, Wide-area, Mid-infrared Photometric Monitoring of the Orion Nebula Cluster**. *The Astrophysical Journal* 733 (May 2011). 50. DOI: 10.1088/0004-637X/733/1/50.

[Mos+19] Sofia-Paraskevi Moschou et al. **The Stellar CME–Flare Relation: What Do Historic Observations Reveal?** *The Astrophysical Journal* 877:2 (June 2019). 105. DOI: 10.3847/1538-4357/ab1b37.

[MW20] Kento Masuda and Joshua N. Winn. **On the Inference of a Star's Inclination Angle from its Rotation Velocity and Projected Rotation Velocity**. *The Astronomical Journal* 159:3 (Mar. 2020). 81. DOI: 10.3847/1538-3881/ab65be.

[New+16] Elisabeth R. Newton et al. **THE ROTATION AND GALACTIC KINEMATICS OF MID M DWARFS IN THE SOLAR NEIGHBORHOOD**. *The Astrophysical Journal* 821:2 (Apr. 2016). 93. DOI: 10.3847/0004-637X/821/2/93.

[New+17] Elisabeth R. Newton et al. **THE H03b1 EMISSION OF NEARBY M DWARFS AND ITS RELATION TO STELLAR ROTATION**. *The Astrophysical Journal* 834:1 (Jan. 2017). 85. DOI: 10.3847/1538-4357/834/1/85.

[Not+19] Yuta Notsu et al. **Do Kepler Superflare Stars Really Include Slowly Rotating Sun-like Stars?—Results Using APO 3.5 m Telescope Spectroscopic Observations and Gaia-DR2 Data**. *The Astrophysical Journal* 876:1 (May 2019). 58. DOI: 10.3847/1538-4357/ab14e6.

[Not+24] Yuta Notsu et al. **Apache Point Observatory (APO)/SMARTS Flare Star Campaign Observations. I. Blue Wing Asymmetries in Chromospheric Lines during Mid-M-Dwarf Flares from Simultaneous Spectroscopic and Photometric Observation Data**. *The Astrophysical Journal* 961 (Feb. 2024). 189. DOI: 10.3847/1538-4357/ad062f.

[NV20] Y. Netto and A. Valio. **Stellar magnetic activity and the butterfly diagram of Kepler-63**. *Astronomy & Astrophysics* 635 (Mar. 2020). A78. DOI: 10.1051/0004-6361/201936219.

[Oss03] Mathieu Ossendrijver. **The solar dynamo**. *Astronomy and Astrophysics Review* 11 (Jan. 2003). 287–367. DOI: 10.1007/s00159-003-0019-3.

[OW17] Rachel A. Osten and Scott J. Wolk. **A Framework for Finding and Interpreting Stellar CMEs**. In: vol. 328. ADS Bibcode: 2017IAUS..328..243O. Oct. 2017, 243–251. DOI: 10.1017/S1743921317004252.

[Pal+22] Elsa K. Palumbo et al. **Evidence for Centrifugal Breakout around the Young M Dwarf TIC 234284556**. *The Astrophysical Journal* 925 (Jan. 2022). 75. DOI: 10.3847/1538-4357/ac38a5.

[Par55] Eugene N. Parker. **Hydromagnetic Dynamo Models.** *The Astrophysical Journal* 122 (Sept. 1955). 293. DOI: 10.1086/146087.

[Pas+19] V. M. Passegger et al. **The CARMENES search for exoplanets around M dwarfs: Photospheric parameters of target stars from high-resolution spectroscopy. II. Simultaneous multiwavelength range modeling of activity insensitive lines**. *Astronomy & Astrophysics* 627 (July 2019). A161. DOI: 10.1051/0004-6361/201935679.

[Pau+18] Rishi R. Paudel et al. **K2 Ultracool Dwarfs Survey. IV. Monster Flares Observed on the Young Brown Dwarf CFHT-BD-Tau 4**. *The Astrophysical Journal* 861:2 (July 2018). 76. DOI: 10.3847/1538-4357/aac8e0.

[PD24] Susanne Pfalzner and Furkan Dincer. **Low-mass Stars: Their Protoplanetary Disk Lifetime Distribution**. *The Astrophysical Journal* 963 (Mar. 2024). 122. DOI: 10.3847/1538-4357/ad1bef.

[Pet+10] W. M. Peterson et al. **A large coronal loop in the Algol system**. en. *Nature* 463:7278 (Jan. 2010). 207–209. DOI: 10.1038/nature08643.

[Pie+22] M. Pietras et al. **Statistical Analysis of Stellar Flares from the First Three Years of TESS Observations**. *The Astrophysical Journal* 935:2 (Aug. 2022). 143. DOI: 10.3847/1538-4357/ac8352.

[PM13] Mark J. Pecaut and Eric E. Mamajek. **Intrinsic Colors, Temperatures, and Bolometric Corrections of Pre-main-sequence Stars**. *The Astrophysical Journal Supplement Series* 208 (Sept. 2013). 9. DOI: 10.1088/0067-0049/208/1/9.

[Pop+21] Mark Popinchalk et al. **Evaluating Rotation Periods of M Dwarfs across the Ages**. *The Astrophysical Journal* 916:2 (Aug. 2021). 77. DOI: 10.3847/1538-4357/ac0444.

[Pop+23] Mark Popinchalk et al. **Examining the Rotation Period Distribution of the 40 Myr Tucana–Horologium Association with TESS**. *The Astrophysical Journal* 945:2 (Mar. 2023). 114. DOI: 10.3847/1538-4357/acb055.

[Qui+14] A. Quirrenbach et al. **CARMENES instrument overview**. 9147 (July 2014). 91471F. DOI: 10.1117/12.2056453.

[Ram+21] Gavin Ramsay et al. **Transiting Exoplanet Survey Satellite (TESS) Observations of Flares and Quasi-Periodic Pulsations from Low-Mass Stars and Potential Impact on Exoplanets**. *Solar Physics* 296 (Nov. 2021). 162. DOI: 10.1007/s11207-021-01899-x.

[Rap+14] S. Rappaport et al. **M-DWARF RAPID ROTATORS AND THE DETECTION OF RELATIVELY YOUNG MULTIPLE M-STAR SYSTEMS**. *The Astrophysical Journal* 788:2 (May 2014). 114. DOI: 10.1088/0004-637X/788/2/114.

[Rea+97] F. Reale et al. **Determination of the length of coronal loops from the decay of X-ray flares I. Solar flares observed with YOHKOH SXT.** *Astronomy and Astrophysics* 325 (Sept. 1997). 782–790.

[Rea14] Fabio Reale. **Coronal Loops: Observations and Modeling of Confined Plasma**. en. *Living Reviews in Solar Physics* 11 (2014). DOI: 10.12942/lrsp-2014-4.

[Reb+22] L. M. Rebull et al. **Rotation of Low-mass Stars in Upper Centaurus–Lupus and Lower Centaurus–Crux with TESS**. *The Astronomical Journal* 164:3 (Sept. 2022). 80. DOI: 10.3847/1538-3881/ac75f1.

[Rei+22] A. Reiners et al. **Magnetism, rotation, and nonthermal emission in cool stars: Average magnetic field measurements in 292 M dwarfs**. *Astronomy & Astrophysics* 662 (June 2022). A41. DOI: 10.1051/0004-6361/202243251.

[Rib+23] I. Ribas et al. **The CARMENES search for exoplanets around M dwarfs: Guaranteed time observations Data Release 1 (2016-2020)**. *Astronomy & Astrophysics* 670 (Feb. 2023). A139. DOI: 10.1051/0004-6361/202244879.

[Ric+14] George R. Ricker et al. **Transiting Exoplanet Survey Satellite**. en. *Journal of Astronomical Telescopes, Instruments, and Systems* 1:1 (Oct. 2014). 014003. DOI: 10.1117/1.JATIS.1.1.014003.

[Rim+18] Paul B. Rimmer et al. **The origin of RNA precursors on exoplanets**. en. *Science Advances* 4:8 (Aug. 2018). eaar3302. DOI: 10.1126/sciadv.aar3302.

[RJG12] Ansgar Reiners, Nandan Joshi, and Bertrand Goldman. **A CATALOG OF ROTATION AND ACTIVITY IN EARLY-M STARS**. *The Astronomical Journal* 143:4 (Apr. 2012). 93. DOI: 10.1088/0004-6256/143/4/93.

[Ros+14] G. P. Rosotti et al. **Protoplanetary disc evolution affected by star-disc interactions in young stellar clusters**. en. *Monthly Notices of the Royal Astronomical Society* 441:3 (May 2014). 2094–2110. DOI: 10.1093/mnras/stu679.

[RV18] Rachael M. Roettenbacher and Krisztián Vida. **The Connection between Starspots and Flares on Main-sequence Kepler Stars**. *The Astrophysical Journal* 868 (Nov. 2018). 3. DOI: 10.3847/1538-4357/aae77e.

[RWS17] Sukrit Ranjan, Robin Wordsworth, and Dimitar D. Sasselov. **The Surface UV Environment on Planets Orbiting M Dwarfs: Implications for Prebiotic Chemistry and the Need for Experimental Follow-up**. *The Astrophysical Journal* 843 (July 2017). 110. DOI: 10.3847/1538-4357/aa773e.

[San+22] H Sanderson et al. **Can scallop-shell stars trap dust in their magnetic fields?** en. *Monthly Notices of the Royal Astronomical Society* 518:3 (Dec. 2022). 4734–4745. DOI: 10.1093/mnras/stac3302.

[Sca82] J. D. Scargle. **Studies in astronomical time series analysis. II. Statistical aspects of spectral analysis of unevenly spaced data.** *The Astrophysical Journal* 263 (Dec. 1982). 835–853. DOI: 10.1086/160554.

[Sch98] Arthur Schuster. **On the investigation of hidden periodicities with application to a supposed 26 day period of meteorological phenomena**. en. *Terrestrial Magnetism* 3:1 (Mar. 1898). 13–41. DOI: 10.1029/TM003i001p00013.

[Scu+16] E. Scullion et al. **OBSERVING THE FORMATION OF FLARE-DRIVEN CORONAL RAIN**. *The Astrophysical Journal* 833:2 (Dec. 2016). 184. DOI: 10.3847/1538-4357/833/2/184.

[Seg+10] Antígona Segura et al. **The Effect of a Strong Stellar Flare on the Atmospheric Chemistry of an Earth-like Planet Orbiting an M Dwarf**. en. *Astrobiology* 10:7 (Sept. 2010). 751–771. DOI: 10.1089/ast.2009.0376.

[SF99] J. H. M. M. Schmitt and F. Favata. **Continuous heating of a giant X-ray flare on Algol**. en. *Nature* 401:6748 (Sept. 1999). 44–46. DOI: 10.1038/43389.

[Shi+13] Kazunari Shibata et al. **Can Superflares Occur on Our Sun?** *Publications of the Astronomical Society of Japan* 65 (June 2013). 49. DOI: 10.1093/pasj/65.3.49.

[Shu+19] D. Shulyak et al. **Magnetic fields in M dwarfs from the CARMENES survey**. *Astronomy & Astrophysics* 626 (June 2019). A86. DOI: 10.1051/0004-6361/201935315.

[Sil+10] A. Silva-Valio et al. **Properties of starspots on CoRoT-2**. *Astronomy and Astrophysics* 510 (Feb. 2010). A25. DOI: 10.1051/0004-6361/200911904.

[Sil+20] Steven M. Silverberg et al. **Peter Pan Disks: Long-lived Accretion Disks Around Young M Stars**. *The Astrophysical Journal* 890:2 (Feb. 2020). 106. DOI: 10.3847/1538-4357/ab68e6.

[Sil03] Adriana V. R. Silva. **Method for Spot Detection on Solar-like Stars**. *The Astrophysical Journal* 585:2 (Mar. 2003). L147–L150. DOI: 10.1086/374324.

[Sim+24] Paulo J A Simões et al. **Hydrogen recombination continuum as the radiative model for stellar optical flares**. en. *Monthly Notices of the Royal Astronomical Society* 528:2 (Jan. 2024). 2562–2567. DOI: 10.1093/mnras/stae186.

[SM03] S. Seager and G. Mallen-Ornelas. **A Unique Solution of Planet and Star Parameters from an Extrasolar Planet Transit Light Curve**. en. *The Astrophysical Journal* 585:2 (Mar. 2003). 1038–1055. DOI: 10.1086/346105.

[Sok+13] Igor V. Sokolov et al. **MAGNETOHYDRODYNAMIC WAVES AND CORONAL HEATING: UNIFYING EMPIRICAL AND MHD TURBULENCE MODELS**. *The Astrophysical Journal* 764:1 (Jan. 2013). 23. DOI: 10.1088/0004-637X/764/1/23.

[Spi+23] R. Spinelli et al. **The ultraviolet habitable zone of exoplanets**. *Monthly Notices of the Royal Astronomical Society* 522 (June 2023). 1411–1418. DOI: 10.1093/mnras/stad928.

[Spi+24] R. Spinelli et al. **The time evolution of the ultraviolet habitable zone**. *Monthly Notices of the Royal Astronomical Society: Letters* 533:1 (June 2024). L76–L82. DOI: 10.1093/mnrasl/slae064.

[SR98] K. G. Strassmeier and J. B. Rice. **Doppler imaging of stellar surface structure. VI. HD 129333 = EK Draconis: a stellar analog of the active young Sun**. *Astronomy and Astrophysics* 330 (Feb. 1998). 685–695.

[SS92] M. Schuessler and S. K. Solanki. **Why rapid rotators have polar spots.** *Astronomy and Astrophysics* 264 (Oct. 1992). L13–L16.

[Sta+17] John Stauffer et al. **Orbiting Clouds of Material at the Keplerian Corotation Radius of Rapidly Rotating Low-mass WTTs in Upper Sco**. *The Astronomical Journal* 153:4 (Mar. 2017). 152. DOI: 10.3847/1538-3881/aa5eb9.

[Sta+18a] Keivan G. Stassun et al. **The TESS Input Catalog and Candidate Target List**. *The Astronomical Journal* 156:3 (Sept. 2018). 102. DOI: 10.3847/1538-3881/aad050.

[Sta+18b] John Stauffer et al. **More Rapidly Rotating PMS M Dwarfs with Light Curves Suggestive of Orbiting Clouds of Material**. *The Astronomical Journal* 155:2 (Jan. 2018). 63. DOI: 10.3847/1538-3881/aaa19d.

[Sta+21] John Stauffer et al. **Even More Rapidly Rotating Pre-main-sequence M Dwarfs with Highly Structured Light Curves: An Initial Survey in the Lower Centaurus-Crux and Upper Centaurus-Lupus Associations**. *The Astronomical Journal* 161:2 (Feb. 2021). 60. DOI: 10.3847/1538-3881/abc7c6.

[Str+17] K. G. Strassmeier et al. **CoRoT photometry and STELLA spectroscopy of an eccentric, eclipsing, and spotted HgMn binary with sub-synchronized rotation**. *Astronomy & Astrophysics* 597 (Jan. 2017). A55. DOI: 10.1051/0004-6361/201629150.

[Str09] Klaus G. Strassmeier. **Starspots**. en. *The Astronomy and Astrophysics Review* 17:3 (Sept. 2009). 251–308. DOI: 10.1007/s00159-009-0020-6.

[Stu66] P. A. Sturrock. **Model of the High-Energy Phase of Solar Flares**. *Nature* 211 (Aug. 1966). 695–697. DOI: 10.1038/211695a0.

[STZ00] Ian Sammis, Frances Tang, and Harold Zirin. **The Dependence of Large Flare Occurrence on the Magnetic Structure of Sunspots**. en. *The Astrophysical Journal* 540:1 (Sept. 2000). 583–587. DOI: 10.1086/309303.

[SY02] Kazunari Shibata and Takaaki Yokoyama. **A Hertzsprung-Russell–like Diagram for Solar/Stellar Flares and Corona: Emission Measure versus Temperature Diagram**. en. *The Astrophysical Journal* 577:1 (Sept. 2002). 422–432. DOI: 10.1086/342141.

[Til+19] Matt A. Tilley et al. **Modeling Repeated M Dwarf Flaring at an Earth-like Planet in the Habitable Zone: Atmospheric Effects for an Unmagnetized Planet**. en. *Astrobiology* 19:1 (Jan. 2019). 64–86. DOI: 10.1089/ast.2017.1794.

[TOG05] R. H. D. Townsend, S. P. Owocki, and D. Groote. **The Rigidly Rotating Magnetosphere of 03c3 Orionis E**. en. *The Astrophysical Journal* 630:1 (Sept. 2005). L81–L84. DOI: 10.1086/462413.

[Van18] Jacob T. VanderPlas. **Understanding the Lomb-Scargle Periodogram**. *The Astrophysical Journal Supplement Series* 236 (May 2018). 16. DOI: 10.3847/1538-4365/aab766.

[Vid21] Aline A. Vidotto. **The evolution of the solar wind**. en. *Living Reviews in Solar Physics* 18:1 (Dec. 2021). 3. DOI: 10.1007/s41116-021-00029-w.

[Wau+21] Rose F P Waugh et al. **Slingshot prominences: a hidden mass loss mechanism**. en. *Monthly Notices of the Royal Astronomical Society* 505:4 (June 2021). 5104–5116. DOI: 10.1093/mnras/stab1709.

[WB16] Maria A. Weber and Matthew K. Browning. **Modeling the Rise of Fibril Magnetic Fields in Fully Convective Stars**. *The Astrophysical Journal* 827 (Aug. 2016). 95. DOI: 10.3847/0004-637X/827/2/95.

[WD16] Nicholas J. Wright and Jeremy J. Drake. **Solar-type dynamo behaviour in fully convective stars without a tachocline**. *Nature* 535 (July 2016). 526–528. DOI: 10.1038/nature18638.

[Wol+08] U. Wolter et al. **Doppler imaging an X-ray flare on the ultrafast rotator BO Mic: A contemporaneous multiwavelength study using XMM-Newton and VLT**. *Astronomy & Astrophysics* 478:1 (Jan. 2008). L11–L14. DOI: 10.1051/0004-6361:20078838.

[Woo+11] Thomas N. Woods et al. **NEW SOLAR EXTREME-ULTRAVIOLET IRRADIANCE OBSERVATIONS DURING FLARES**. *The Astrophysical Journal* 739:2 (Oct. 2011). 59. DOI: 10.1088/0004-637X/739/2/59.

[Woo04] Brian E. Wood. **Astrospheres and Solar-like Stellar Winds**. en. *Living Reviews in Solar Physics* 1 (2004). DOI: 10.12942/lrsp-2004-2.

[Wri+11] Nicholas J. Wright et al. **The Stellar-activity-Rotation Relationship and the Evolution of Stellar Dynamos**. *The Astrophysical Journal* 743 (Dec. 2011). 48. DOI: 10.1088/0004-637X/743/1/48.

[Wya+15] M. C. Wyatt et al. **Five steps in the evolution from protoplanetary to debris disk**. en. *Astrophysics and Space Science* 357:2 (June 2015). 103. DOI: 10.1007/s10509-015-2315-6.

[Xu+24] Yu Xu et al. **Simulated Coronal Mass Ejections on a Young Solar-type Star and the Associated Instantaneous Angular Momentum Loss**. *The Astrophysical Journal* 971 (Aug. 2024). 153. DOI: 10.3847/1538-4357/ad5845.

[Yad+15] Rakesh K. Yadav et al. **EXPLAINING THE COEXISTENCE OF LARGE-SCALE AND SMALL-SCALE MAGNETIC FIELDS IN FULLY CONVECTIVE STARS**. *The Astrophysical Journal* 813:2 (Nov. 2015). L31. DOI: 10.1088/2041-8205/813/2/L31.

[Yan+23] Kai E. 51ef Yang 6768 et al. **A Possible Mechanism for the "Late Phase" in Stellar White-light Flares**. *The Astrophysical Journal* 959:1 (Dec. 2023). 54. DOI: 10.3847/1538-4357/ad077d.

[Yas+06] S. Yashiro et al. **Different Power-Law Indices in the Frequency Distributions of Flares with and without Coronal Mass Ejections**. en. *The Astrophysical Journal* 650:2 (Oct. 2006). L143–L146. DOI: 10.1086/508876.

[Zha+07] L.Y. Zhang et al. **Longitudinal distribution of major solar flares during 1975–2005**. en. *Advances in Space Research* 40:7 (Jan. 2007). 970–975. DOI: 10.1016/j.asr.2006.12.052.

[Zha+19] Z. Zhan et al. **Complex Rotational Modulation of Rapidly Rotating M Stars Observed with TESS**. *The Astrophysical Journal* 876:2 (May 2019). 127. DOI: 10.3847/1538-4357/ab158c.

# A Appendix A: MCMC in practice

## A.1 The Metropolis-Hastings (M-H) algorithm

The most common and simple MCMC algorithm is the Metropolis-Hastings [M-H; Has70; Met+53] algorithm. The M-H algorithm is not the final used algorithm in this thesis, it is useful to go through its procedure to better understand more advanced MCMC algorithms: from data to the equilibrium distribution or the resulting posterior PDF. Figure A.1 illustrates a simple scenario. Consider a Markov chain that starts with a value A at step $x_1$. The goal is to determine the value of step $x_2$. By definition of a Markov chain, value at $x_2$ is determined solely by $x_1$.

The M-H algorithm generates sample $B$ at $x_2$ by doing the following:

1. Draw a proposal value for $x_2$ from a proposal PDF. The proposal PDF is generated from a Gaussian distribution that centers on value $A$ at $x_1$. If value B is proposed, the proposal PDF is defined as $Q(B|A) = \mathcal{N}(A, \sigma^2)$.
2. Draw a random number $0 < r < 1$ from a uniform distribution.
3. Compute $P(B|D)/P(A|D)$, following Equation 4.5.
4. If $P(B|D)/P(A|D) > r$, accept $B$ as the value at $x_2$.
5. Otherwise, value at $x_2$ remains to be $A$. Meaning $A$ gets repeated and the process continues.

In a more mathematical term, the M-H algorithm dictates that the new sample $B$, with the previous sample $A$, is accepted with a probability:

$$\min\left(1, \frac{P(B|D)}{P(A|D)} \frac{Q(A|B)}{Q(B|A)}\right). \tag{A.1}$$

The reason why this algorithm, and every MCMC algorithm, works is not trivial. Hogg and Foreman-Mackey [HF18] pointed that there are two components to the argument, but I believe the argument becomes clearer if it is explained in three components.

First, a fundamental property of a Markov process is that it produces a unique stationary distribution $p(x)$. This stationary distribution is often referred as the equilibrium distribution and it is illustrated in Figure A.1. Geyer [Gey11] noted that a Markov chain stabilizes when the probability distribution $p(x)$ does not depend on $x$. In other words, when the chain runs long enough, the probability distribution $p(x)$ in element $x_n$ and $x_{n+k}$ of the Markov chain are the same and becomes independent of the starting state.

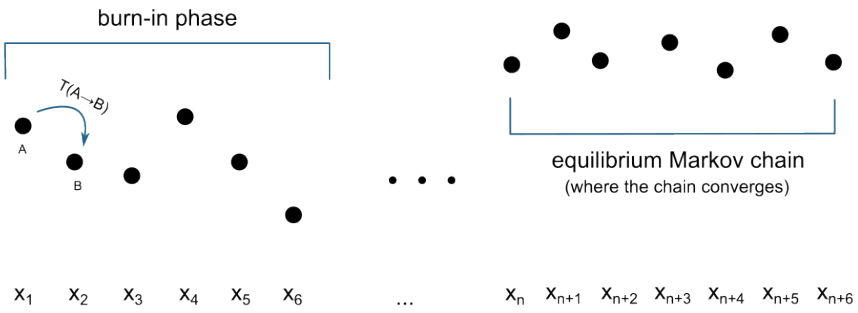


**Figure A.1:** Simple illustration of one Markov chain, consisting of a burn-in phase and the equilibrium Markov chain. The goal of an MCMC is to go from the "chaotic" burn-in phase, where the PDF of each point is different, to the equilibrium distribution that represents the posterior PDF. The burn-in phase is then removed when reporting the end PDF.

Second, the equilibrium distribution $p(x)$ of the Markov chain is proportional to $P(\theta|D)$ when the acceptance algorithm uses the likelihood function and the prior PDF to determine $P(\theta|D)$ (Equation 4.5). Remember that MCMC is essentially a biased random walk, that is biased in such a way that the chain favors high-probability regions while occasionally samples low-probability regions, i.e., if $P(B|D) > P(A|D)$, $B$ is guaranteed to be accepted and less likely otherwise. This bias makes sure that the amount of time the chain spends at $\theta$ is proportional to $f(\theta) \propto \mathcal{L}(D|\theta)\,\pi_\theta(\theta) \propto P(\theta|D)$.

Lastly, to ensure that the Markov chain indeed produces an equilibrium distribution $p(x)$ that samples from $P(\theta|D)$, the acceptance algorithm must fulfill the detailed-balance condition. The detailed-balance condition, explained by Geyer [Gey11], requires:

$$T(A \to B) = T(B \to A) \tag{A.2}$$

$$P(A|D)\,Q(B|A)\,a(A \to B) = P(B|D)\,Q(A|B)\,a(B \to A) \tag{A.3}$$

where $T(A \to B)$ is the probability of value $A$ at $x_n$ transitioning to value $B$ at $x_{n+1}$, $a(A \to B)$ is the probability of accepting $A$ transitioning to $B$, and vice versa. A way to read Equation A.3 is that: the probability of $A$ moves to $B$ depends on the probability of $A$ existing in the posterior PDF, the probability of $B$ being proposed, and the probability of $B$ being accepted. In short, the detailed-balance ensures reversibility, that it is equally probable for $A$ to transition to $B$ as it is the other way around. This reversibility is a crucial requirement for a Markov chain to stabilizes to an equilibrium distribution.

## A.2 emcee and the stretch-move algorithm

The main difference between the mostly-used M-H algorithm (see Section A.1) and the stretch move algorithm is the proposal distribution. The proposal distribution of the M-H algorithm essentially only considers one chain, i.e., each data points in the M-H algorithm is only determined by the points before them in the *same chain*. The stretch move algorithm considers an ensemble of $n$ walkers that each walker produces its own chain. The proposal distribution of one point in one chain made by walker $a$ is determined by a point *in another chain* by a random walker $b$ from the ensemble. This is illustrated in Figure A.2.

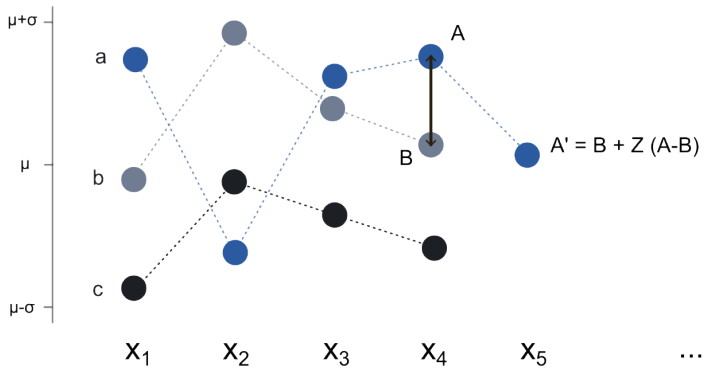


**Figure A.2:** Simple illustration of a stretch-move algorithm used by `emcee`. There are three walkers ($a$, $b$, $c$) making three chains along the mean value $\mu$. The next position of walker $a$, denoted $A'$, is determined based on the the latest values from a randomly chosen chain, in this case chain $b$ ($B$), and chain $a$ ($A$).

To update the position of walker $a$, currently at $x_n$ with value $A$, to value $A'$ at position $x_{n+1}$, the new position is proposed by the stretch algorithm as:

$$A' = B + Z(A - B), \tag{A.4}$$

with $B$ is the value of randomly drawn walker $b$ at position $x_n$ and Z is a random variable drawn from distribution $g(z)$. Goodman and Weare [GW10] suggested that $g(z)$ should take the form:

$$g(z) = \begin{cases} \frac{1}{\sqrt{Z}} & \text{if} \in \left[\frac{1}{a}, a\right] \\ 0 & \text{otherwise} \end{cases} \tag{A.5}$$

with $a = 2$ that fulfills:

$$g(z^{-1}) = z\, g(z) \tag{A.6}$$

and makes the proposal of Equation A.4 symmetric. Because $g(z)$ is assured to be symmetric, the chain can satisfy the detailed balance requirement (see Section A.1).

It indeed does satisfy the detailed balance requirement if the proposal is accepted with probability:

$$\min\left(1, Z^{N-1}\,\frac{P(A'|D)}{P(A|D)}\right), \tag{A.7}$$

where N is the dimension of the parameter space (see again Equation 4.2).

The stretch-move and M-H algorithm, as mentioned before, only differ in the proposal distribution. Therefore, the numerical application of the stretch-move algorithm are similar to the M-H algorithm. The algorithm generates $A'$ for walker $a$ at $x_2$ by doing the following:

1. For chain from walker $a$ with value $A$ at $x_1$, randomly draw walker $b$ from the ensemble with value $B$ at $x_1$.
2. Draw a random number $0.5 < z < 2$ from $g(z)$.
3. Compute $A' = B + Z(A - B)$.
4. Draw a random number $0 < r < 1$ from a uniform distribution.
5. Compute $Z^{N-1}\,P(A'|D)/P(A|D)$, following Equation 4.5.
6. If $Z^{N-1}\,P(A'|D)/P(A|D) > r$, accept $A'$ as the value at $x_2$ for walker $a$.
7. Otherwise, value at $x_2$ remains to be $A$. Meaning $A$ gets repeated and the process continues.

The stretch move algorithm is found to converge faster than the M-H algorithm [see For+13]. This is due to the proposal mechanism, specifically the stretch move itself. The amount of distance a walker can traverse in the next time step is essentially a factor of the relative positions between the walkers in the ensemble. As seen in Figure A.2, the next position $A'$ for walker $a$ is determined by taking the position $B$ of walker $b$ and adding a scaled difference $A - B$ between the two walkers. The value $Z$ determines how much this difference is "stretched". Equation A.5 uses value $a = 2$ that allows exploration of the parameter space to some degree while still conserving efficiency. In other words, the algorithm proposes new positions that are at least half of the distance between two different walkers and at most twice as far. This prevents the walkers from straying too far from its ensemble, which shortens burn-in phase and speeds up convergence. This can be done in parallel and becomes the choice of algorithm for `emcee`.

## A.3 Autocorrelation time and convergence

I have explained why MCMC can be used to sample posterior PDFs from the properties of Markov processes (Section 4.3.1) and the algorithm used in this thesis (Section A.2). The next question after how MCMC guarantees good representation of the posterior is: when does the chain return good representation of the posterior?

In other words, **how long should MCMC be run to be sure that the equilibrium Markov chain has been reached?** Hogg and Foreman-Mackey [HF18] recommended autocorrelation analysis to answer this question.

The nature of the Markov process means that the individual points of the chain are not fully independent of each other, i.e., one point is, at least, always dependent on its immediate neighbor. Furthermore, a point in the chain can still have some degree of dependence on two, three, or even more previous points, since the point it is based on may itself depend on another earlier point. Recall that the equilibrium distribution (see Figure A.1) is reached when the resulting distribution is no longer dependent on the time step: regardless of $x_{n-1}$ the distribution at $f(x_n)$ is identical to $f(x_{n-1})$ and beyond. One indication of this is that the chain becomes independent of its starting state. Autocorrelation time measures how many steps needed to be taken for the chain to be completely independent of its starting point. It essentially quantifies how many steps after $x_n$ for a point in the to be completely independent of $x_n$ from their covariances. **The key idea is that, if the chain has been run for several multiples of the autocorrelation time, then the chain should have converged to its equilibrium distribution.**

For every MCMC run in thesis, I checked their convergence by plotting the autocorrelation time $\tau$ of the Markov chain for every 500 steps. I used the autocorrelation function already provided in `emcee`. Because all MCMC sampling I did in this thesis involved more than one parameter, hence $\tau = \tau_1, \tau_2, ..., \tau_n$, I plotted their average for the convergence analysis as instead of creating individual ones for every parameter $\hat{\tau}$ (see Figure 4.3). Foreman-Mackey et al. [For+13] suggested that a chain is can be considered converged when the number of iterations is more than $50\hat{\tau}$ and the $\hat{\tau}$ estimates changed by less than 1%. There are times when this criteria can not be fulfilled due to computational time, i.e., the large number of parameters made it unrealistic reach $50\hat{\tau}$. When that happens, I decided to do convergence analysis by visually inspecting the chain manually and seeing if the $\hat{\tau}$ estimates vs iteration plot have reached a plateau. If the chain has reached the plateau even before the iteration reached $50\hat{\tau}$, I considered the chain to be converged when the MCMC run has reached more than 12 hours of computation.

# B Appendix B: Periodograms

## B.1 Classical periodogram

A periodogram is a Fourier transform. This section specifically discusses the relationship between a periodogram and the power spectrum, with the hope of making it clearer why the period from a Fourier-based periodogram cannot yield uncertainties in the form of a PDF.

Consider a continuous signal of $g(t)$ with the true period $P_{\text{true}}$ and frequency $f_{\text{true}}$. Fourier transform is essentially a measurement of the energy, or strength of relevance, of a particular frequency within a signal. It, in its literal sense, "sweeps" through a range of winding frequency $f$ to find $f_{\text{true}}$. By this definition, the Fourier transform of $g(t)$ is given by:

$$\mathcal{F}\{g\} = \hat{g}(f) \equiv \int_{-\infty}^{\infty} g(t)\, e^{-2\pi i f t}\, dt, \tag{B.1}$$

with $i$ denoting $\sqrt{-1}$ and $f$ is the winding frequency $1/P$, the inverse of the winding period $P$. This equation is a powerful mathematical tool that allows the identification of which frequency (or frequencies), if superposition of signals with different frequencies was involved) that was used to construct $g(t)$.

A Fourier transform returns a set of amplitudes for every frequencies it considers. This is the strength of relevance mentioned previously. When the resulting amplitudes are squared, it gives the power spectral density (PSD), or power spectrum, defined by:

$$\mathcal{P}_g = |\mathcal{F}\{g\}|^2. \tag{B.2}$$

Squaring the amplitudes of the resulting transform means that any contribution of the complex component and the consequences of the phase in the analysis, from the chosen temporal baseline, to negative values is removed. The power spectrum returns positive real-valued function of the winding frequency $f$ that represents the contribution of each $f$ in the signal.

In Equation B.1, the Fourier transform of $g(t)$, and its power spectrum, is investigated from an infinite time interval. This makes sense in a mathematical standpoint, but it is unrealistic in most, if not all, practical applications of Fourier analysis. In real-world data, a Fourier transform involves some finite span of time with a finite sampling rate. Consider that the finite time interval, or the observing window, is defined by the window function $W(t)$. The signal that is observed and investigated in the Fourier analysis is **not** $g(t)$ but the *pointwise product* of the true signal with the observing window $W(t)$:

$$g_{\text{obs}}(t) = g(t)\, W(t). \tag{B.3}$$

If $g(t)$ is sampled with a finite time interval and a continuous sampling rate, $W(t)$ is described as a box function. More often, the true signal is sampled with a discrete and regular sampling rate. In this case, the window function can be represented with a Dirac comb $\text{III}_{\Delta t}(t)$ at even intervals $\Delta t$. With the Dirac comb, the observed signal is defined as:

$$g_{\text{obs}}(t) = g(t)\, \text{III}_{\Delta t}(t), \tag{B.4}$$

and its Fourier transform is given by:

$$\hat{g}_{\text{obs}}(t) = \sum_{n=1}^{N} g_n\, e^{2\pi i f t_n}, \tag{B.5}$$

with $g_n = g(n\Delta t)$ and $t_n = n\Delta t$, and Equation B.5 is a discrete Fourier transform.

From Equation B.2, the positive real-valued amplitudes of the Equation B.5 can therefore be written as:

$$\mathcal{P}_{g_{\text{obs}}} = \left| \sum_{n=1}^{N} g_n\, e^{2\pi i f t_n} \right|^2. \tag{B.6}$$

When it is multiplied by $1/N$, with $N$ as the total number of samples:

$$\mathcal{P}_S(f) = \frac{1}{N} \left| \sum_{n=1}^{N} g_n\, e^{2\pi i f t_n} \right|^2, \tag{B.7}$$

Equation B.6 becomes the Classical Periodogram, first proposed by Schuster [Sch98]. It should be noted that this periodogram **only applies for cases with a uniform sampling rate**, in which the intervals of the Dirac comb is even for the entirety of the window function.

From Equation B.5-B.7, it can be seen that the periodogram is an *estimator* of the power spectrum. This makes sense, since the power spectrum returns the relevancy of each frequency, with the maximum power (or amplitude) as its most dominant frequency. While it is tempting to simply state that a periodogram *is* the power spectrum of its original signal, the periodogram of a real-world data works with a finite sampling rate. In other words, the periodogram is the power spectrum computed from, at the end of the day, an *incomplete* dataset of the original signal. They, of course, can yield identical results in practice, if the periodogram is computed properly with the the right dataset. However, conceptually they are still different two different things and it becomes even in Section 4.4.1 when the true, continuous signal is sampled unevenly.

## B.2 Lomb-Scargle periodogram

When the sampling is nonuniform, unlike in the classical periodogram, the window function $W(x)$ is no longer defined by a Dirac comb with regular intervals of $\Delta t$. It is, in turn, defined as:

$$W_{\{t_n\}}(t) = \sum_{n=1}^{N} \delta(t - t_n). \tag{B.8}$$

When applied to the original signal $g(t)$, the observed signal is given by:

$$g_{\text{obs}}(t_n) = g(t_n)\, \delta(t - t_n). \tag{B.9}$$

An uneven sampling can have problematic consequences for a periodogram based on Fourier transform. Recall that the classical periodogram is essentially the power spectrum from the true underlying function with an incomplete dataset. Even then, the underlying function, in this case $g(t)$, is sampled equally. This returns a $g_{\text{obs}}$ that properly retains the features of $g(t)$ and period retrieval is still possible, given a minimum $\delta t$.

What if the uneven sampling does not retain the features of $g(t)$? Or if it does, but during the observation the sampling rate is high at the beginning and slowly decreases near its end? When $g(t)$ is not appropriately sampled, the returned $f$ might not be $f_{\text{true}}$ at all. **This creates aliases or false frequencies that resemble the true frequency due to inadequate sampling.**

To address this, Scargle [Sca82] proposed a general from of the classical periodogram. From Equation B.7:

$$P_S(f) = \frac{1}{N}\left|\sum_{n=1}^{N} g_n\, e^{-2\pi i f t_n}\right|^2 \tag{B.10}$$

$$= \frac{1}{N}\left[\left(\sum_{n=1}^{N} g_n\, \cos(2\pi f t_n)\right)^2 + \left(\sum_{n=1}^{N} g_n\, \sin(2\pi f t_n)\right)^2\right] \tag{B.11}$$

the generalized periodogram can be written as:

$$P_{LS}(f) = \frac{A^2}{2}\left(\sum_{n=1}^{N} g_n\, \cos 2\pi f(t_n - \tau)\right)^2 + \frac{B^2}{2}\left(\sum_{n=1}^{N} g_n\, \sin 2\pi f(t_n - \tau)\right), \tag{B.12}$$

with $A$, $B$, and $\tau$ are arbitrary functions of the frequency $f$. These three values can be uniquely chosen in a way that the equation reduces to the classical periodogram when the dataset is sampled uniformly.

# C Appendix C: MCMC for $P_{rot}$

In Figure C.1 and C.2, I show the chains made by the walkers in the MCMC simulation for the period determination using the cosine function and the posterior PDF of the rest of the parameters. The MCMC run using the cosine function does not give a converging solution. In contrast, Figure C.3 and C.4 show the walkers converging.

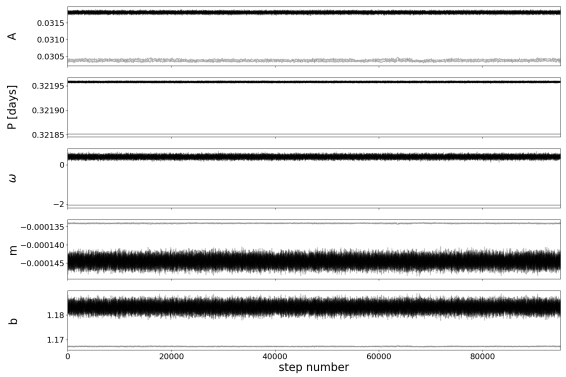


**Figure C.1:** The chains from the MCMC simulation using cosine function. The chains did not converge into one solution and it can be seen that there are around two-three chains that diverged from the main chain cluster.

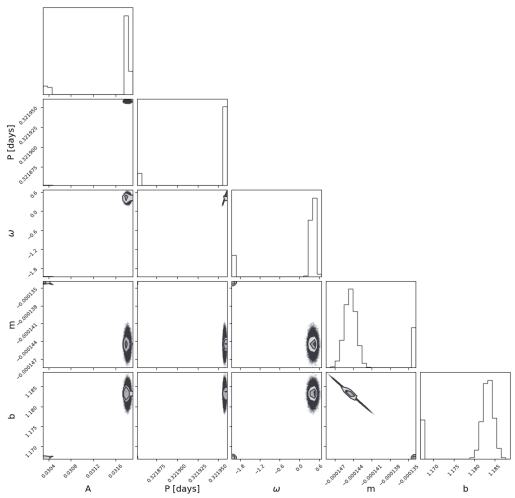


**Figure C.2:** Corner plot for the MCMC simulation using cosine function. The diverging chains prevented a proper corner plot to be produced, showing that the cosine function does not return a converged solution.

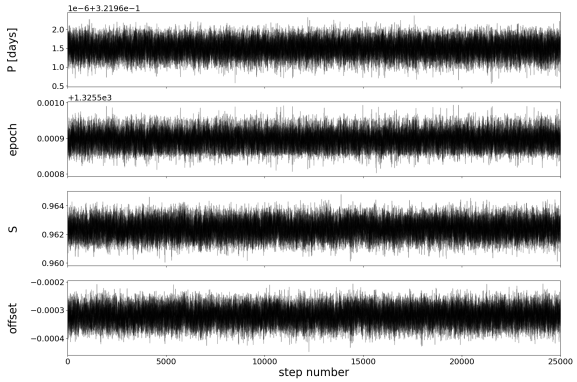


**Figure C.3:** The chains from the MCMC simulation using the modulation template. In contrast to Figure C.2, it shows the chains converging.

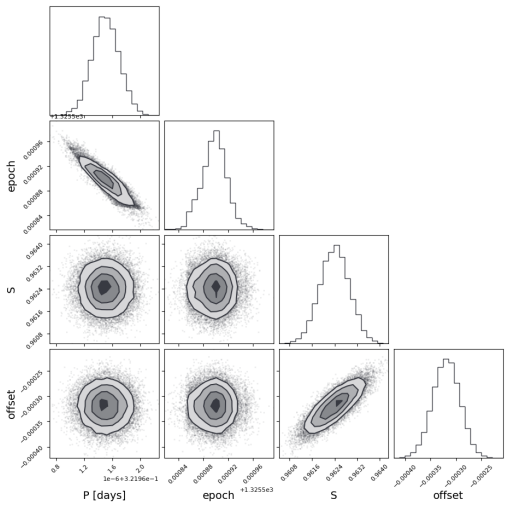


**Figure C.4:** Corner plot for the MCMC simulations using the modulation template.

# D Appendix D: CCFs $v \sin i_*$

In Figure D.1 to D.2, I show the CCFs of from two different datasets that were used to calibrate the $v \sin i_*$ in Section 4.5.1.

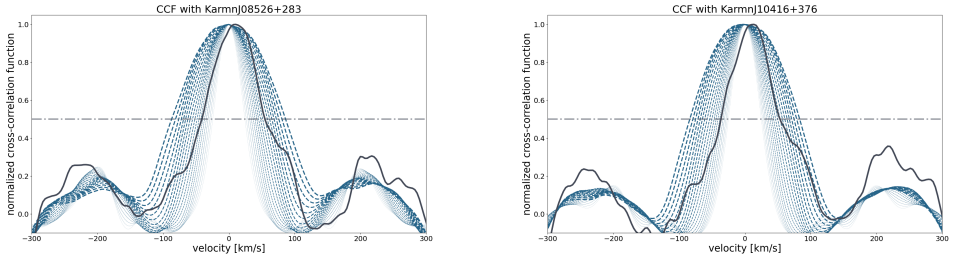


(a)




(b)

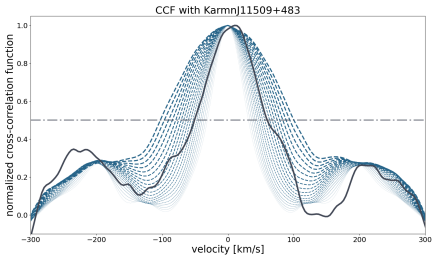


(c)

**Figure D.1:** CCF results (black line) of TIC 206544316 with KarmnJ08526+283 (a), KarmnJ10416+376 (b), and KarmnJ11509+483 (c) from Gaia RVS dataset. The CCF of the reference spectra with its artificially broadened counterparts are noted by blue lines. Note the shift in the CCF peak at the black line. Despite this shift, the FWHM of the CCF can still be reliably measured, and $v \sin i_*$ can still be calibrated, proving the robustness of the cross-correlation method against mismatch with individual lines.

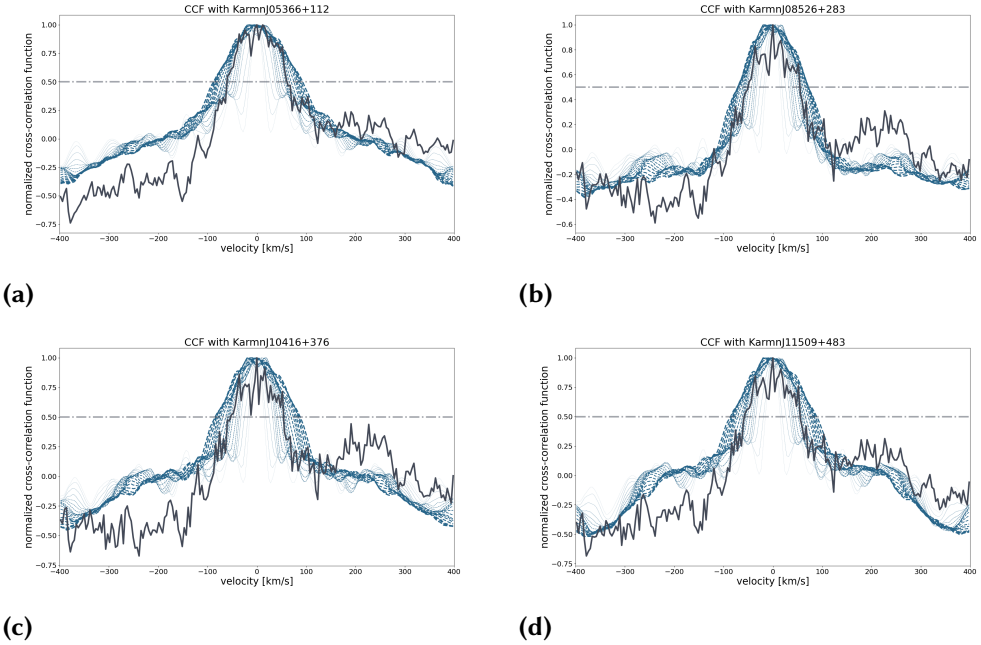


**Figure D.2:** CCF results (black line) of TIC 206544316 with KarmnJ05366+112 (a), KarmnJ08526+283 (b), KarmnJ10416+376 (c), and KarmnJ11509+483 (d) from MIKE-CARMENES dataset. The CCF of the reference spectra with its artificially broadened counterparts are noted by blue lines. Note highly irregular CCF shape due to the additional uncertainty and mismatch from cross-correlating with different instruments and improperly normalized spectrum. Regardless, the FWHM of the CCF can still be measured and $v \sin i_*$ can still be calibrated.

# E Appendix E: Isotropic inclination angles

Another important point of Bayesian framework of Masuda and Winn [MW20] is that its end goal is to compute the posterior PDF of $\cos i_*$, rather than $i_*$ directly. This is because the PDF for $\cos i_*$ becomes a constant:

$$P_{\cos i_*}(\cos i_*) = 1 \tag{E.1}$$

under the assumption of randomly oriented stellar rotation axes. This uniformity comes from the fact that stellar orientations are assumed to be isotropic, meaning all directions in three-dimensional space are equally likely.

However, note that what is measured is the stellar inclination angle $i_*$, the projection of the stellar rotation axes onto the observer's line of sight. Because of this projection, the PDF of $i_*$ is not uniform, even though, physically, stellar orientation follows an isotropic PDF. It, instead, follows a sine distribution $f(i_*) \propto \sin i_*$ (see Figure E.1). Thus, using $\cos i_*$ captures the underlying isotropy of stellar orientations and offers a more efficient sampling in MCMC simulations.

To understand why this works, consider an isotropic PDF of the stellar orientation. Since all orientations are likely, the distribution can be approximated as a sphere. The probability that a stellar rotational axis falls within a specific inclination range $di_*$ to the observer depends on the surface area subtended by that range (see Figure E.2). It is helpful to remember that observers can only see the projection of the celestial sphere and all parts of the sphere has equal probability to be observed. Because of that, the probability of a phenomenon is observed depends only on how much of it could "occupy" the celestial sphere. Therefore, the uniform distribution of the celestial sphere translates into a non-uniform observed stellar inclination $i_*$ in the case that all orientation is possible.

The surface element of a sphere is given as:

$$dA = \sin i_* \, di \, d\phi, \tag{E.2}$$

and integrating over the longitude gives the surface area subtended by the solid angle $di$:

$$dA = 2\pi \sin i_*. \tag{E.3}$$

Therefore, the PDF of the stellar inclination $i_*$, assuming an isotropic orientation, is proportional to $\sin i_*$:

$$P_i(i) \approx \sin i_*, \tag{E.4}$$

which implies that it is more likely for high inclination systems to be observed

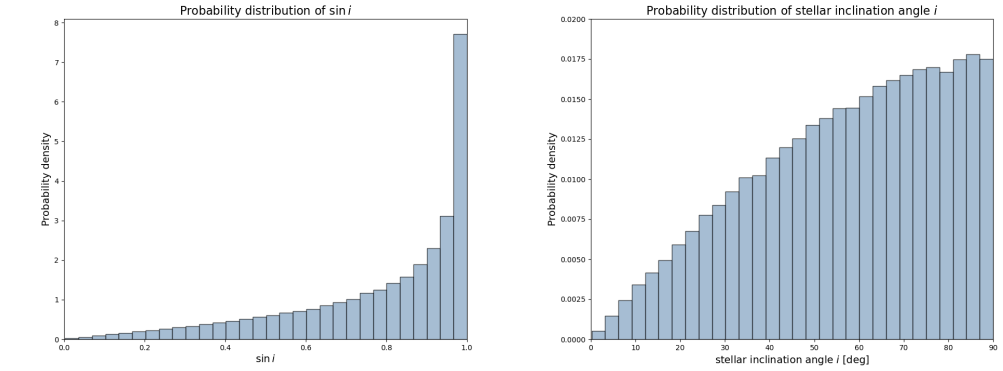


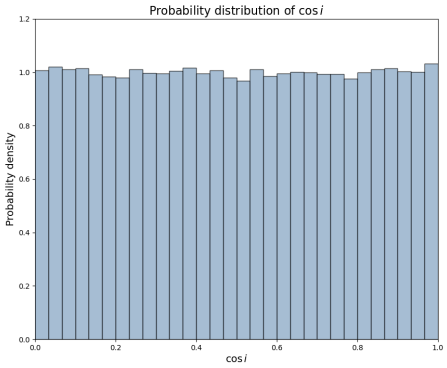


**Figure E.1:** PDF of $i_*$ assuming all orientations are equally likely. This corresponds to an isotropic distribution, which translates to $f(i_*) \propto \sin i_*$. Panel (a): PDF of $\sin i_*$; (b): $i_*$; (c): $\cos{}_*$. It can be seen that, although they represent the same physical quantity, $\cos i_*$ has a uniform distribution and can thus be used as an efficient sampling variable for MCMC simulations.

than those with pole-on orientations.

However, this PDF is inefficient to sample from, especially when MCMC is used. Section 4.3 describes the method of accepting (and rejecting) proposed values for sampling the stationary or targeted distribution of the Markov Chain. It should be noted that the acceptance of a proposed value depends solely on its probability within the distribution. A sine distribution means that randomly generating $i_*$ from 0 to 90° results in values being rejected proportionally to $1 - \sin i_*$. In other words, computation time is wasted at computing their probabilities without contributing meaningfully to the sampling.

To illustrate, consider Figure E.1. In Figure E.1 (b), I randomly generated inclination angles $i_*$ that follow a sine distribution (Figure E.1 (a)). If the probability of a distribution $P(\theta)$ considering a set of parameters $\theta$ is defined as:

$$P(\theta) \propto P_i(i), \tag{E.5}$$

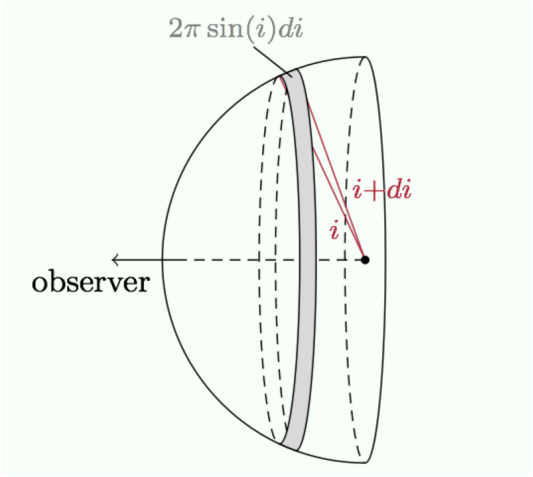


**Figure E.2:** Illustration of a stellar hemisphere facing the observer. A star's rotational axis is assumed to be randomly oriented relative to the observer, i.e., it has an isotropic probability distribution. This means that, physically, all orientations are equally likely. However, what the observer measures, $i_*$, is the projection of that orientation onto the plane of the sky. From the observer's perspective, the likelihood that $i_*$ falls within an interval $di_*$ is proportional to the area on the sphere subtended by that angle. This implies that higher inclinations (edge-on) are more likely to be observed than lower inclinations (face-on). From https://keatonb.github.io/archivers/uniforminclination.

which indeed is the case for Section 4.5.2, the low inclination values return such low probabilities that the proposed values are more likely to be rejected, leading to inefficient computation. The ideal approach is to use a flat distribution where the entire range of the parameter space can be efficiently utilized.

Fortunately, taking the cosine of inclination angles $i_*$ from Figure E.1 (b) returns a flat distribution from 0 to 1, as seen in Figure E.1 (c)[5]. Therefore, $\cos i_*$ can be used to represent the inclination angle while still preserving the geometric information of the isotropic orientation and observable bias toward highly inclined systems.

5 The mathematical reasoning behind why $\cos i_*$ yields a flat probability is explained in a way that is easy to understand in this blog: https://keatonb.github.io/archivers/uniforminclination accessed in August 2024. It involves mathematically finding a function of $\sin i_*$, or $f(\sin i_*)$, that returns flat for the relevant range. Transforming $\sin i_*$ to $\cos i_*$ satisfies that requirement.

# F Appendix F: MCMC results for $\cos i_*$ benchmarking

In Figure F.1, I show the rest of the marginal posterior PDF of $\cos i_*$ from my benchmarking.

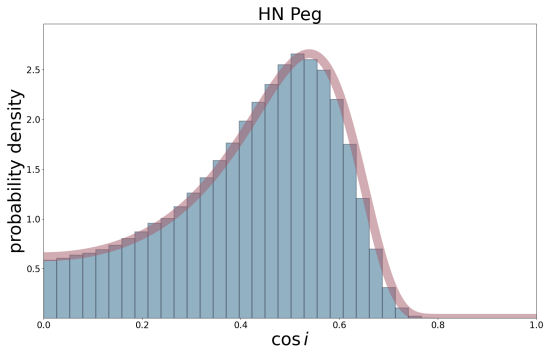


**(a)**

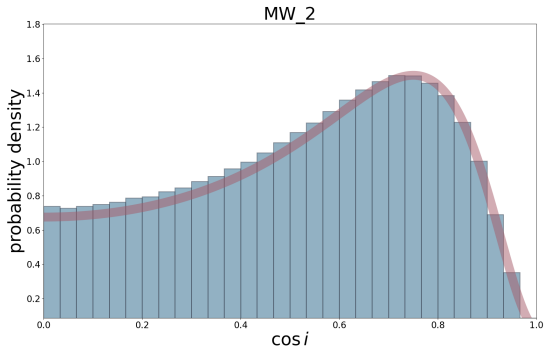


**(b)**

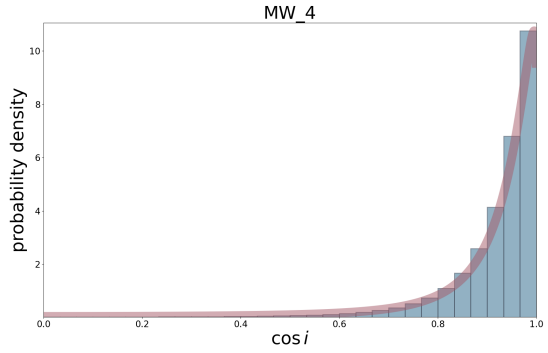


**(c)**

**Figure F.1:** Continuation benchmark cases from Figure 4.9. Panel (a): HN Peg; (b)-(c): the second and foruth illustrative case in Masuda and Winn [MW20]. Blue bars represent the marginal posterior PDF of $\cos i_*$ from MCMC and the pink line is the analytical solution from Equation 4.38.

# G Appendix G: Parameters of low-latitude spots

Supplementary table for Section 6.1 that shows the detailed parameters of low-latitude spots from spot transits found in literature.

| Star | Kepler-63 | CoRoT-2 |
|---|---|---|
| SpT | G5V | G7V |
| $P_{\mathrm{rot}}$ (days) | 5.40 | 4.54 |
| $\theta_{\mathrm{trans}}$ (deg) | $4-34$ | $-14.6$ |
| Average $R_{\mathrm{spot}}$ (Mm) | 32 | 50 |
| Minimum $R_{\mathrm{spot}}$ (Mm) | 14 | 20 |
| Maximum $R_{\mathrm{spot}}$ (Mm) | 40 | 75 |
| Reference | Netto and Valio [NV20] | Silva-Valio et al. [Sil+10] |

**Table G.1:** Parameter of spots on two Kepler-63 and CoRoT-2. The spot parameters are derived from the spot transit method that takes advantage an orbiting exoplanet transiting over a spot [Sil03]. The spot parameters for Kepler-63 are only listed for their low-latitude spots.

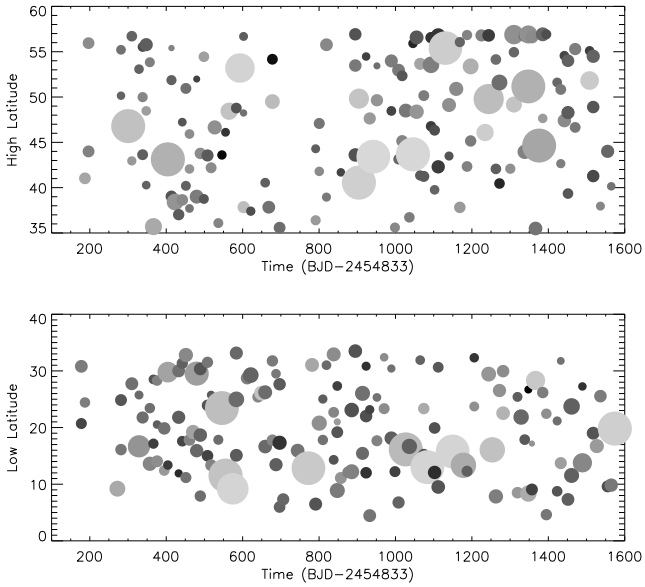


**Figure G.1:** Butterfly diagram of Kepler-63: temporal evolution of the spot latitude during the four years of observation of the Kepler on low- (bottom) and high-latitude (top) regions. The size of the discs is proportional to the spot radius. Low-latitude ranges from $4-34°$ while high-latitude ranges from $34-60°$. There is no strong difference in the distribution of spot radii in both regions. From Netto and Valio [NV20].

# Declaration of Authorship

I hereby declare that this thesis is my own unaided work. All direct or indirect sources used are acknowledged as references.

Potsdam, April 28, 2025


Cinta Vidante